9-20-2018

A SELF-ADAPTIVE ENERGY DISSIPATION STRUCTURE FOR LOW SPEED IMPACT AND PEDESTRIAN PROTECTION

James Wu
University of Windsor

A SELF-ADAPTIVE ENERGY DISSIPATION STRUCTURE FOR LOW SPEED IMPACT AND PEDESTRIAN PROTECTION

By

James Wu

A Thesis
Submitted to the Faculty of Graduate Studies
through the Department of Mechanical, Automotive and Materials Engineering
in Partial Fulfillment of the Requirements for
the Degree of Master of Applied Science
at the University of Windsor

Windsor, Ontario, Canada

2018

A Self-Adaptive Energy Dissipation Structure for Low Speed Impact and Pedestrian Protection

by

James Wu

APPROVED BY:

D.E. Green
Department of Mechanical, Automotive and Material Engineering

N.G. Zamani
Department of Mechanical, Automotive and Material Engineering

W. Altenhof, Advisor
Department of Mechanical, Automotive and Material Engineering

September 7, 2018

DECLARATION OF CO-AUTHORSHIP / REVIOUS PUBLICATION

I. Co-Authorship

I hereby declare that this thesis incorporates material that is result of joint research, as follows: The thesis was developed by the author under the supervision of professor Dr. Altenhof, from university of Windsor, with input from Dr. Bhattacharjee and Dr. Sundararajan, from Ford Motor Company. In all cases, the key ideas, primary contributions, experimental designs, data analysis, interpretation, and writing were performed by the author. The contribution of Dr. Altenhof was primarily through the provision of supervision, and the knowledge of crashworthiness and finite element analysis. The contribution of Dr. Bhattacharjee and Dr. Sundararajan was primarily through the provision of information and suggestions regarding industrial standard and manufacturability. Mr. John Magliaro contributed to the editing of the manuscript.

I am aware of the University of Windsor Senate Policy on Authorship and I certify that I have properly acknowledged the contribution of other researchers to my thesis, and have obtained written permission from each of the co-author(s) to include the above material(s) in my thesis.

I certify that, with the above qualification, this thesis, and the research to which it refers, is the product of my own work.

II. Previous Publication

This thesis contains 1 paper that have been previously published or submitted for publication within peer reviewed journals as follows.

Thesis Chapter	Publication title/full citation	Publication status
5-9	Wu J, Altenhof W, Bhattacharjee S, Sundararajan S and Magliaro J. A self-adaptive energy absorber for improved pedestrian safety and low speed damage requirements. International Journal of Crashworthiness. Accepted on September 7, 2018. This is an Accepted Manuscript of an article will be published by Taylor & Francis in Journal of International Journal of Crashworthiness, available online: https://doi.org/10.1080/13588265.2018.1524546	Accepted

I certify that I have obtained a written permission from the copyright owner(s) to include the above published material(s) in my thesis. I certify that the above material describes work completed during my registration as graduate student at the University of Windsor.

III. General

I declare that, to the best of my knowledge, my thesis does not infringe upon anyone's copyright nor violate any proprietary rights and that any ideas, techniques, quotations, or any other material from the work of other people included in my thesis, published or otherwise, are fully acknowledged in accordance with the standard referencing practices. Furthermore, to the extent that I have included copyrighted material that surpasses the bounds of fair dealing within the meaning of the Canada Copyright Act, I certify that I have obtained a written permission from the copyright owner(s) to include such material(s) in my thesis and have included copies of such copyright clearance to my appendix.

I declare that this is a true copy of my thesis, including any final revisions, as approved by my thesis committee and the Graduate Studies office, and that this thesis has not been submitted for a higher degree to any other University or Institution.

ABSTRACT

Bumper design regulations for low-speed vehicular impacts (Part 581, Bumper Standard, formerly FMVSS 215) and high-speed pedestrian impacts (ECE 127/GTR 9) possess a contradictory set of requirements. Essentially, an ideal bumper structure should be stiff under low-velocity vehicular impacts while exhibiting a softer response when impacting pedestrians at elevated velocities to satisfy both regulations. A series of energy absorbing structures capable of passively adapting their mechanical responses based on the loading conditions were investigated using finite element modelling tools which were validated to a series of experimental testing observations. The preferred structure consisted of a rectangular array of trapezoidal cells which buckle under single-cell impacts while resisting lateral deformation and artificially increasing the overall stiffness under large-area impacts. A geometric study of this dissipater demonstrated the potential to increase total energy absorption by 37.3% by adding thin-walled crossbars at the bases of adjacent cells. Additionally, a parametric study identified a combination between upper cell angle and the ratio between the wall thicknesses as the most critical parameter to consider when tailoring the overall mechanical response.

ACKNOWLEDGEMENTS

I would first like to thank my wife, Yutong Lu, and my parents, Weixing Wu and Yaohong Zhang, for their love and support through the period of my study.

I would like to express my deep gratitude and sincere thankfulness to Dr. William Altenhof, my academic advisor, for his support, encouragement and guidance with his vast of knowledge and experience in crashworthiness and finite element modeling. I would also like to thank my committee members, Dr. Green and Dr. Zamani, and industrial expert from Ford Motor Company, Dr. Bhattacharjee and Dr. Sundararajan, for their help and support. I am indebted to Mr. Kevin Harkai and Mr. Matt St. Louis for their technical assistance. I am also grateful to Matthew Bondy, Yang Song and John Magliaro for their help and friendship.

Last but not least, the financial support from Ford Motor Company and the Natural Sciences and Engineering Research Council of Canada (NSERC) are gratefully acknowledged.

TABLE OF CONTENTS

LIST OF TABLES

LIST OF FIGURES

LIST OF ABBREVIATIONS

ASTM	American Society for Testing and Materials
CAE	Computer aid engineering
ECE	Economic Commission for Europe
EDM	Electric Discharge Machine
FE	Finite Element
FEA	Finite Element Analysis
FEM	Finite Element Model
FMVSS	Federal Motor Vehicle Safety Standard
GTR	Global Technical Regulation
NHTSA	National Highway Traffic Safety Administration
PP	Polypropylene
SEA	Specific Energy Absorption

NOMENCLATURE

E	Young's modulus
L	Total number of discrete data
P	Load
P_m	Average load
S	Displacement
V	Validation metric
b_{eing}	Engineering stress
σ_{True}	True stress
ε_{Eng}	Engineering strain
ε_{True}	True strain
$\varepsilon_{Effective\ Plastic}$	Effective plastic strain

1. INTRODUCTION

Safety is a major concern for engineers when designing vehicles. Significant research efforts within the field of crashworthiness have historically been allocated towards studies involving occupant safety. However, in recent years, more attention has been raised in the protection of pedestrians, who could be more vulnerable in road accidents. Based on a report from NHTSA, over 5000 pedestrians were killed and over 70,000 pedestrians reported injuries in road accidents in the USA during the year of 2015 [1]. Among these cases, 85% were frontal impacts where the front bumper was the first entity to contact the pedestrian. Vehicular accidents are also the leading cause of death worldwide for ages 15 to 29 based on latest data from the World Health Organization [2].

In general, bumper design involves two sets of regulations: a pedestrian safety driven standard and vehicle protection driven standard. Pedestrian protection is tested by the requirements defined in UN regulation ECE 127/GTR 9 [3]. This regulation emphasizes a limit on the impact force and effect of impact location when the bumper collides with a legform impactor. In the Part 581 Bumper Standard, which was formally referred to as FMVSS 215 [4], the bumper is required to maintain a high stiffness when struck by an impacting pendulum at low velocities (~4 km/h). The engineering challenge proposed in this study is to design a bumper which can adjust and quasi-optimize its mechanical response over a broad range of loading conditions based upon the above described criteria.

In the ECE 127/GTR 9 testing requirement, two tests related to front bumper and front hood impacts have been developed. This study considered the front bumper tests since the bumper was the targeted apparatus; however, the final product of this study was an

energy absorber that can easily be adapted for multiple applications. Bumper testing for this standard involves an impact between a bumper and legform impactor. The standard requires the legform to impact the front bumper at a velocity of 40 km/h. The results of each test are evaluated depending upon the bumper height of the tested vehicle. When the lower bumper height is above 500 mm where the upper legform impactor was used, the maximum impact force must be limited to 7.5 kN and the maximum bending moment cannot exceed 510 N·m throughout the impact duration. When the lower bumper height is below 425 mm and a flexible lower legform impactor is utilized, injury is evaluated both for the knee and tibia sections. The knee injury is evaluated with the elongation of three specific dimensions in the knee joint center which represents the medial collateral ligament (MCL), anterior cruciate ligament (ACL) and posterior cruciate ligament (PCL). The tibia injury is evaluated based on the maximum bending moment within the tibia section of the impactor. The maximum dynamic elongation of the represented dimensions of the MCL, ACL and PCL are limited to 22 mm, 13 mm and 13 mm, respectively. The maximum tibia bending moment is set to 340 N·m. In this legform impact scenario, a deformable bumper structure is desired to minimize the impact force.

In the Part 581 Bumper Standard [4], the test apparatus is composed of a front and rear bumper impacted by a pendulum. The impacting mass, calculated by adding the mass of the pendulum block and 1/3 of the mass of the supporting arm, is assumed as equivalent to the vehicle tested. The impact velocity is prescribed as 3.7 km/h (equivalent to 2.3 mph) for longitudinal impacts and 2.1 km/h (equivalent to 1.3 mph) for corner impacts as per US standards. In the European and Canadian standard, the requirement is similar with an impacting speed of 4 km/h. In this scenario a bumper with a stiff structure and high energy

dissipation potential is ideal. The post-test examination of the vehicle includes the alignment of the lights, the suspension, the functionality of the door, hood, cooling system and other critical components. In the low speed pendulum test, the bumper is required to be stiff and absorb large quantities of energy to prevent severe damage of other, more expensive and vital components.

This study was driven by the increased attention directed towards pedestrian protection in road accidents. The interest of the author is to develop a structure for the vehicular bumper that could reduce damage to the pedestrian while still being able to provide the required protection to the vehicle.

2. LITERATURE REVIEW

A bumper protects other components of the vehicle including the engine and passengers by dissipating kinetic energy. When excessively high impact energy must be absorbed, most of the energy will be absorbed through permanent deformation of the dissipating structure. Considerable research has been conducted on energy absorption to study the deformation behavior of various structures under load with the intent to maximize spatial energy absorption and achieving a controllable load/displacement response.

Considering the objectives of this study, a literature review was conducted on various energy absorbing structures. The primary interests of previous studies were the deformation behavior of structures and their corresponding energy absorbing behavior. The geometries studied were mostly thin-walled structures with large design volumes for maximum deformation and energy dissipation. Energy absorbing structures are usually evaluated with the consistency of the load/displacement response and energy absorption.

2.1. Axial loading of thin walled structure

Plastic deformation by loading thin-walled tubular structures in the axial direction usually involves changes in shape or size of the cross-sectional area of the tube which repeats in the axial direction of the tube throughout the collapsing process, as in progressive folding, tube inversion, tube splitting, or axial cutting. Progressive folding has been studied extensively by many researchers as in Yuen and Nurick's overview [5]. Under progressive folding, a small section of a given thin-walled extrusion folds as the structure is loaded and tube length decreases. While a load is continuously applied, an additional section will fold as the previous folding completes, forming a progressively repeating pattern. The expected load/displacement response for progressive folding will fluctuate with local maximum and

minimum that coincide with the folding process. The deformation was controlled by adjusting the geometry of the tube. Guillow studied axial loading of circular 6060 T5 aluminum tubes and summarized the observed deformation modes occurring from different tube dimensions [6]. Guillow tested 70 tubes with various dimensions and classified the deformation into axisymmetric collapse (Figure 1a), non-symmetric collapse (Figure 1b), mixed mode (Figure 1c) and Euler's buckling mode. The occurrence of these deformation modes was mapped with factors of diameter to thickness ratio and diameter to length ratio. Euler's buckling can also be predicted by factoring in consideration for Euler's critical buckling load. The maximum load required to initiate progressive folding should never exceed Euler's critical load.

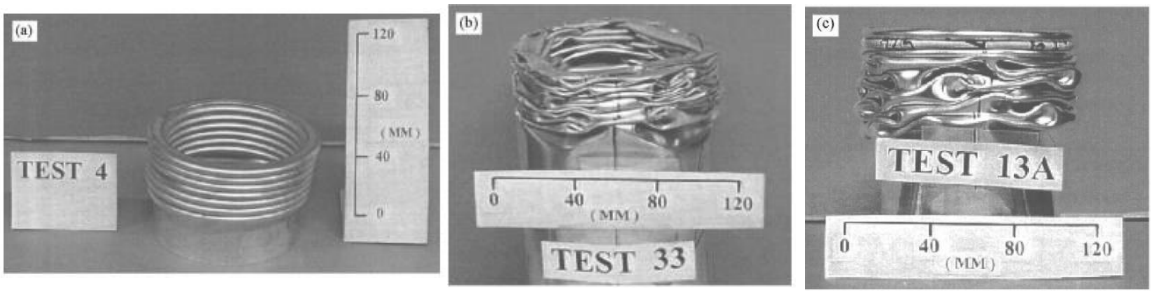

Figure 1. (a) Axisymmetric collapse, (b) non-symmetric collapse, and (c) mixed mode. [6]

Furthermore, the frequency and amplitude of the load/displacement response can be controlled by altering the cross-sectional geometry of the tube. Tang [7] studied multi-cell columns under axial loading, where the cross section of the column was divided into cells as shown in Figure 2. Throughout this study, it was determined that increasing the number of layers inside the column increased the specific energy absorption, or energy absorption per unit mass. Furthermore, cylindrical, multi-cellular columns displayed a consistent loading response compared to square columns.

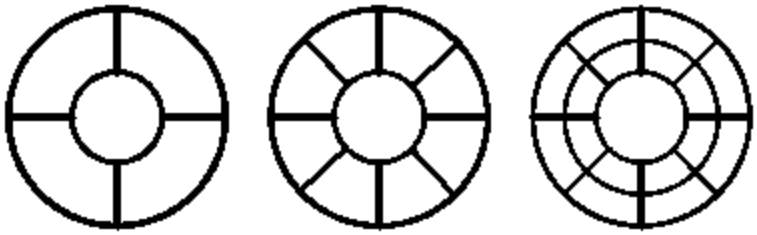

Figure 2. Cross section of multi-cell columns with different layers. [7]

When axial loading thin walled tubes, machining pre-designed stress concentrators into the structure such as grooves, notches or a drilled hole are commonly used to control the deformation during the collapsing process. As in Hosseinipour‘s research [8], grooves were pre-cut on the circumference of the cylindrical tube. During the collapsing process, the grooved location transitioned into the plastic folding hinge and influenced the frequency of the load/displacement response.

Tube inversion is another deformation mode which allows for energy absorption under axially compressive loading. This deformation mode primarily absorbs energy by altering the radius of the cylindrical tube. Since the deformation process is continuous, it displays a consistent load/displacement response. There are generally three variations of tube inversion as shown in Figure 3. Type A and B in Figure 3 displays the first design of tube inversion, in which one end of the extrusion must be manufactured with a different diameter compared to the majority of the tube. The smaller/larger end will be fixed during the deformation and the inverting process will be initiated at the fixed end. The second type is shown as type C in Figure 3, where the tube possesses two sections with different diameters connected with a transition section. When the tube is under axial loading, inversion will initiate at the transition section. The third design, shown as Type D and E in

Figure 3, is the design with the lowest manufacturing cost and easiest to use. The tubes used in this scenario are straight tubes without special features.

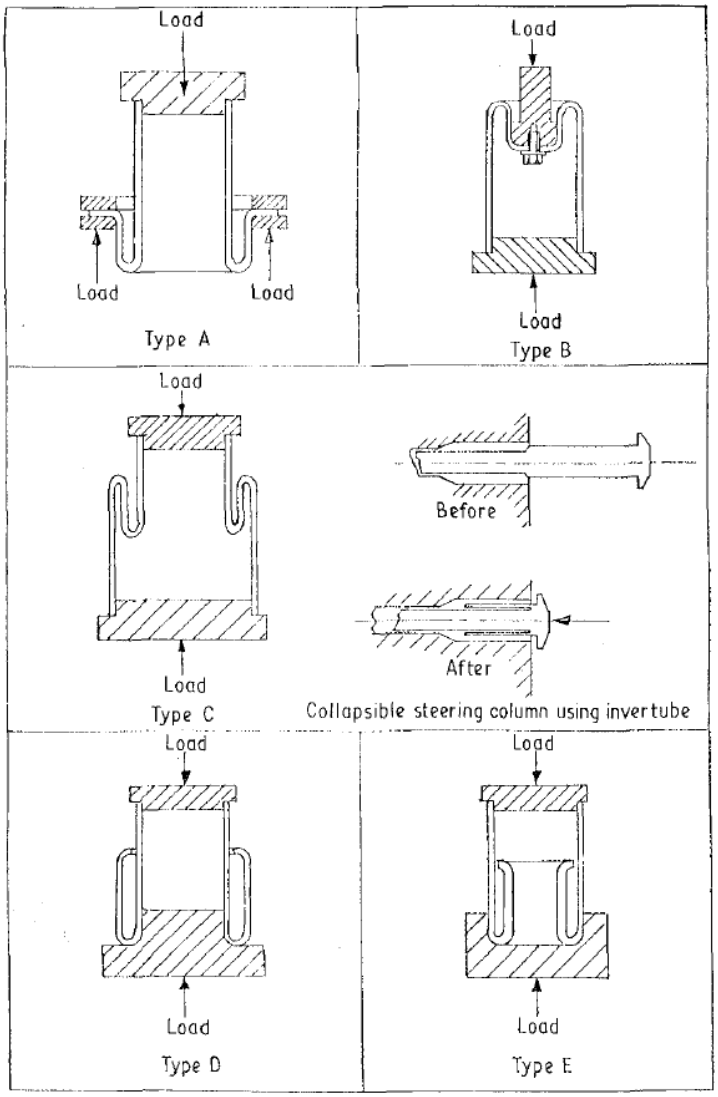

Figure 3. Types of tube inversion. [9]

An inverting die, or deflector, with suitable radius will cause the tube to increase or decrease in diameter and initiate the inversion process. The first and second design of tube inversion are commonly called free inversion of tubes; load characteristics of the compression process mostly depend upon the tube geometry and material property. In the third design, where a deflector is involved, the additional factors of the deflector geometry

and the contact condition are also important to the energy dissipation behavior. Al-Hassani has conducted research on tube inversion with the use of a deflector [9]. In this study, the author has performed experiments on tubes composed of several materials while also utilizing deflectors with various dimensions. Comparing tubes with various materials revealed that for extrusions which possessed a high stiffness, asymmetric buckling could form during the inversion process. The author has also found the optimal deflector angle and radius that could maximize the energy absorption of the deformation process. When the deflector was designed with a large radius or a tapered surface, the extrusion material under axial loading would reach the strain limit and the wall will split into evenly spaced circumferential strips and transition the deformation mode into tube splitting. In Huang's study [10] of tube splitting, the energy has been found to be dissipated by splitting the tube, curling the strips, and the friction between the tube and deflector. The energy dissipation of axial splitting could be further increased by adding a plate to the system to prevent excessive curling.

Axial tube cutting, studied by Jin [11], considered energy dissipation by cutting the sacrificial tube with blades along the axial direction. A highly repeatable and consistent load/displacement response was achieved in the author's research. The load/displacement response of the cutting process is strongly correlated to the extrusion dimensions and the number of cutting blades. The load/displacement response of axial tube cutting could intentionally be varied throughout the cutting process by machining the tube to have different thicknesses along the axial direction; this technique cannot be implemented for other axial loading deformation modes. A deflector could be installed to deflect the petalled sidewalls and increase the space efficiency of the cutting system.

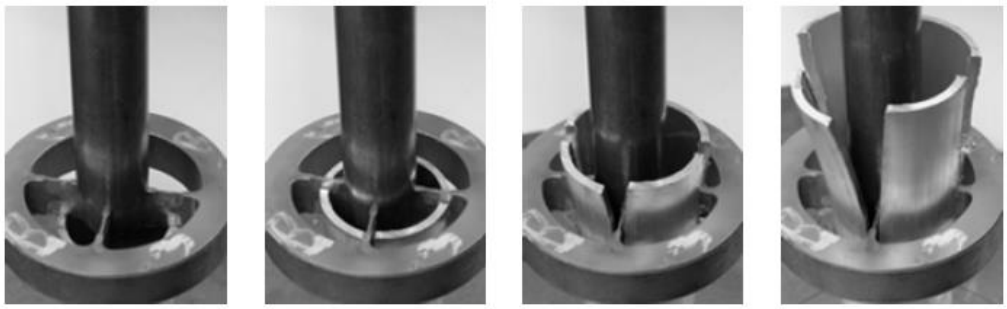

Figure 4. Typical tube cutting process without deflector. [11]

Unique cases of axial loading were studied by loading structures with circular cross-sections which varied in the loading direction such as the frustum investigated by Alghamdi [12, 13] or spherical shells studied by Gupta [14]. In the study of the frustum, the deformation of the structure experienced a combination of bending and change in surface area which promoted increased energy absorption. The load/displacement response was consistent before the displacement reached 50% of the height of the frustum. Further study also showed the specific energy absorption increased when the larger end of the frustum was constrained during the process. When the larger end of the frustum was constrained, more plastic hinges formed during the deformation (Figure 5b) which increased the total energy absorption; fluctuation in the load/displacement response was significant. In the study considering spherical shells, the load/displacement response presented a smoothly increasing load for shells with a constant wall thickness. With the proper design of variable shell thickness along the axial direction, a near-constant load/displacement response was achieved.

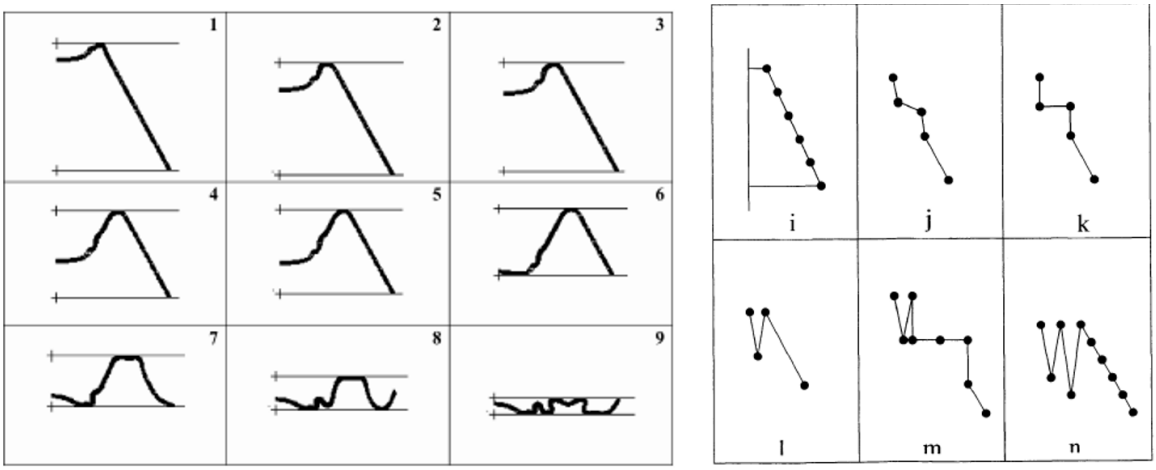

(a) (b)

Figure 5. Deformation mode of frustum: (a) with no constraint, (b) with the larger end constrained. [12,13]

2.2. Lateral loading of thin walled structure

The mechanical response of thin-walled structures loaded in the lateral direction has been studied extensively [15-20]. In this configuration, tubes with multiple cross-sectional geometries were tested, experiencing a load in the lateral direction and absorbing kinetic energy as the structure deformed. Studies for square or rectangular shaped tubes demonstrated excellent resistance to deformation during the initial contact, followed by a loss of rigidity as the structure experienced continued deformation. The load/displacement response in the process of deforming a square tube demonstrated a high peak load initially, followed by a rapid decrease and more consistent, lower load in the later stages of deformation. When a circular tube is crushed resulting in deformation in the lateral direction, the deformation of the structure is continuous during the process and the load/displacement response is more consistent. Since the deformation modes observed for tubes under lateral loading are relatively simple and displayed limited energy absorption capabilities, researchers such as Khanchehzar [21] and Niknejad [22] have conducted

studies on reinforced tubes with additional internal cross-sectional geometry or foams to increase the controllability and energy absorption capability. In Niknejad's study [22], modified circular tubes with grooves added along the axial direction were tested and compared with various internal reinforcement conditions. The reinforcement conditions included filling the internal volume with foam, inserting a smaller, empty cylindrical tube and inserting a smaller foam filled tube. It was found that the specific energy absorption of the tube with the first two reinforcements was decreased, while the last reinforcement condition increased the specific energy absorption. Constraining the space for deformation of circular tubes was also studied by Baroutaji [23] to observe the change in load/displacement response and energy absorption. The study demonstrated that when the deformation of the tube was constrained, the structure will deform in a more complex mode and increase the energy absorption. Lu [24] further elaborated on the behavor of tubes with external constraints loaded with various types of impactors.

To maximize the energy dissipation of tubes loaded laterally, Smith [25] developed and tested composite structures comprised of braided stainless-steel tubes and aluminum foam cores. The braided tubes subjected to transverse loads increased in length and simultaneously decreased in diameter; as the diameter of the tube decreased, the foam cores were progressively crushed, as shown in Figure 6. This deformation mode allowed for concentrated loads to be dissipated more effectively over the volume of the entire structure, thus increasing the total energy absorption.

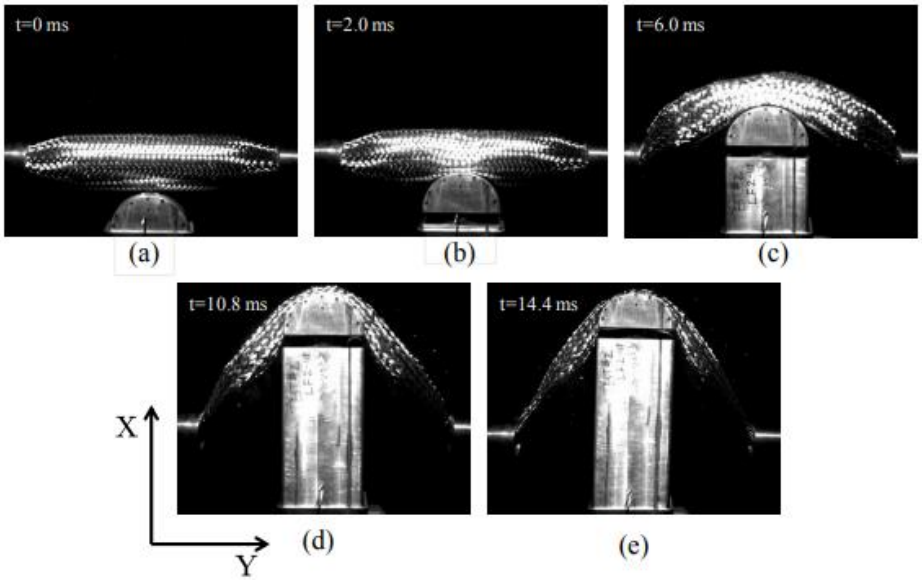

Figure 6. Braided tube with aluminum foam core under concentrated loading. [25]

2.3. Self-adaptive eggbox shape structure

Among the multitude of energy absorbing structures studied previously, the "eggbox" geometry researched by Deshpande [26], Zupan [27], Nowpada [28], Sashikumar [29] and Yoo [30] was relevant to this study and shared the common goal of passive self-adaptability. The structure was composed of a conical geometry formed with sheet metal above and below the median plane, alternatively, as in Figure 7. The deformation mode of the conical structure was similar to the frustum when loaded axially. However, the load/displacement response was more consistent compared to the loading of the frustum due to the rounded corners. When the structure was loaded, the response was relatively consistent up to 50% of the structural thickness; the amplitude of the force was strongly correlated to the loading area. As shown in the study of the "eggbox" structure [28], when a single frustum is loaded with constrained edges, the load/displacement response is nearly 1.8 times greater than the free-edge version. This

provides the opportunity for a passively adaptable load/displacement response by adjusting the loading area of the structure.

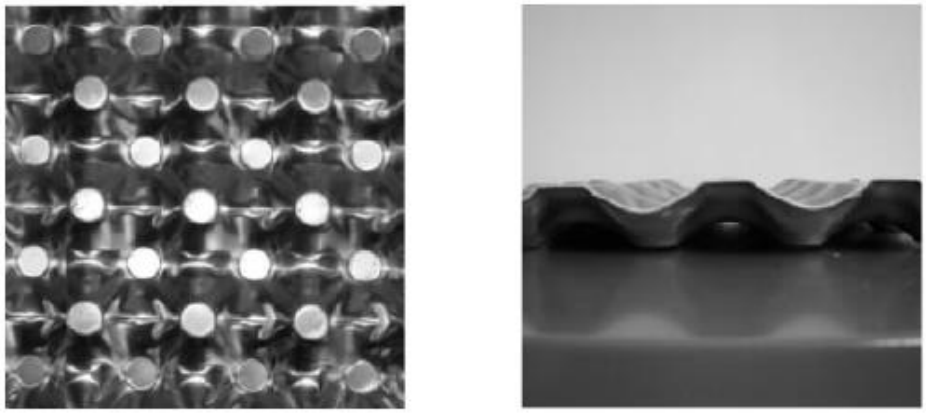

Figure 7. Plain and section view of eggbox structure.

2.4. Summary of literature review

Previous investigations of general energy absorbing structures have provided information regarding the relationship between deformation modes and the load/displacement responses. Under the axial loading of tubes, many different deformation modes were studied. The tube splitting mode had the highest specific energy absorption compared to other axially loaded dissipaters. Axial cutting yields the most consistent load/displacement response and has very good controllability. Tube inversion also exhibits a favorable load/displacement response but could only utilize a maximum of 50% of the total length for energy absorption. The various laterally loaded structures provided good energy absorption with minimal displacement. While the square tubes demonstrated excellent plastic deformation resistance, circular tubes benefit from a more consistent load/displacement response.

The studies of the eggbox structure, lateral loading of rings with various constraints and axial loading of frustums demonstrated the capabilities of passively adaptable energy absorbers. The corresponding deformation modes could be altered under different loading conditions or with modified boundary conditions.

3. RESEARCH OBJECTIVES

As stated in Section 1, two testing standards exist to provide a guideline for ideal bumper performance. However, the stipulations from each set of regulations posted by the ECE 127 and Part 581 of US standard are conflicting in terms of the desired structural properties. The purpose of this investigation is to develop a structure to passively adapt its mechanical response for high velocity pedestrian impacts and low velocity, large contact area impact scenarios. This allows for the achievement of performance requirements for different impact/crash conditions, thus quasi-optimizing the performance of the bumper for various potential loading conditions. In this study, numerical analyses will be performed to meet these goals. Finite element models will be constructed to represent the two distinct impact conditions posted in the testing standards. The simulated tests will consider quasi-static deformation of the designed structure, and the outcome will be discussed with emphasis on the aspects significant to the performance of the designed structure. The study will be conducted in 4 major sections as follows:

1. A pilot study will be conducted as the first step of the research. During the pilot study, brainstorming and testing of possible designs will be the primary focus. The knowledge obtained from the literature review will be utilized as the foundation of this study. A most preferred design will be determined to be used as the base structure for further study and referred to as the designed structure in this thesis.

2. Model verification and validation will be performed for the FEM of the designed structure that will be used in further investigations. A physical specimen, with similar geometry to the designed structure, will be manufactured and tested in a lab apparatus. The numerical model will be verified and validated with the physical

results. After the model is verified and validated as acceptable representation of the physical test, similar modeling technique will be used in further study.

3. A further parametric study will be performed with the designed structure to understand the significance of the critical dimensions and features. The designed structure will then be adjusted based upon the knowledge obtained.

4. The final section will be a geometric study utilizing the adjusted structure from parametric study. In this section, material will be added/removed from the structure at critical locations to reinforce the structure and/or to modify the deformation sequence within the system.

Throughout this study, CAE software will be utilized to construct the FEM and perform numerical analysis of the impacting event. Software and tools used for the validation of the models will be discussed in later sections.

4. PRESCRIBED DESIGN REQUIREMENTS

The research within this thesis was an industrial driven project, therefore, a set of requirements was prescribed at the initial stage of the research. In this study, the impact was simulated utilizing LS-DYNA. The designed structure was impacted under two distinct impact conditions, which will be referred to as the legform test and pendulum test in the latter sections. Since the FEM was a simplified representation of the testing standards, the requirements of the results were also narrowed to limit the load response for legform tests and the energy absorption for pendulum tests. Specific dimensions of the model and requirements of the test were as follows:

1. The prescribed design volume implemented in the analyses were 500 mm long, 100 mm wide at the impact surface and 80 mm deep in the loading direction. This geometry was considered to approximate a potential bumper-type energy dissipating structure and/or other geometries which would allow for the examination of structural performance under both localized and full area contact loading.

2. The impactor of the pendulum test was represented as a flat plate with dimensions of 600 mm long and 112 mm wide, which was large enough to fully contact the surface of the energy absorber. The impactor for the legform test was a solid cylinder with a radius of 125 mm and length of 112 mm.

3. The impacting direction for both tests was perpendicular to the 500 mm by 100 mm impact surface of the design volume, which is in the negative z-direction in Figure 8. For the pendulum test, the impactor makes full contact with the designed energy dissipater where the surface of the impactor remains perpendicular

to the impacting direction. In the legform test, the impactor will contact the center portion in the contact surface of the energy dissipater, the center axis of the impactor was positioned perpendicular to both the impacting direction and the longer side of the design volume. In Figure 8, the green, blue, and red parts represent the legform impact, pendulum impactor, and design volume respectively. Note that for each individual test, only one impactor will be present and impact with the dissipater.

4. The legform test represents the scenario where the pedestrian impacts with the bumper at high velocity. The prescribed motion throughout the test was 10 m/s. Since the goal was to minimize damage to the pedestrian, the maximum load during the deformation process was stipulated to not exceed 6 kN. The energy absorption was also a variable that was considered, but the primary focus was to reduce the load response. The pendulum test was modeled following the low speed test scenario, and the impactor was set to travel at 1 m/s. Since the results of the test could not be assessed with a similar approach to the Part 581 test requirement, energy absorption was used to evaluate the result. The basic requirement was to absorb 1 kJ of energy through the deformation process, which is equivalent to the kinetic energy of a small car traveling at 4 km/h. The travel distance of the impactors in both tests were 60 mm, which was 75% of the total depth within the design volume. No requirement was postulated for the mass of the system, however, since the specific energy absorption is an important aspect in evaluating energy absorber, it was considered as a minor aspect in the comparison of test results.

5. Although the estimated cost was not a part of the requirements for the project, the manufacturability was considered through the design process. The material was also not restricted; however, a polymeric material model was kindly provided by the industrial partner to be utilized in the study.

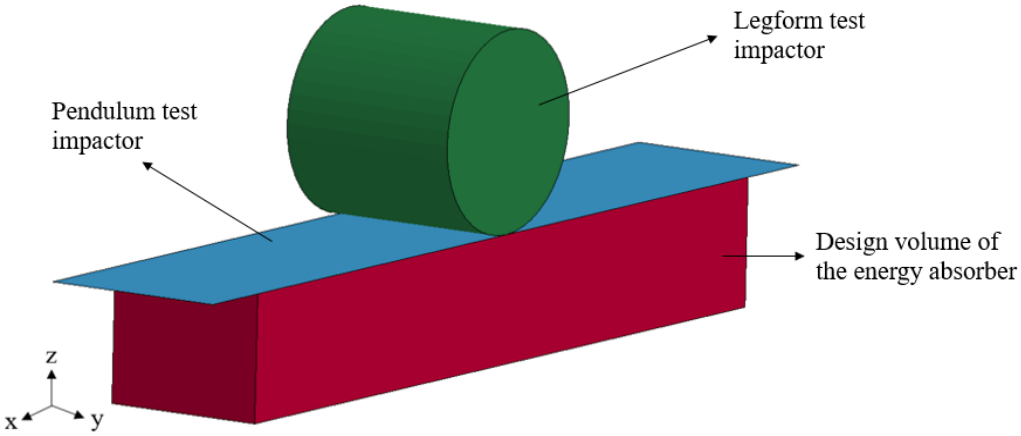

Figure 8. Demonstration of impactor and design volume.

5. PILOT STUDY

The objective was to design a self-adaptable system; therefore, it was important to decide what conditions the system must be adapted to. By comparing the difference between the impact scenarios, the major differences between these tests were the impact velocities and contact surface conditions. A structure capable of passively adapting to multiple impact velocities was anticipated to require complex working mechanisms, and such a system may not behave as intended under dynamic loading conditions. Therefore, the scope of this investigation was limited to the consideration of adjusting the deformation mode by controlling the contact area.

The authors wish to emphasize the adaptive characteristics of the system to the force/displacement behavior when the system is subjected to either (i) a local region of deformation or (ii) the condition of complete, full contact between the energy dissipation system and the impactor. In the case of a bumper system, the former could potentially represent a legform impact condition, while the latter could represent a full-frontal impact condition.

Many designs of the self-adaptive energy absorbing system were considered during the brainstorming stage. The designs consisted of two major categories. The first category was a two-stage system where the first stage acted as a mechanical switch and affects the deformation mode of the second stage. A simple illustration of such a system is shown in Figure 9. The gray blocks represent the switch element and the blue blocks represent the energy absorbing element, each switch element would control the deformation of a distant energy absorbing element, as demonstrated by blocks A and B in Figure 9. When a localized impact occurred near block A, the switch will trigger a mechanical link and

increase the stiffness of energy absorbing element B. However, since block B will not be in contact with the impactor, the impacting event will have a reduced load response. Under a large area impact event, all switch elements would be triggered, therefore the overall stiffness of the system would be increased. The second category of designs was characterized by no moving parts and has the structure divided in multiple repeated cells. The structure could be stiffened by having the deformation of two adjacent cells interacting with each other and forcing the deformation mode to change.

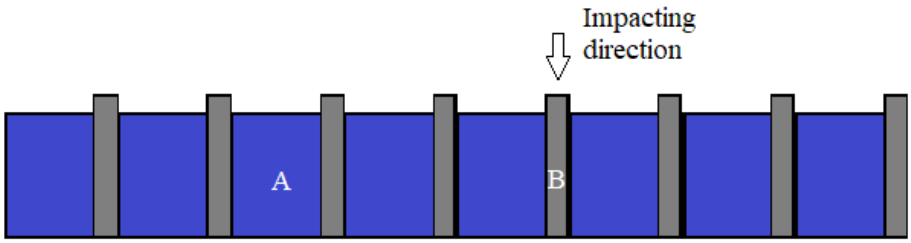

Figure 9. Demonstration of two-stage self-adaptable system.

The first category has the advantage of being able to modify the deformation mode on a large scale since moving parts are available. However, if multiple objects where impacted simultaneously, for example, two legs of a pedestrian, one object may trigger the switch and the other object could be impacted by the stiffened structure. Therefore, the designs of the first category were not ideal for complex scenarios although it may be acceptable in terms of satisfying the test requirement. Also, the space occupied by the switch element will have low contribution to the energy absorption, which my lower the overall energy absorption. Compared to the designs of the first category, designs within the second category could be more reliable since there is no reliance on moving parts. With simpler designs, the manufacturing costs would almost certainly also be reduced. Therefore, designs from the first category were withdrawn from further consideration.

A series of analyses were completed on proposed designs originating from established and previously discussed energy absorbing systems. These analyses emphasized the compressive loading characteristics of the energy dissipation system with the application of two loading conditions; a localized contact region and a full contact condition.

5.1. Finite element model of pilot study

The pilot study designs were developed with CATIA V5, discretized in a capitalized mesh with HyperMesh, then transferred to LS-PrePost to generate the keyword for simulation within LS-DYNA. Details of the finite element model which was used for the pilot study designs are listed below. Minor changes of modeling parameters throughout the research will be stated in later sections as necessary.

5.1.1. Element discretization

The pendulum impactor of the test was modeled as flat plates with shell elements, and the legform impactor was modeled with solid elements. Both impactors were modeled as rigid bodies since negligible deformation in these components was expected. The pendulum impactor utilized elements with an average size of 8mm by 8 mm. The legform impactor was modelled with 44 elements along the radius to form a relatively smooth outer surface. The energy absorbing structures were modeled with all hexahedron solid elements with 3 elements through the wall thickness; the elements had edge length between 0.5 mm to 2 mm. The largest element aspect ratio was 3 for the hemispherical design and 2 for the other designs. The minimum characteristic length of the elements within the dissipater was 0.4 mm. The constant stress element was selected for the pilot study simulations to obtain results with shorter simulation time. Hourglass control was implemented with

Belytschko-Bindeman hourglass viscosity and hourglass coefficient of 0.15 to reduce hourglassing.

5.1.2. Material properties

A piecewise linear isotropic plasticity material model based on von Mises yield criterion, MAT_024 in LS-DYNA [31], was used to model the elastoplastic behavior of the dissipater in the simulation. The material property used for the study was provided by the industrial partner, which was PP T20 polymer. The material had strain rate effects implemented in the plastic region. The density, elastic modulus, and Poisson's ratio were specified as 1040 kg/m^3, 1.1 GPa, and 0.3, respectively. The strain to failure was 0.8. The yield stress and the effective stress versus effective plastic strain relation were rate dependent and described with multiple stress versus strain curves over multiple strain rates. The yield stress and ultimate stress under a strain rate of 0.001 s^{-1} were 9.2 MPa and 25.2 MPa, respectively. The ordinate of the effective stress versus effective plastic strain relation increased by approximately 2 MPa whenever the strain rate increased by a factor of 10.

5.1.3. Contact algorithms

The contact algorithm defined between the impactors and the energy dissipater was a segment based, automatic surface-to-surface contact [31]. In this contact definition, the dissipater was the slave and impactors were the master since the dissipater possessed a more discrete mesh. The static and dynamic coefficient of friction was unknown since no physical material was available for testing. Nevertheless, the friction coefficient was estimated to be 0.4 for the static condition and 0.3 for the dynamic condition; these represented the median values from a multitude of values presented in various engineering

recommendations and supplier catalogs for steel to polymer contact. The exponential decay coefficient was set to 10^4 for all contact definitions which resulted in a rapid transition between the static and dynamic coefficients of friction. The optional card "SOFT" was activated with default parameters to invoke segment-based contact and reduce penetration. An automatic single-surface contact algorithm was also defined for the dissipater to account for self-contact during compression. The single surface contact included friction coefficients of 0.5 and 0.4 for static and dynamic conditions, respectively.

5.1.4. Boundary conditions and simulation environment

Several boundary conditions were applied to the impactors and the energy absorbing structures. The impactors were constrained to only allow for translation in the z-axis as shown in Figure 8. The boundary condition of pilot study designs was different due to the geometry of the structure, which will be discussed in a later section with the dimension of the designs. Impactor displacement was defined with a boundary prescribed motion with 10 m/s for the legform test and 1 m/s for the pendulum test as described in the prescribed requirements in Section 4. All models were simulated with explicit time integrals. No time scaling or mass scaling was used. The analysis was performed with LS-DYNA, shared memory processing (SMP), double precision solver R8.0.0. Data from the simulation results including energy terms and contact forces were output at 50 kHz for the legform. Since the pendulum tests were simulated with a test rate 10 times lower than the complementary legform tests, the data from the pendulum tests were collected at a proportionate rate of 5 kHz. By carefully observing and comparing the load/displacement responses, it was determined that the data collected provides a reasonably accurate representation of the expected test results.

5.1.5. Layer offset of energy absorber

For the designs with a continuous contact surface, the legform impact test result was not affected by the location where impact was initiated. However, for the design structure with a discontinuous initial contact surface, as shown in Figure 10, the load response will be affected. Figure 11 shows the comparison of the legform test results by having different initial impact locations for the structure in Figure 10. This effect will cause the results of legform test for the structure with a discontinuous contact surface to be unreliable. To reduce this inconsistency, the structure was divided into multiple layers in the y-direction and offset in the x-direction. The number of layers was decided based upon the size of discontinued space, larger space required more offset layers. Each layer was offset in the x-direction with distance calculated by the dividing the x-dimension of the cell with number of layers. Preliminary design 2 and 3 in the following section were divided into several layers, as needed.

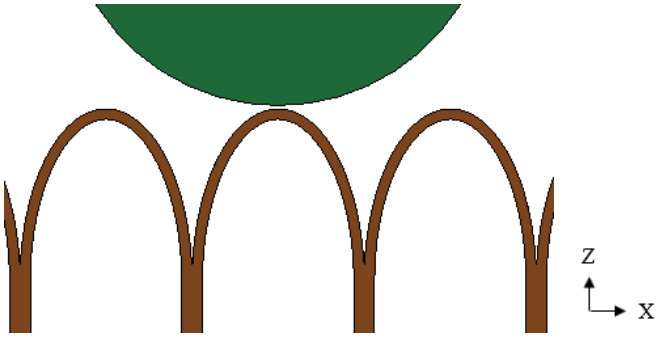

Figure 10. Legform test of structure with discontinuous contact surface.

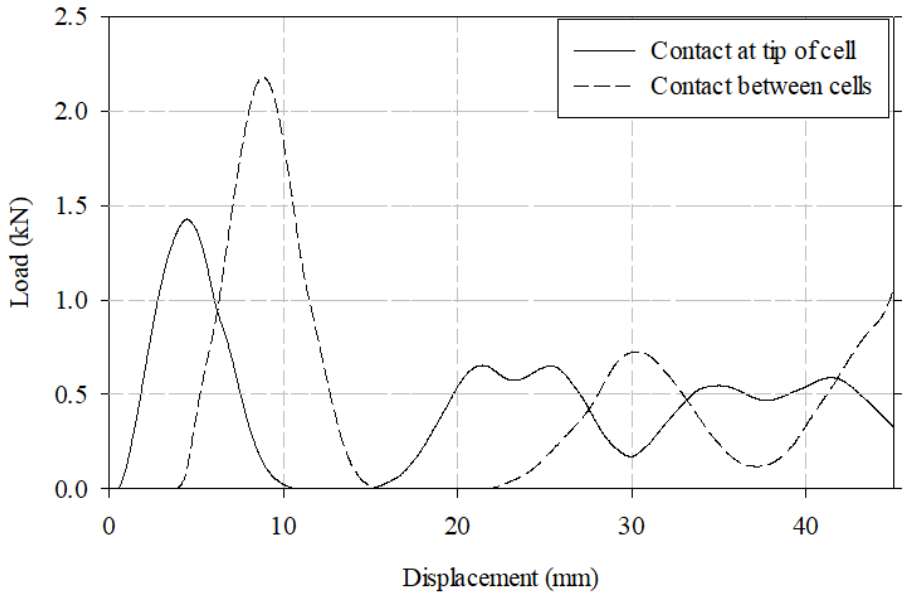

Figure 11. Result of legform test of Figure 10 with different impact location.

5.2. Pilot study designs

A myriad of structures with diverse working mechanisms were considered based on the information and results obtained from previous studies. Axial loading structures with uniform cross section are advantageous since they typically yield a highly repeatable load/displacement response. Axial cutting and inversion are especially favorable since these energy dissipation methods are capable of yielding a near-constant load/displacement response. However, these designs were rejected from further consideration since the deformation requires nearly perfect loading alignment to prevent buckling, and because of the low space efficiency of the deformation process, and the requirement to install a cutter and deflector which consumes both space and mass capacity within a given system. Moreover, the deformation modes of tube under axial loading could not be designed to have the self-adaptive characteristics discussed in earlier sections. Braided tubes with metal foam cores were also removed from consideration since the deformation requires excessive space for the structure to expand, which could not be provided for the targeted applications.

Based on the requirements of the study, many designs were tested. Some of them did not generate results as expected and were therefore removed from consideration. After a series of tests on designs inspired by previous studies had been completed, three typical structures were selected as preliminary designs for more detailed investigation and comparison: (1) stacked, alternating layers of hemispherical structure, (2) an array of adjacently positioned lateral rings and (3) a rounded top, self-stiffening rectangular array. All three designs were selected based on the knowledge from reviewing previous studies that potentially address the capabilities of self-adaptive energy absorption.

5.2.1. Preliminary design 1: Hemispherical structure

The first design utilized a similar concept of the axial loading of frustum, spherical shell and eggbox energy absorber. Layers of repeating hemispheres were stacked in an alternating fashion such that the hemispheres were in contact with each other as shown in (Figure 12(a)). When the structure is loaded, the hemispherical caps will compress into flat plates as their diameters increase. When multiple hemispheres are simultaneously compressed, adjacent caps will resist their respective radial deformations, acting as a boundary constraint, and therefore increasing the force required for plastic deformation.

In addition to this self-stiffening behavior, hemispherical cells were selected to ensure contact stability during the crushing process. As shown in Figure 16(a), an increasing degree of lateral shifting occurs throughout the structure at elevated deformations. A similar design with frusta instead of hemispheres was investigated and the lateral shift in upper layers during the legform test reduced the contact area between layers and caused the frustum to deform in an undesired shape. The hemispherical cells will maintain normal surface-to-surface contact more naturally than a similar conical or flat-

sided cell under shifting. This will result in the most efficient load path between the cellular chains which is crucial to a stacked energy dissipating structure.

Each layer of the hemispheres had a structural thickness of 10 mm, with 8 layers stacking to fit the design space available. The wall thickness was 2 mm. The center-to-center distance between adjacent hemispheres was 25 mm. The nodes at the bottom surface of the lowest layer were fully constrained against both translation and rotation. The nodes on the end surface perpendicular to the x-axis were constrained against translation in the x-direction and rotation along the y-axis and z-axis to represent a symmetry condition. The nodes on the end surface perpendicular to the y-axis were constrained to prevent translation in the y-direction to ensure the structure will not deform outside of the design space.

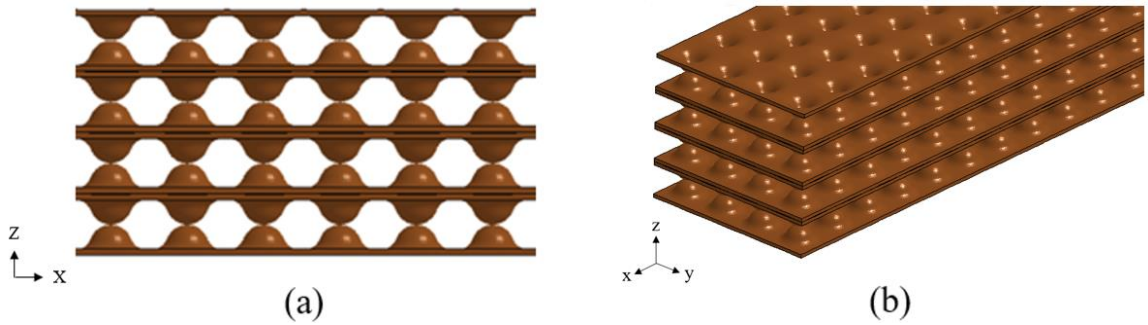

Figure 12. The hemispherical design in (a) front view, (b) isometric view.

5.2.2. Preliminary design 2: Lateral ring structure

The second design was inspired by the previous investigation where constraints were imposed on the lateral compression of circular tubes. The structure was composed of an array of rings that were loaded orthogonally to their axes (Figure 13(a)). Additionally, adjacent rows were offset laterally by the magnitude of their radii to increase the consistency of contact conditions. When a circular ring is compressed laterally and deformed, the radius parallel to the loading direction decreases with a corresponding increase in the transverse directions, yielding an elliptical geometry. This deformation phenomenon was not expected to occur for rectangular cells or other alternative flat-sided structures. Therefore, ring-like cells were chosen. This lateral deformation is significant for cases when multiple adjacent rings are loaded; transverse deformation will be suppressed due to interaction between neighboring rings. The tight contact between adjacent cells ensures that lateral resistance will occur instantaneously. This will result in a more complex bending mode, increasing the structure's rigidity and maximizing the potential energy absorption.

The diameter of the rings was 80 mm and the wall thickness was 3 mm. The structure was divided into 2 layers in y-direction and offset at 40 mm in x-direction. For this design, applying symmetry for the end surfaces and constraining the bottom surface as in hemisphere design was not suitable. Three solid walls were created on the bottom and two ends in the x-direction as shown in Figure 13(b), acting as a barrier for the design space. These walls had similar properties to the pendulum impactor both in element and material settings, and the contact definition between the energy absorber to the barrier walls was

also similar to the contact defined for the absorber to pendulum impactor as discussed in Section 5.1. The nodes of the walls where fully constrained for all degrees of freedom.

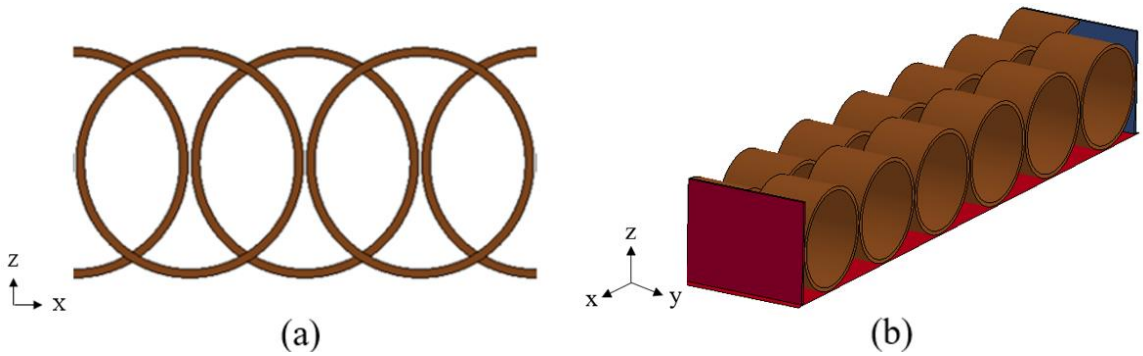

Figure 13. The lateral ring design in (a) front view, (b) isometric view.

5.2.3. Preliminary design 3: Round top cellular structure

The third design was based on a modification of the lateral ring structure design with an amalgamation of aspects from the first design. The upper section is elliptical and converges into a rectangular profile towards the lower section (Figure 14(a)). The intention of the design of the lower section was to produce a high load response in the initial stage of the deformation similar to square tubes under lateral loading in the pendulum test. When multiple cells are loaded, the neighboring cells will transfer the crushing load to the base and subject the structure to compression while resisting transverse deformation, artificially increasing the stiffness. This concept is discussed in further detail with consideration for the load path for a revised design in Section 6.1 of this document. Unlike either of the previous designs, this preliminary design utilizes energy dissipating cells which are fixed together. The additional constraints were more feasible with this proposed geometry and were implemented to further enhance the overall stiffness of the structure.

The wall thickness of the lower, rectangular section was 4 mm and the thickness of the upper section was 2 mm. In the upper section of the structure, the round top has a radius

of 10.7 mm and the oblique wall made a 68.5 degrees angle with the x-y plane. The height of the lower section was 35 mm and the width of the cell in the x-direction was 50 mm. The full structure consists of 9 complete cells and 2 half-cells, one at each end of the structure, connected at the lower section of the structure over the span in the x-direction. The nodes of the cutting surface of the half-cell were constrained to prevent translation in the x-direction and rotation along the y and z axes for symmetry. The bottom surface of the structure was fully constrained. Since the contacting surface at the top of structure was discontinuous and the gap was relatively large, the structure was divided into 4 layers in the y-direction and offset by 12.5 mm in the x-direction between each layer.

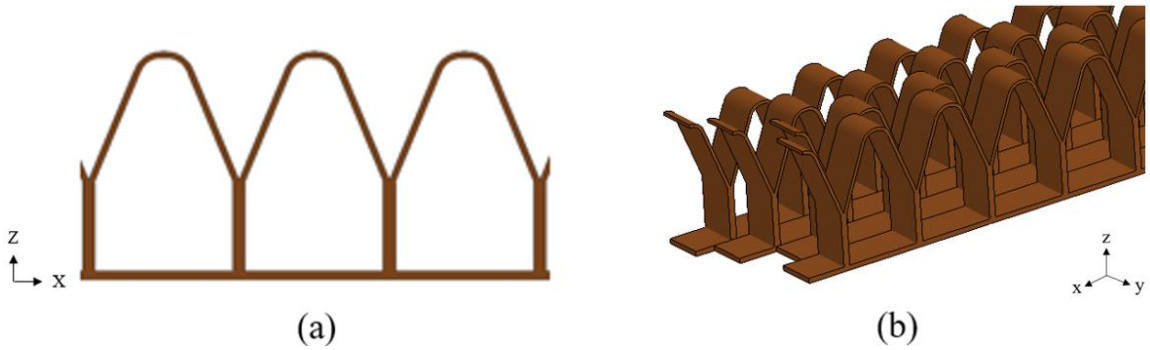

Figure 14. The round top cellular design in (a) front view, (b) isometric view.

5.3. Pilot study results

The pilot study emphasized a comparison between the force/displacement responses and deformation modes in both testing configurations. Following the comparison, the most preferable design was selected and modified based on the critical findings. The following parameters were utilized to assess the performance on each design: consistency of the load/displacement response in the legform test, the instance of peak energy absorption in the pendulum test and the ratio between the average legform and pendulum loads for each respective design.

5.3.1. Hemispherical structure

The load/displacement response of the pendulum test for the hemispherical structure in Figure 15 displayed an increasing load as the impactor progressed and the hemispherical geometries were progressively compressed into flat sheets. The crushing load reached 33 kN at 32 mm, followed by a minor fluctuation between 32 mm to 50 mm, then increased rapidly as the space between the impactor and bottom surface became occupied by the compressed material. During the legform test as shown in Figure 16(b), the contact area increased as the impactor traveled downwards, this resulted in an increased load response proportional to the increase in contact area. The load/displacement response in the legform test increased continuously throughout the simulation, reaching approximately 10 kN at 60 mm of displacement.

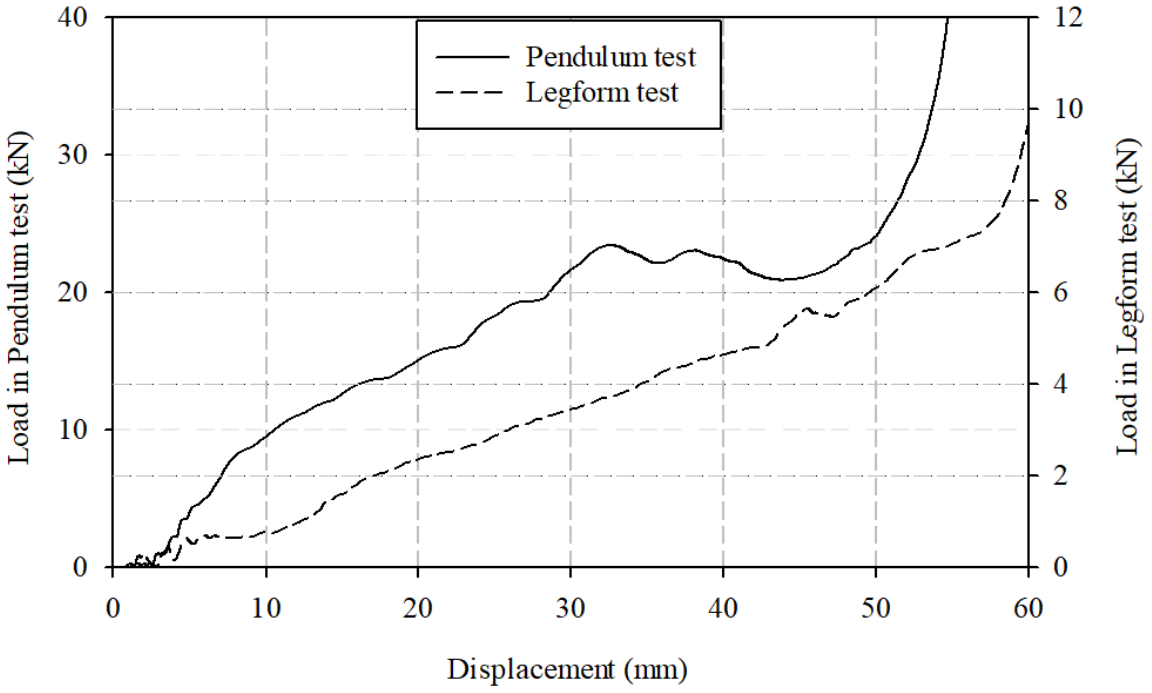

Figure 15. Load response versus displacement for hemispherical structure design.

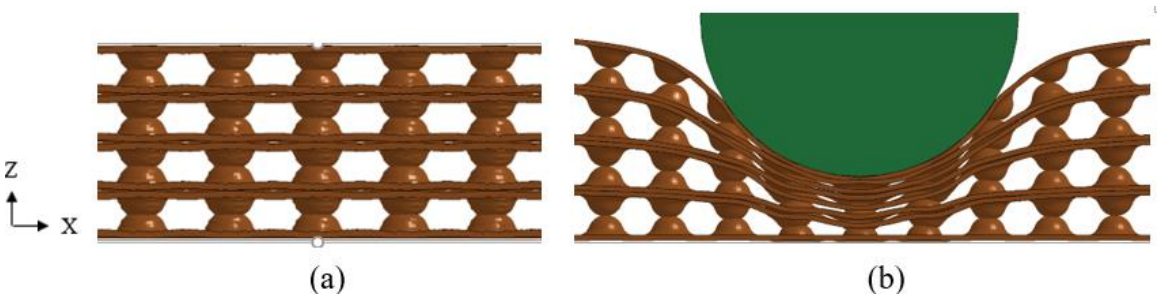

Figure 16. Impact deformation of hemispherical structure for (a) Pendulum test at 20 mm and (b) Legform test at 50 mm.

5.3.2. Lateral ring structure

For the lateral ring structure test result (Figure 17), the load/displacement response in the pendulum test experienced a near-zero crushing force within the first 5mm of displacement, followed by a quasi-linear increase up to 20 mm. The first peak load and corresponding maximum energy absorption occurred at 26.4 mm of deformation, with the energy absorber transitioning from a ring-like geometry to rectangular cells as shown in Figure 18(a). A resultant peak load of 11 kN was observed. The second peak load of 16 kN, and global maximum for the response, occurred beyond 50 mm of displacement. In contrast to the pendulum test, the rings in the legform test were not constrained laterally under compression (Figure 18(b)), resulting in significantly less resistance as illustrated by the load/displacement response. Additionally, as the deformed rings expanded laterally adjacent rings were shifted; the contact area between the impactor to the adjacent rings was reduced due to this behavior. The load response in the legform test displayed a peak load of 1.5 kN and average load of 0.72 kN.

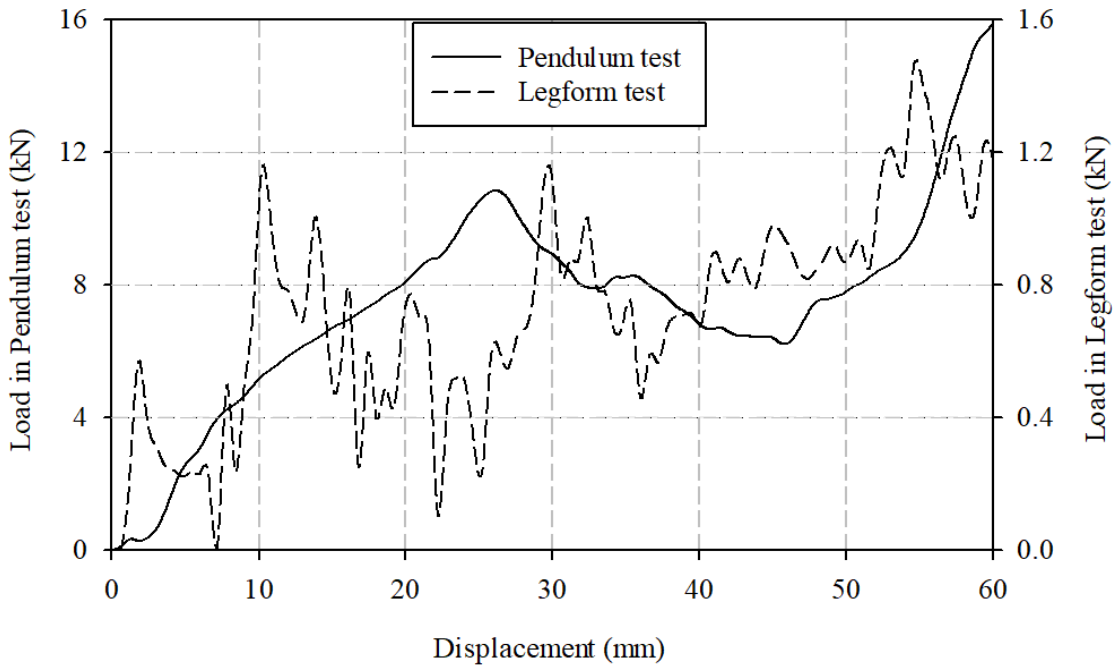

Figure 17. Load response versus displacement of lateral ring structure design.

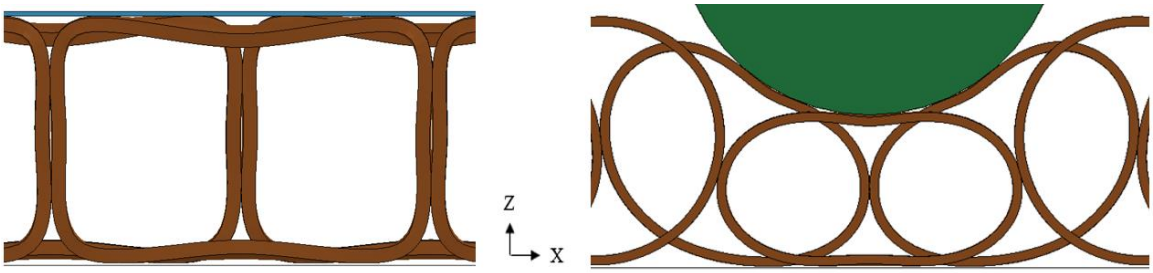

Figure 18. Impact deformation of lateral ring structure for (a) Pendulum test at 26 mm and (b) Legform test at 35 mm.

5.3.3. Round top cellular structure

The load/displacement curve from the pendulum test on the round top cellular structure (Figure 19) exhibited local maxima of 32.0 kN at 17 mm and 60 mm. The first peak load occurred when the rounded upper section was compressed into a geometry with higher stiffness at 17 mm (Figure 20(a)). In the legform simulation, two impact scenarios were presented with unique impact locations, all other boundary conditions were common.

The first scenario considered impact directly above a vertical wall in the lower section. High compressive loads were observed as the impactor approached the vertical wall (Figure 20(b)). In the second scenario, the impactor was offset to the side of the wall (Figure 20(c)). These loading cases will be referred to in later sections as scenarios 1 and 2, respectively. In this test, the wall was subjected to a bending load which resulted in a significantly lower load response. Both scenarios of the legform impact possessed a similar load response below 2 kN and prior to 45 mm of deformation; beyond 45 mm, the load response remained consistent at approximately 1.8 kN until termination in scenario 2. In contrast, scenario 1 displayed a sudden increase in load to 7.0 kN for the remainder of the test. It is important to note that the scenario 1 accounted for less than 10% of the possible impact occurrences.

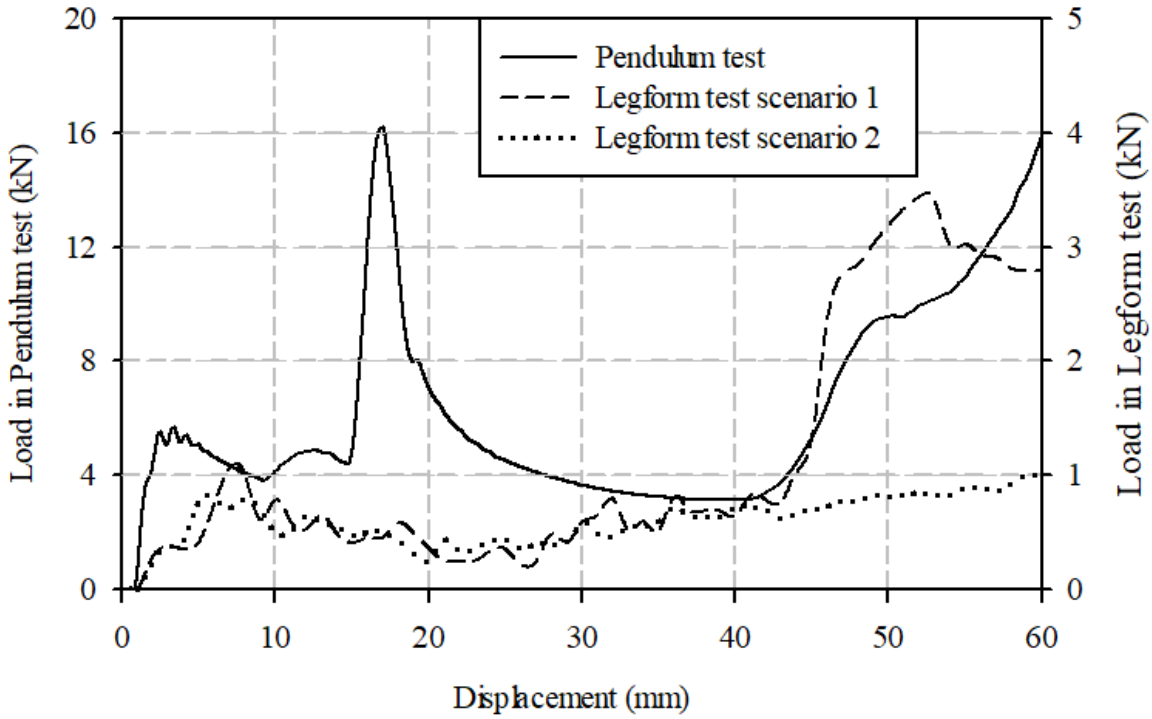

Figure 19. Load response versus displacement for round top cellular structure.

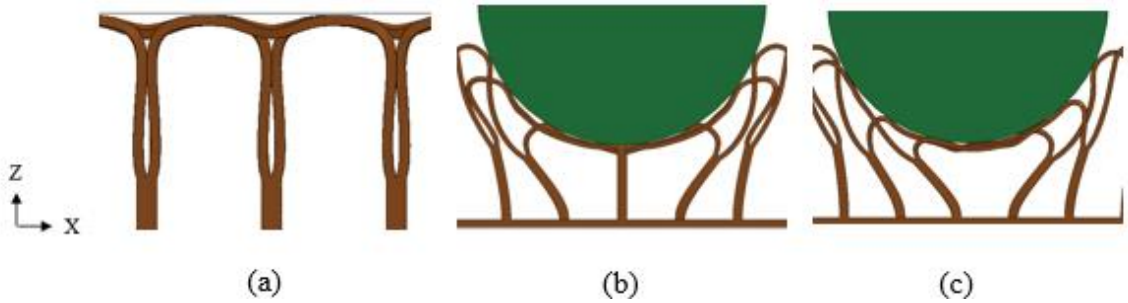

Figure 20. Impact deformation of round top cellular structure for (a) Pendulum test at 17 mm, (b) Legform test scenario 1 at 42 mm and (c) Legform test scenario 2 at 42 mm.

5.3.4. Comparison of pilot study results

All preliminary designs functioned as expected in the pendulum test with the self-stiffening requirements. The hemispherical structure possessed a self-stiffening geometry prior to the initial deformation while the lateral ring structure and round-top cellular structure required some deformation to achieve a self-stiffening structure. To evaluate the performance of the 3 designs the following parameters were considered: the consistency in load during the legform test, the occurrence and locations of peak energy absorption in the pendulum test, and comparison between the mechanical responses observed during the legform and pendulum tests of each design individually.

For the legform test, the hemispherical structure experienced a steady, gradual increase in load throughout the test. The lateral ring structure and the round-top cellular structure both experienced a rapid increase in load initially, followed by a short decrease in the load response and finally, a slow increase until termination. For the pendulum test, the hemispherical structure absorbed the majority of the energy in the second half of the test, between 30 mm and 60 mm. The lateral ring structure displayed a local peak of load at 26.4 mm of displacement which offered a minor increase in energy absorption between 25 mm and 30 mm of deformation; the round top cellular structure underwent peak energy

absorption between 15 mm and 20 mm of deformation with a local peak load of 16 kN. The ratio of average loads between the pendulum tests and legform tests for the hemispherical structure, lateral ring structure and round top cellular structures were 5 to 1, 9 to 1 and 10.2 to 1, respectively. For each scenario, the average load (P_m) was calculated as a function of load (P) within the displacement (S) domain as per the method demonstrated in equation 1.

$$P_m = \frac{1}{S_{total}} \int_0^{S_{total}} P(S)dS \tag{1}$$

However, since the load/displacement responses were generated from discrete data points rather than continuous functions it was impossible to perform a true integration of the data. Therefore, the average load was numerically approximated using equation 2.

$$P_m = \frac{1}{S_{total}} \sum_{i=1}^{n-1} (S_{i+1} - S_i) \cdot \left(\frac{P_{i+1} + P_i}{2}\right) \tag{2}$$

These average loads and the complementary peak loads are summarized in Table 1. It is important to note that multiple maximum loads were present in pendulum tests of the lateral ring structure and rounded top cellular structure; the results are therefore displayed in separate rows.

Table 1. Key parameters from the load/displacement responses of preliminary designs.

	Legform test		Pendulum test		
Preliminary designs	Peak load (kN)	Average load (kN)	Peak loads (kN)	Displacement at peak load(s) (mm)	Average load (kN)
Hemispherical structure	10.0	4.0	23.0	32.0	20.5
Lateral ring structure	1.5	0.7	10.8* 16.9	26.4 60.0	6.5
Round top cellular structure	2.0	1.2	32.0 31.6*	17.0 60.0	12.2

Note: * indicates that the peak load represents a local maximum.

Comparing the legform test results, the round top cellular structure demonstrated the most consistent load/displacement response. Among the pendulum test results, the round top cellular structure could absorb the greatest quantity of energy in the early stages of deformation. This is demonstrated in Table 1 by a primary peak crushing load of 32.0 kN at 17.0 mm of deformation for round top cellular structure compared to 23.0 kN at 32.0 mm and 10.8 kN at 26.4 mm for the hemispherical and lateral ring structures, respectively. When comparing the average loads between the pendulum and legform tests of each individual design, the round-top cellular structure also possessed the greatest pendulum to legform force ratio. A summary of this comparison is provided in Table 1. Since the round-top cellular structure displayed the most favorable results with respect to the previously described considerations, it was therefore selected for further revision and study. Although alternative scenario 2 of the legform test for round top cellular structure could potentially result in a high load response, the occurrence was less than 10%; reduction of this behavior should be an important consideration for further study.

From the results of each design in the pilot study, it was determined that the round top cellular structure demonstrated the greatest resistance to deformation when the load

was applied along the vertically orientated wall. Such effects were observed in the pendulum test for the lateral ring displayed in Figure 18(a) and round top cellular structures illustrated in Figure 20(a), where the load response increased. With the intention of minimizing deformation during the pendulum test, significant energy absorption in the early stages of pendulum impact were desired. The geometry at the upper impact surface was considered utilizing a flat top with sharp corners which form trapezoidal cells rather than the previously utilized rounded cap. This revision was expected to shift the peak load observed for the round top cellular structure to the early stages of deformation in the displacement domain.

6. MODEL VERIFICATION AND VALIDATION

6.1. Revised design selected for further study

A preferred structure based on the preliminary study was developed and is presented in Figure 21, with the arrows representing the estimated load path within the structure for the two different loading conditions. The load acting at the impacting surface will follow the load path indicated to generate unique, tailored loading conditions within the lower section of the structure. When a single cell is loaded the load transferred to the lower section will introduce unbalanced lateral forces and cause the lower section of the cell to buckle, thus resulting in a less stiff response that is more susceptible to yielding in a legform impact. Such a response is favorable when considering pedestrian safety. When the structure is loaded at multiple cells simultaneously, the lateral force components from adjacent cells will neutralize each other and the absorber will experience pure compression until buckling occurs. A beam is capable of withstanding greater axial loads when no lateral force is present before buckling. Similarly, this preferred structure is also stiffer when loaded at multiple points before experiencing large scale deformation and the initial high stiffness is no longer present. The resultant design is therefore capable of passively adapting its response to prioritize pedestrian safety in a localized impact or energy dissipation, and therefore minimize deformation in a vehicular impact. The upper half of the structure with trapezoid shape will be referred to as the upper section and the lower half of the structure will be referred to as the lower section in this thesis.

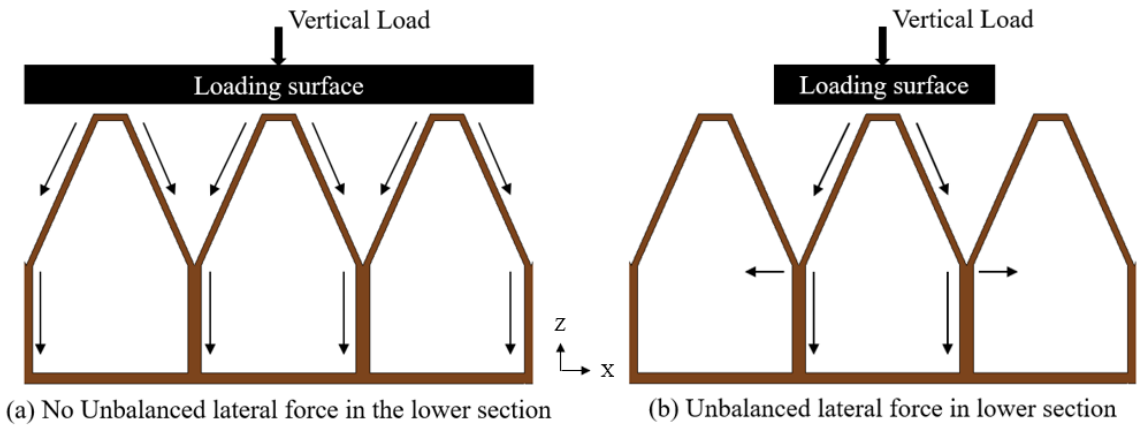

Figure 21. Preferred structure showing the expected load path in conditions with (a) large area loading and (b) single cell loading.

6.2. Verification and validation approach

Validation experiments were performed to test the predictive capabilities of the finite element model and the corresponding analysis. The geometry presented in the model was scaled down in size for convenience. Although the study was conducted using a proprietary polymer as the material, it was impossible to obtain properly manufactured plastic test specimens in a reasonable quantity. Therefore, specimens were fabricated from mild steel for the physical testing. The finite element model was also revised to match the physical testing in specimen size, material properties and testing conditions. To generate a more reliable comparison between the FEA and physical testing, the tests were performed considering the quasi-static engagement of the passive adaptive structure and two crushing entities including: (i) a large contact flat impactor and (ii) a cylindrical roller.

For validation purposes, the deformation of the test specimen was recorded, with tracker dots marked on the specimen as shown in Figure 22. ProAnalyst© Motion Analysis was used to track the path of the tracker dot and used to compare with the path of a node

at the same location in the FEM. The load and displacement were also recorded and compared to the FEA result.

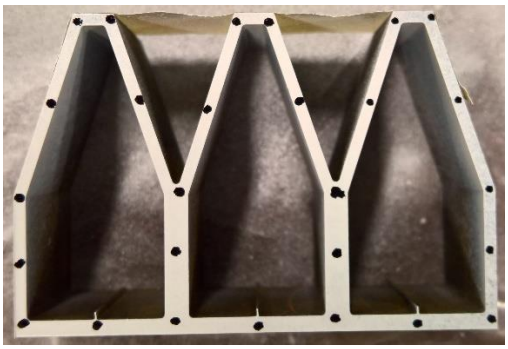

Figure 22. Specimen with tracker dots.

To verify the FEMs generated in this study, an extensive investigation of each model's energy balances was also conducted. The major energy components were plotted with respect to time; this included the following terms: kinetic energy, internal energy, sliding energy and total energy. In this study, the deformation, and by extension the full magnitude of energy dissipated, was expected to be attributed to external work caused by boundary prescribed motion. Therefore, the average ratio of total energy with respect to external work computed by LS-DYNA was also calculated to quantify the verification efforts. Ideally, this value should be unity to satisfy the law of Conservation of Energy. In mathematical prediction, the sum of kinetic energy, internal energy, and sliding energy at initial stage of the test plus the work done during the test would be equal to the sum of these energies at the end of the test. The standard deviation was also computed to assess consistency. Since the test was performed quasi-statically, the contact forces between the impactor and specimen were expected to be almost identical to the contact force between the specimen and support plate. Also, the average ratio of the kinetic energy to internal energy cannot exceed 10% for a problem to be considered quasi-static. For brevity, the

verification data was only included for the model generated for the validation experiments. However, a similar approach was utilized for all other models presented in this thesis.

6.2.1. Test of material property

The material model used for the FEA were supplied by the industrial partner, which was assumed to be accurate and accepted as a valid representation of the physical property of the PP T-20. Since the material was not available and manufacturing test specimens with such material was not viable, a common grade of steel was chosen as the specimen's substitute material in the validation study. The ANSI 1020 steel could be obtained easily and cut with EDM to obtain a specimen with accurate dimensions at a reasonable cost. However, the purchased steel does not have specified mechanical properties from the supplier. Since the material model of the FEA requires the stress versus strain behavior of the material, a set of tests to obtain the mechanical properties of the material was required.

A group of 10 tensile specimens was cut to perform the test. To minimize the possible difference between the tensile specimens and validation test specimen, both were EDM cut from the same block of steel. The dimensions of the tensile specimen were designed following the ASTM testing standard [32] as shown in Figure 23. The sub-sized specimen geometry was used, and the thickness was designed to be 1.5 mm. Since the material was a hot rolled steel block, the property variation due to directionality was neglected.

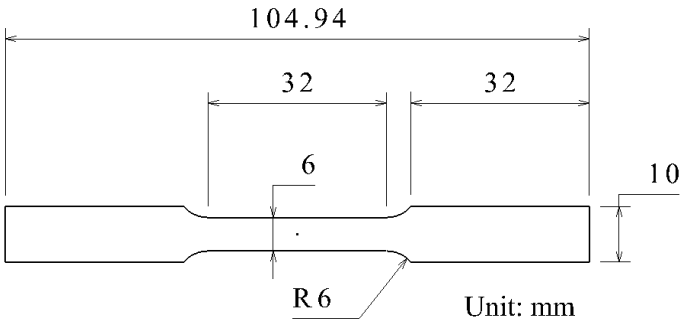

Figure 23. Dimensions of tensile specimen.

Prior to the test, the surface of the gauge section of the specimen was painted with white background and black random dots for DIC and/or digital image analysis. During the test, a 5 mega-pixel video camera was utilized to record the deformation of the gauge section of the tensile specimen. The recorded video was used by MTS video extensometer software act as an optical extensometer. A physical clip-on extensometer was also present to obtain data and compared with the electronic results. The clip-on extensometer possessed a nominal gauge length of 25 mm and was able to measure up to 12.5 mm displacement. The material was expected to have less than 20% of maximum strain, therefore the extensometer was capable of capturing the length change of the specimen during the entire test. An MTS universal testing machine was used to perform the test; the specimen was mounted vertically. The lower end grip was stationary while the upper grip was attached to a load cell and installed onto the cross head.

All critical specimen dimensions were measured with a digital caliper before each specimen was tested. Five measurements of the width and thickness were taken along the gauge section of each specimen. When the specimen was mounted on the testing machine, the lower grip was tightened before the upper grip. After the specimen was locked to the grips, the pre-loading was released by slight lowering the crosshead position, which was

controlled by the wheel on the control pad. The digital video camera was setup on the painted side of the specimen. The physical extensometer was calibrated then clipped onto the other side of the specimen. The tracker of the optical extensometer was placed near the clippers of the physical extensometer on the symmetry axis of the specimen. During the test, the speed of the crosshead was set to 2.5 mm/min. The termination of the test was primarily controlled by the load response and was such that the crosshead stops moving when the load drops to 90% of the maximum load of the individual test. The video was recorded at 1 frame per second. The load, displacement and strain extensometer readings were collected at 25 Hz.

After the tests were complete, the engineering stress was calculated from the load collected during the test and cross-section dimensions measured before the test. The engineering stress versus engineering strain behavior obtained with both physical and optical extensometers are shown in Figure 24 and 25, respectively. Comparing the data obtained from the two extensometers, the readings were identical prior to the maximum stress; after the maximum stress of each test was reached, the specimen started to neck, and the optical extensometer began to lose focus of the specified optical tracking region due to large deformation. Since the video was recorded at 1 frame per second, the result of optical extensometer appears to be discrete compared to the transducer results. Considering the results from the optical extensometer, the readings of the physical extensometer up to the maximum load were considered accurate, and were used to generate the material model for validation of the FE model.

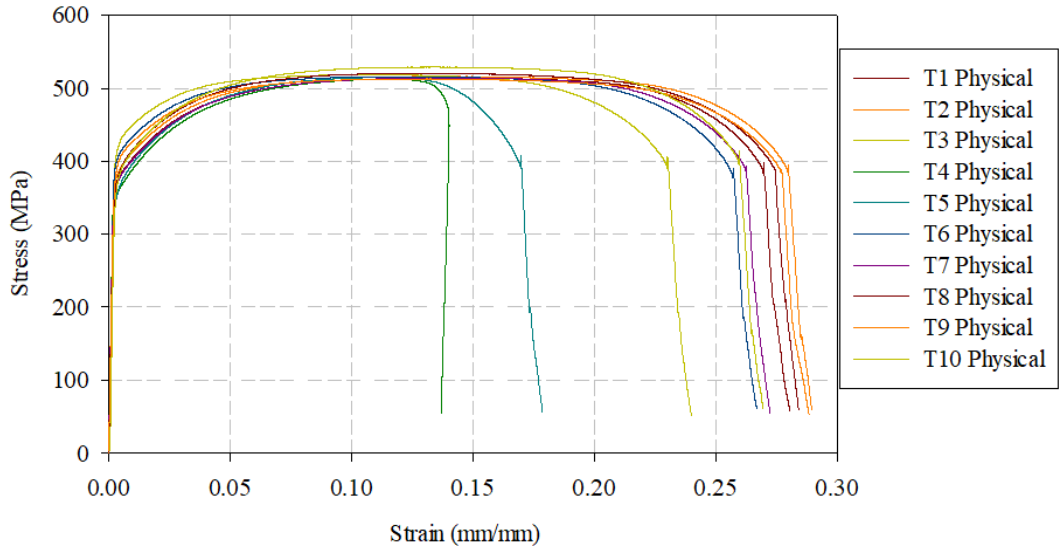

Figure 24. Engineering stress versus strain for physical extensometer result.

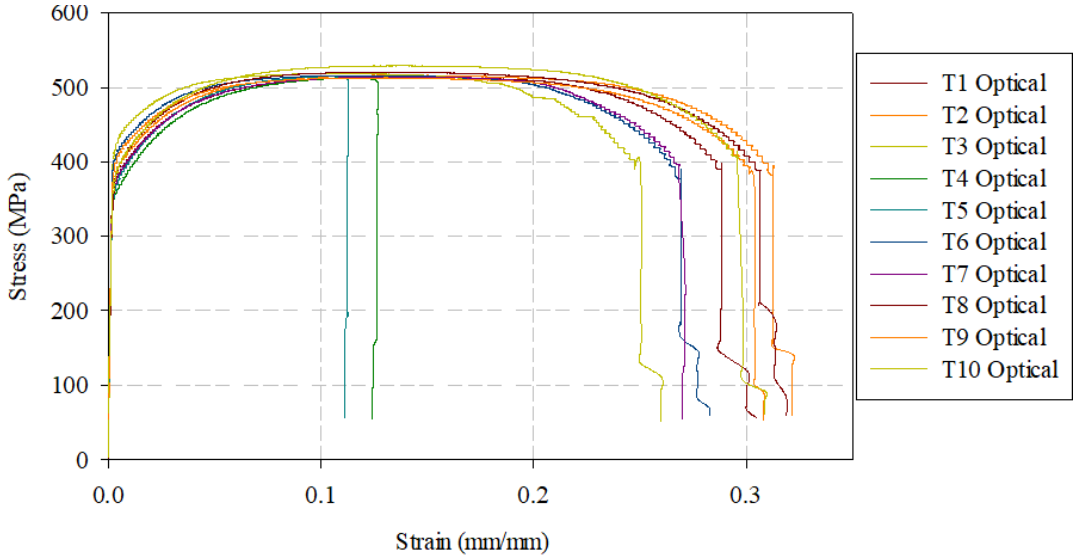

Figure 25. Engineering stress versus strain for optical extensometer result.

The elastic behavior was obtained by linearly interpolating the lower section of the elastic region observed in the stress/strain plot, the slope of the interpolated line was recorded as the elastic modulus and the stress where the test result deviated from the interpolated line was recorded as the yield strength. Thus, a proportional limit definition was used to determine the yield strength. Among the 10 tests, the elastic modulus was

found to be between 180 GPa to 200 GPa with an average of 187 GPa; the yield strength ranged between 350 MPa to 400 MPa with an average of 365 MPa. The plastic behavior varied slightly after yield then converged again when the maximum stress was reached. Between the tests, 9 out of 10 tests demonstrated maximum stresses between 512 MPa to 520 MPa, with one outlier of 529 MPa. Although the maximum stress was similar, the strain to failure was different. The region of strain where maximum stress occurred ranged from 0.11 to 0.15. Test 2 results were selected to be used for generating the material model since it had aspects close to the average among all the results. The true stress and true strain were calculated with Equations 3 and 4. The effective plastic strain was calculated with Equation 5 and true stress corresponding to the strain was used directly as effective stress.

$$\sigma_{True} = \sigma_{Eng} * (1 + \varepsilon_{Eng}) \tag{3}$$

$$\varepsilon_{True} = \ln(1 + \varepsilon_{Eng}) \tag{4}$$

$$\varepsilon_{Effective\ Plastic} = \varepsilon_{True} - (\frac{\sigma_{True}}{E}) \tag{5}$$

Since the coefficient of friction between the steel and impactors was unknown, a simple slide test was performed to estimate the value. The impactor was placed with impacting surface facing upward. A plate cut from the same steel block for the test sample was placed on the impactor surface, and weights with mass of 5 kg was placed on top of it. Dragging force required to slide the plate was measured with a digital hanging scale. The dynamic and kinetic coefficient of friction was estimated to be 0.25 and 0.3 respectively.

6.2.2. Validation test setup

The specimens used in the physical tests were fabricated by cutting the geometry from a block of steel with an Electric Discharge Machine (EDM) to the critical dimensions as shown in Figure 26. The tests were performed by utilizing an MTS universal test system. In the flat impactor apparatus, the specimen was compressed between two platens as shown in Figure 27(a). In the roller impactor test setup, the specimen was set on a platen and compressed by a roller with a 50.8 mm diameter from above as shown in Figure 27(b). The top platen and roller were fixed onto the crosshead and displaced at a rate of 5 mm/min; the duration of each test was 5 min. The displacement data for the impactor was read from the displacement of the crosshead on the MTS system and the load response data during the compression tests was read by a 150 kN capacity load cell mounted onto in the crosshead. The load/displacement data was recorded at 10 Hz. The video of the test was captured with a 5 mega-pixel video camera that was synchronized with the MTS system. The video was recorded with a resolution of 2560 by 1960 pixels^2 at a 1 Hz sampling rate.

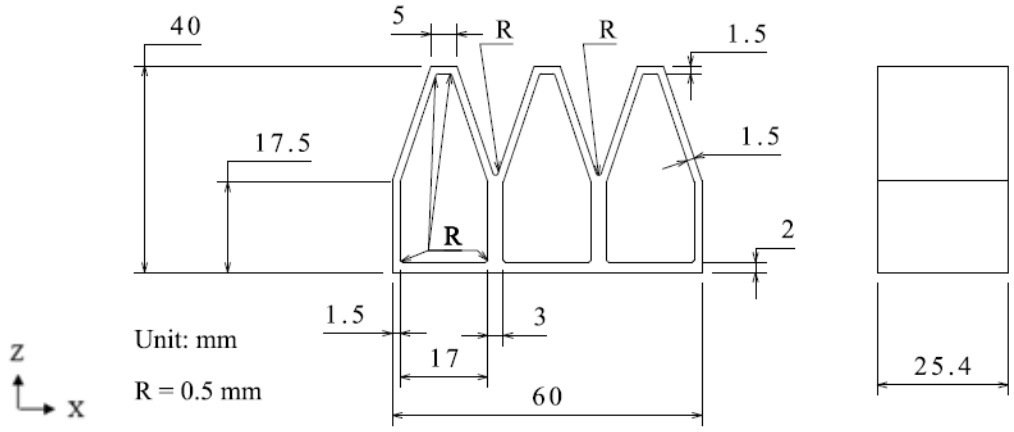

Figure 26. Dimension of testing specimen.

Figure 27. Test setup of (a) flat platter compression, (b) roller compression.

The FE simulation generated for comparison was modeled according to the physical apparatus, with a time scale factor of 100 applied to the simulation process. In order to represent the physical test specimen accurately within FEM, the material data was obtained from tensile tests discribed in Section 6.2.1. The material properties will be disccused in the next section.

6.3. Finite element model

The finite element models included three major components: the impactors, a rigid base support and the energy dissipating structure. Figure 28 shows a schematic of the FEM. The flat impactor was modeled as a flat plate and the round impactor was modeled with a cylinder. The energy dissipating structure has the same geometry as the test specimen.

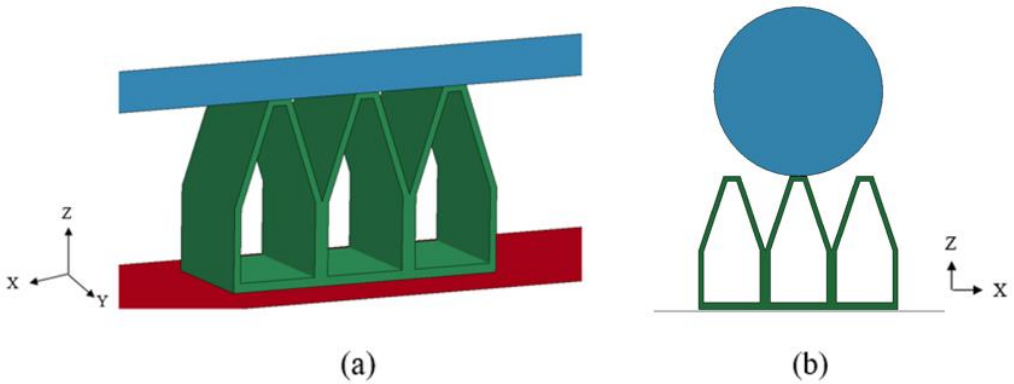

Figure 28. FEM of (a) flat platter apparatus and (b) roller apparatus.

6.3.1. Element discretization

Both the flat impactor and base support of the test were modeled as flat plates with shell elements, and the round impactor was modeled with solid elements. Both impactors and the base surface were modeled as rigid bodies since negligible deformation in these components was expected. The flat impactor and base surface utilized elements with an average size of 2 mm by 2 mm. The roller was modelled with 48 elements along the radius. The energy dissipater was also modeled with solid elements with 3 elements through the wall; the minimum element depth through the wall was 0.5 mm. The largest element aspect ratio was 2.5 located at the upper portion of the structure, all other elements in the structure generally possessed an aspect ratio of 2 with an average element size of 1 mm by 1 mm by 0.5 mm. The minimum characteristic length of the elements within the dissipater was 0.4 mm. A fully integrated, selectively reduced element formulation that was designed to compensate for large aspect ratio, element formulation "-1" in LS-DYNA [31], was utilized for the energy dissipater. This element formulation utilizes a modified Jacobian matrix where the aspect ratio was added as a factor in the calculation. Due to the large element deformation throughout the impact simulation, the element formulation with aspect ratio considerations in the calculation matrix was a reasonable selection to generate more accurate results.

6.3.2. Material properties

Piecewise linear isotropic plasticity material model, MAT24 in LS-DYNA, was used to model the energy dissipating structure. In this material model, the density, elastic modulus, Poisson's ratio, yield stress and a set of effective stress versus effective plastic strain data points were used to define the mechanical behavior of the material. The

commonly accepted steel properties of density and Poisson's ratio were defined as 7830 kg/m^3 and 0.29, respectively, while the elastic modulus, yield stress and effective stress versus effective plastic strain were obtained from tensile tests discussed in Section 6.2.1. The following values were obtained from these tests: an elastic modulus of 193 GPa, yield stress of 317 MPa and the effective stress versus effective plastic strain response is shown in Figure 29. The effective plastic strain property beyond 0.13 was not specified in the material property, which will be linearly interpolated by the FEA solver if needed. Material failure was not considered since no precise strain to failure value could be determined. This was assumed to be acceptable since no fracture was observed on the tested physical specimen. In the FEA result, the maximum effective plastic strain was 0.99 at the end of flat plate compression. A rigid material model was implemented for the impactors and base support. The density, elastic modulus and Poisson's ratio were defined as 7830 kg/m^3, 207 GPa, 0.29, respectively, for all rigid entities.

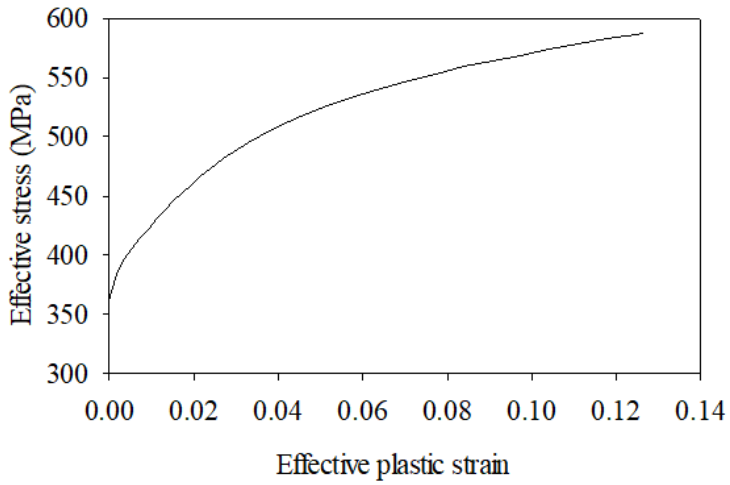

Figure 29. Effective stress versus Effective plastic strain of mild steel.

6.3.3. Contact algorithms

The contact algorithm defined between the impactors and the energy dissipater was a segment based, automatic surface-to-surface contact [31]. In this contact definition, the dissipater was the slave and the impactors were the master since the dissipater possessed a more discrete mesh. The friction coefficients were defined as 0.3 and 0.25 for static and dynamic conditions, respectively, which were experimentally measured by a simple sliding test setup. The exponential decay coefficient set to 10^5 for all contact definitions which produced a rapid transition between the static and dynamic coefficients of friction. The optional card "SOFT" was activated with default parameters to invoke segment-based contact and reduce penetration. Contact between the dissipater and base utilized similar parameters. Automatic single-surface contact algorithm was also defined for the dissipater to account for possible self-contact during compression, though no self-contact was observed during the test. The single surface contact included friction coefficients of 0.5 and 0.4 for static and dynamic conditions, respectively.

6.3.4. Boundary conditions and simulation environment

Several boundary conditions were implemented on the impactors and base support. The impactors were constrained to only allow for translation in the z-axis as shown in Figure 28. The base was fully constrained against translation and rotation. Impactor displacement was defined with a boundary prescribed motion similar to the physical testing apparatus. The model was simulated with explicit analysis and time scaling, so that the velocity of the impactors was greater in the simulation than in the physical test by a factor of 1000, which was approximately 83.3 mm/sec. The analysis was performed with LS-DYNA, shared memory processing (SMP), double precision solver R8.0.0. Data from

the simulation results including energy terms and contact forces was output at 10 kHz where a total of 3000 sets of data were collected. By carefully observing and comparing the load/displacement responses, it was determined that the data collected provides a reasonably accurate representation of the expected test results.

6.4. Results and discussion

6.4.1. Model verification

Model verification was completed based upon an energy balance considering the system energies and external work applied in the simulation. Figure 30 provides output from the simulation regarding internal, sliding, kinetic and total energies as well as external work. The work/energy balance response was observed to be appropriate where the external work is approximately equal to the total energy being equal to the sum of the kinetic, sliding and internal energy terms. The previously discussed element formulations which were implemented do not allow for hourglassing; therefore, consideration for this effect was not necessary. The behavior of the sliding energy response provides further confidence in the validity of the model since this term was increasing or reached a plateau as the simulation progressed with the absence of negative values.

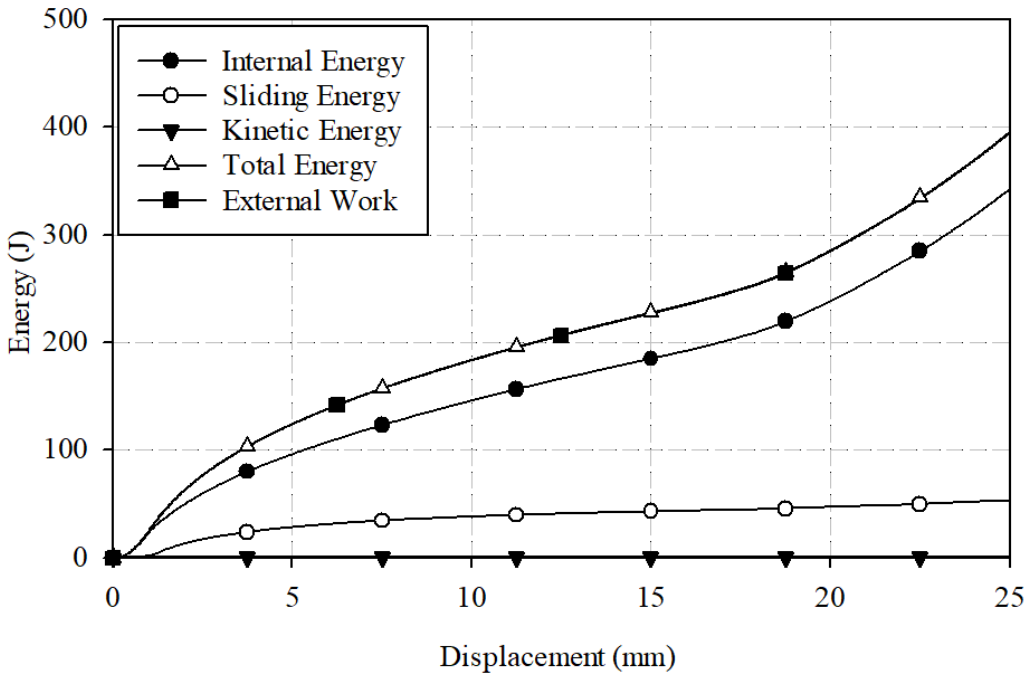

Figure 30. Energy terms with respect to displacement for validation FEM.

To quantify the correlation between these terms, the average ratio between the total energy and external work for each cycle was computed, along with the standard deviation. These values were 1.003 and 0.001, respectively. As mentioned in the methodology of this investigation, a value of unity implies a true conservation of energy. The average ratio between kinetic and total energy was 0.42% for the validation simulation considering the entire time domain. Additionally, the contact forces between the impactor and the upper surface of the test specimen were compared with the contact force between the support plate and lower specimen surface by evaluating the relative difference between them by utilizing Equation 6. However, since the results from the FEA were generated as discrete data, Equation 7 was used to estimate the true value. The relative difference between the contact forces at the upper and lower surfaces of the specimen was approximately 0.23%, which demonstrates that these contact forces were nearly identical. This further supports that the deformation event was quasi-static in nature.

$$relative\ difference = \frac{1}{S}\int_0^S \left|\frac{y(x)-Y(x)}{Y(x)}\right| dx * 100\% \tag{6}$$

$$relative\ difference = \frac{1}{L}\sum_{n=1}^{n=L} \left|\frac{y(x_n)-Y(x_n)}{Y(x_n)}\right| * 100\% \tag{7}$$

6.4.2. Model validation

Prior to the validation of the FE model, a validation of the material model was performed to ensure the material card generated was a suitable representation of the steel used in the physical tests. A FEM was created mimicking the tensile test setup and the tensile load versus strain at the gauge section was collected and compared with the physical test data. The relative difference calculated with Equation 7 between the FE results and physical tests prior to the strain where necking initiated in the physical test; this was

approximately 1.5%. Since the results were almost identical, the material model was accepted.

The deformed specimens were compared visually with the simulation results to determine if the overall deformation was consistent with the FE predictions. As shown in Figure 31, the deformation was observed to be similar between the physical test and FEA results for the flat platform compression scenario. Comparison of predicted and experimental results for the roller compression test revealed a slight difference between the final deformed structures, as shown in Figure 32. The specimen of the physical test deformed asymmetrically where the middle cell appeared to be shifted laterally during the compression. An examination of the recorded digital photographs taken during the experimental testing revealed a slight rotation about the roller's axis during the deformation. The asymmetric folding on the right side of the physical test specimen was attributed to this minor degree of rolling motion.

Photos recorded during the compression tests were processed by ProAnalyst© Motion Analysis to extract the displacement of the marked location on each specimen. Nodal motion was tracked at similar locations for comparison. The extrapolated paths were compared and are presented in Figures 33 and 34, for the flat platter and roller compression conditions, respectively. Note the dashed line presented in Figure 33 and 34 represent the path of the experimental tracker dot while the solid line indicates the nodal displacement predicted by FEA. The tracked dot and node paths in Figure 33 demonstrated a high degree of similarity between the simulations and physical experiments. In the roller compression test, the path of the tracker dot on the physical specimen indicated the left side of the specimen has experienced less deformation, with a similar deformation mode compared to

FEA predictions (Figure 34). The path of the tracker dot located in the upper section of the middle cell exhibited some deviation, but was noted not to be too significant until the last 5 mm of deformation. It was anticipated that non-symmetrical deformation observed in the physical roller test would not adversely influence the load response significantly.

Figure 31. Deformed shape after flat platter compression.

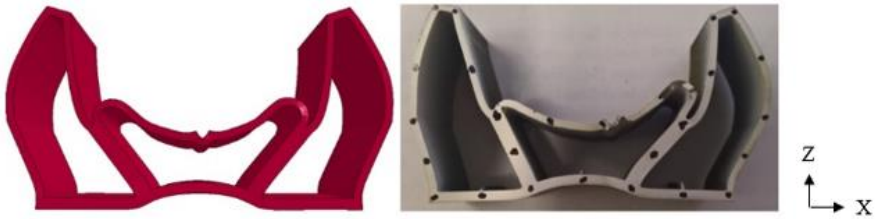

Figure 32. Deformed shape after roller compression.

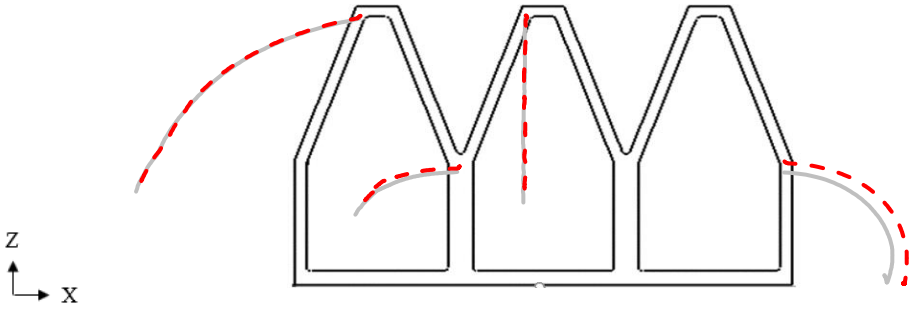

Figure 33. Path of tracked dots/nodes in flat platter compression.

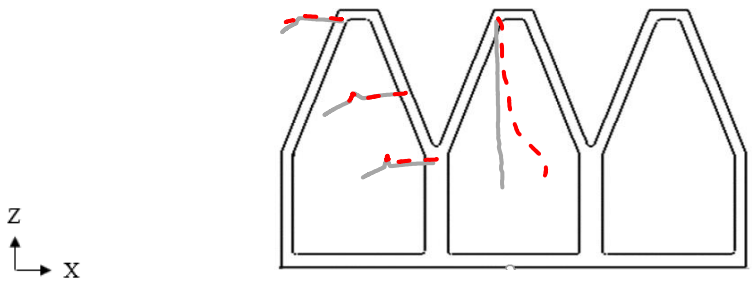

Figure 34. Path of tracked dots/nodes in roller compression.

The load/displacement responses obtained from the physical tests and simulations were compared to validate the accuracy of the numerical model. Figures 35 and 36 compares the FEA result to physical test result of flat platform and roller compression, respectively. The load/displacement response for the flat platform compression test displayed a rapid increase in load as the compression initiated, with a peak load of 44 kN and 1.2 mm of displacement, followed by a decrease to 12 kN at 5 mm of compression. The load dropped gradually until the impactor reached 17 mm of crushing distance. A secondary increase, at approximately 18 mm, was observed beyond this point as the upper section of the specimen was completely deformed and the adjacent cells contacted the lower platen (Figure 37). The load continously increased for the remainder of the test.

The load response for the physical roller test increased rapidly within the first 1 mm of deformation and reached a peak load of 14.2 kN, then gradually decreased to 3.2 kN within 13 mm of displacement. As the upper section of the middle cell was compressed to allow the roller to contact the side surfaces of the center cell (Figure 38), the load experienced a secondary increase, which was observed to occur at approximately 15 mm displacement. The load increased as the roller compressed the lower section of the structure for the remainder of the test.

As shown in Figures 35 and 36, the similarity between load responses in their respective tests suggest that the deformation mode predicted by the numerical model is a very good representation of the physical apparatus and the testing condition it was subjected to. The FEA results revealed a slight overestimation in the load response for both tests compared to the physical test results. A potential cause for the variation could include both the setup of the test and inconsistent material properties of the specimen. A minor but notable movement of the platen was observed and may have contributed to the decreased loads observed in the physical test. While tensile tests were performed to obtain the stress-strain relationship for the material model of the simulation, the results of the tensile tests displayed variation between specimens and the average was used to obtain the stress-strain relationship. Any potential difference between the experimental stress/strain behavior, from the specimen tested, and the average value used would result in variations in the load predicted from FE simulations to the experimental observations. The accumulated error, presented as the relative difference in Equation 6, and validation metric represented as V in Equation 8 [33] were utilized to evaluate the accuracy of the simulation results. While Equation 6 was previously utilized to estimate the relative difference between contact forces, the formula can also be applied to calculate accumulated error between FEA and physical test results. Since the force responses obtained from both the physical test and the FEA were discrete data, Equations 7 and 9 were used for the discrete data to compute the cummulative error and validation metric, respectively.

$$V = 1 - \frac{1}{S}\int_0^S tanh\left|\frac{y(x)-Y(x)}{Y(x)}\right| dx \tag{8}$$

$$V = 1 - \frac{1}{L}\sum_{n=1}^{n=L} tanh\left|\frac{y(x_n)-Y(x_n)}{Y(x_n)}\right| \tag{9}$$

This validation metric was used to compute the accumulated error between the FEA and physical tests to evalute the disparity between them, with a scale from 0 to 1. The validation metric for the flat platen and roller compression tests was 0.74 and 0.73, respectively. The average difference between the load responses in the physical test and the FEA result were also calculated to be 28% and 27.7% for the flat platen and roller compression tests, respectively. With validation metrics above 0.7 and cummulative errors less than 30%, considering these error metrics are evaluated and integrated over the entire displacement domain, the FEMs were accepted as reasonably accurate estimates to the physical behavior of the energy dissipater.

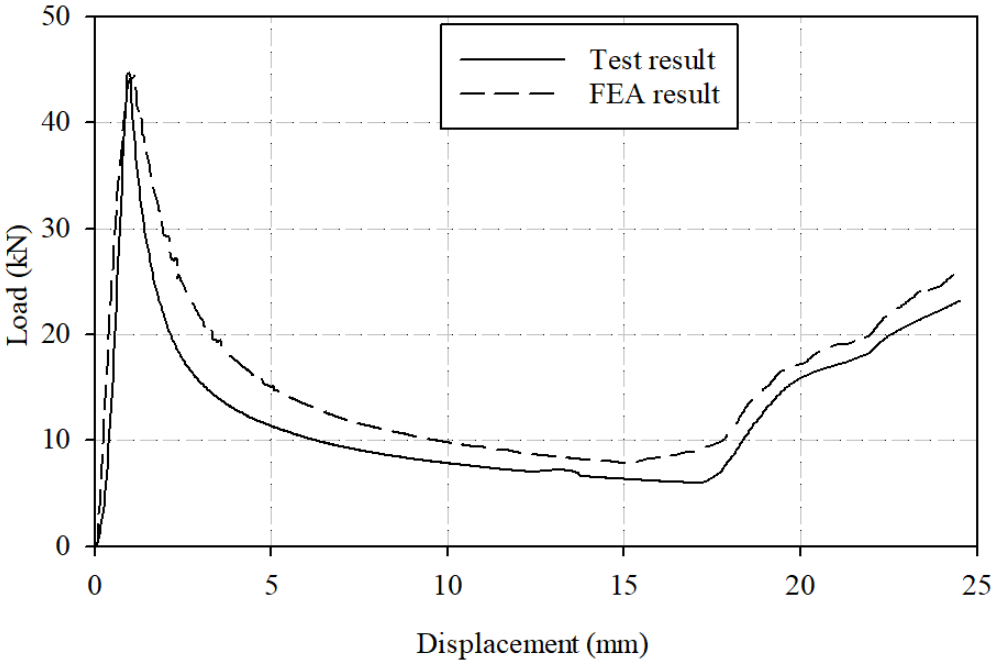

Figure 35. Load to displacement response of flat platform compression test.

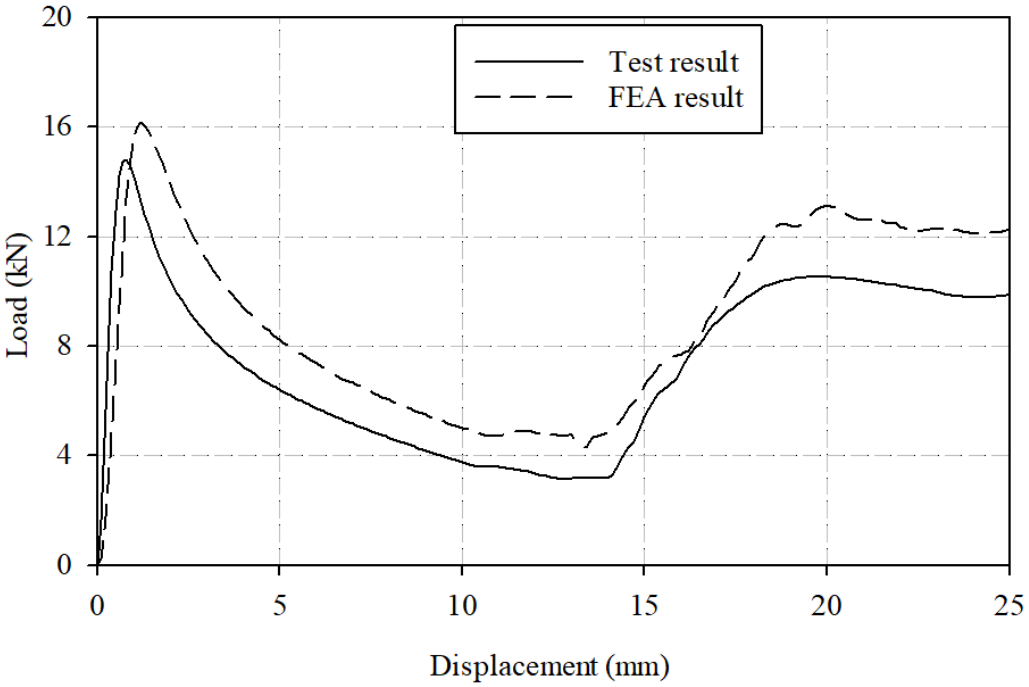

Figure 36. Load to displacement response of roller compression test.

Figure 37. Deformed specimen at 17 mm of flat platter compression.

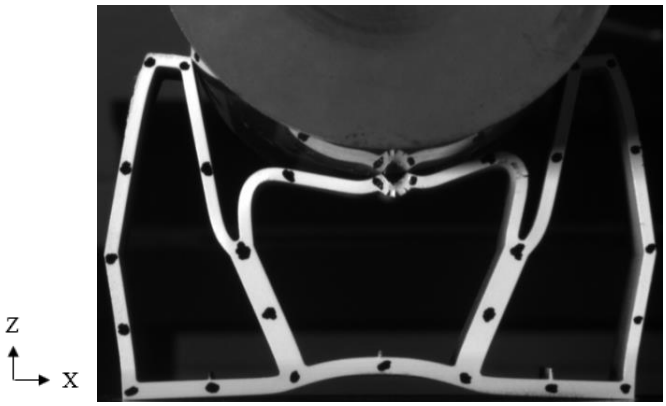

Figure 38. Deformed specimen at 14 mm of roller compression.

7. PARAMETRIC STUDY

7.1. Concept and methodology

To investigate the behavior of the revised design, a series of parametric studies were performed to determine the significance of each dimension. The critical dimensions of a single cell are marked in Figure 39(a). From the load path shown in Figure 39(b), both the force applied to the upper section of the structure and the lateral force acting on the lower section of the structure were affected by the angle "Alpha" shown in Figure 39(a). In its undeformed state, the forces acting in the system are shown in Figure 39(b). The relation between the force applied (F) acting at top of a single cell to the force acting along the wall in the upper section (F_{upper}) and the lateral force ($F_{lateral}$) could potentially be described by a trigonometric relation as presented Equations 10 and 11. Therefore, modifying "Alpha" could alter the force within the structure which may change the deformation mode. The benefits of the parametric studies were to determine: the effect of adjusting the proportion of upper and lower section of the structure; the effect of adjusting the ratio of wall thickness of the upper and lower sections; and the effect of changing angle "Alpha" on the deformation mode. Based on the benefits of the parametric study, dimensions "B", "F", and "E" were adjusted in small increments so as to thoroughly assess the influence of each value on the performance of the structure.

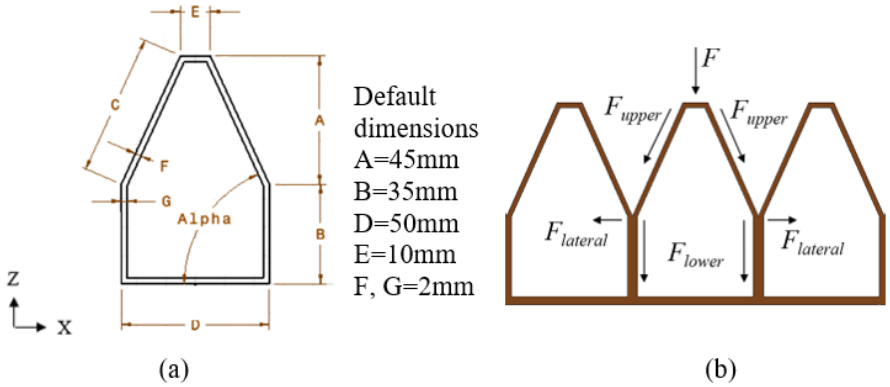

Figure 39. (a) Critical dimensions and (b) load configuration of the unit cell.

$$F_{upper} = \frac{0.5F}{\sin(Alpha)} \tag{10}$$

$$F_{lateral} = \frac{0.5F}{\tan(Alpha)} \tag{11}$$

7.2. Finite element model

Since the model was verified and validated as an acceptable representation of the physical test, with details provided in Section 6, the modeling technique was used to generate the finite element model for a detailed investigation of the self-adaptive energy dissipater. The dissipater was modelled with similar element characteristics as the validated model, as shown in Figure 40(a). The structure was divided into 4 layers and shifted by 12.5 mm between each layer for consistency of the structure as in Figure 40(b), note that the 4 layers were modeled as a single part; color was added for the purpose to distinguishing between the layers of the structure. The offset distance of second, third and fourth layer reference to the first layer was +12.5 mm, -12.5 mm and +25.0 mm in the x-direction, respectively. This offset pattern was to prevent the legform impactor from experiencing torsional load or bending moment about z-axis. The model of legform impactor and

pendulum impactor was modeled with proper size as described in the project requirement in Section 4.1. Each lateral free end surface of the structure in the x-direction was constrained to only allow translation in the y- and z-directions to represent a symmetric boundary condition. The lower surface of the dissipater was fully constrained from motion.

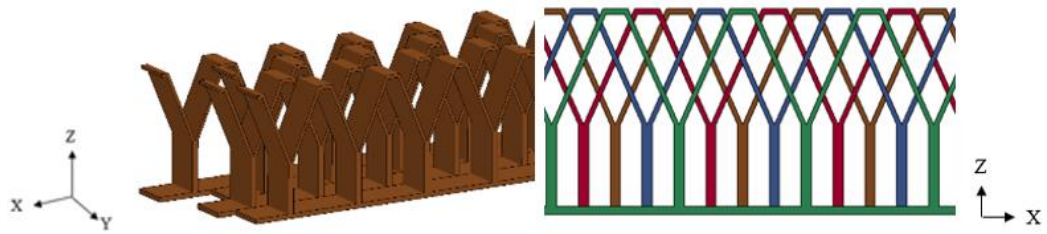

Figure 40. Finite element model of revised structure: (a) section of structure with symmetrical cut-off and (b) layers of structure differed with color.

The material data provided by the industrial partner was used for further investigation. However, slight modifications were implemented based upon previous observations. Due to the large-scale deformations of the structure toward the end of the test, elements were deleted when the strain of the element exceeded a specified failure value, which was 0.8. After discussion with the industrial experts, it was recommended that the strain to failure property should be excluded from the material card. FEA was conducted on an identical model, with the only difference being the presence of the strain to failure property. The load/displacement response of the test was as shown in Figure 41. The load was nearly identical within the first 10 mm of deformation. After the first 10 mm of deformation, the fluctuating load response of the tests showed small variations with a similar load trend. The maximum difference in load was 1 kN; the average load of the tests with and without the failure property was 2.73 kN and 2.80 kN. The relative difference between the tests calculated with Equation 7 was 9%. Since the difference between test

results was not significant, it was therefore acceptable for the strain to failure property to be removed.

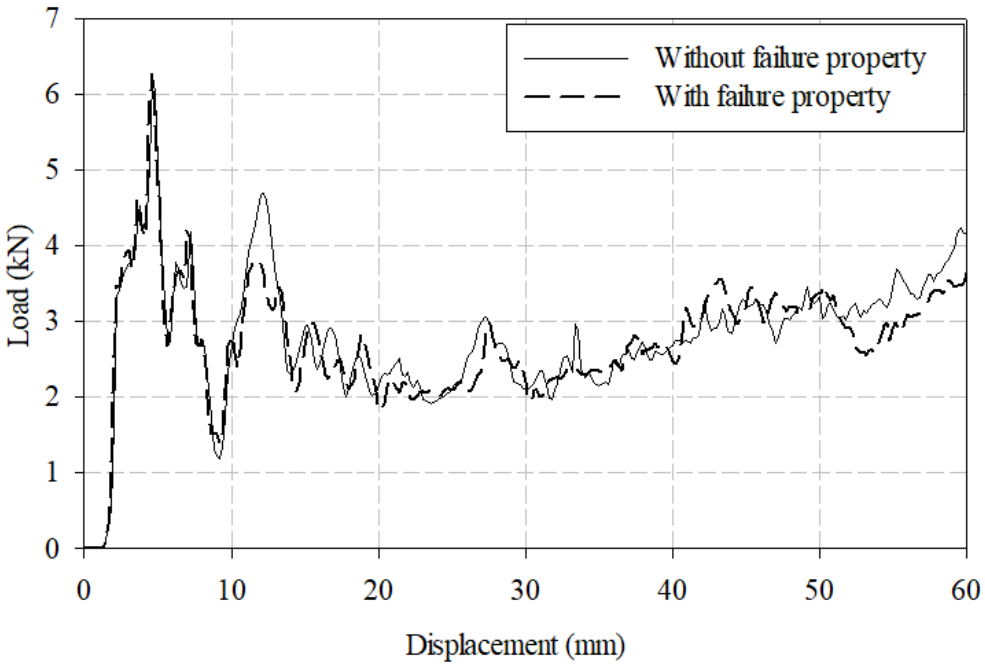

Figure 41. Result of material with and without failure property

7.3. Deformation and loading behavior of structure with default dimension

The load/displacement response of the energy dissipating structure with the default dimensions was obtained and is presented in Figure 42. The geometry was revised by replacing the rounded top with a flat surface to shift the peak load observed in the pendulum test as outlined in Section 5.3.4. The peak load observed in the pendulum test was shifted to the initial 5 mm of the deformation process due to this revision. Given the numerical predictions of the load/displacement response in the legform and pendulum tests (Figure 42), the deformation was observed to occur in three stages.

In the legform test, the first stage was identified as the initial impact and the deformation of the structure between 0 mm and 10 mm of impactor displacement. The load

rapidly increased as the impactor engaged with the energy dissipating structure (Figure 43(a)) and reached a load of 2 kN over 2 mm of displacement, a fluctuating load between 2 kN to 2.8 kN was observed within the next 5 mm of displacement, then decreased below 40% of the peak load in the following 3 mm of displacement. The second stage was characterized by the deformation of the upper section of the structure which occurred between 10 mm to 40 mm of impactor displacement, as shown in Figure 43(b). The structure was observed to be weaker in the upper section since the load/displacement responses during the second stage displayed an average load that was approximately 30% of the magnitude of the peak load in the first stage. The third stage initiated after 40 mm of impactor displacement; beyond this displacement the upper section of the dissipater was fully crushed, and the lower section experienced large scale deformation (Figure 43(c)). During the third stage, since the impactor was constrained to produce a centric loading condition on the lower section of the structure, the load responses experienced a secondary increase and reached a local peak load of 3.3 kN at approximately 47 mm of deformation. The load was reduced to 2.8 kN at 50 mm of deformation and maintained an average load of 3 kN for an additional 5 mm of displacement, followed by a decrease to 2.5 kN in the last 5 mm of displacement of the simulation. While this configuration would most likely occur infrequently when the impact location is not carefully controlled, it demonstrates the maximum possible load response when the structure is impacted. To ensure a conservative and robust design was produced, this critical loading setup for the legform test was selected for further study.

The deformation of the energy dissipater observed during the pendulum test was also divided into three stages. The first stage contained the global maximum load of

39.5 kN; however, an increase and decrease of the reaction load occurred rapidly within the initial 5 mm of deformation. The load response was high in first stage since the undeformed structure (Figure 44(a)) possessed an artificially increased stiffness since multiple cells were loaded. The second stage was characterized by an average load of 8 kN between 5 mm to 40 mm of impactor displacement when the upper section of the structure was deformed. This was significantly reduced compared to the loads predicted in first stage after the rigidity of the undeformed structure was lost (Figure 44(b)). The third stage was initiated when the upper section of the structure was completely deformed, just above 40 mm of impactor displacement (Figure 44(c)) and followed by a secondary increase in load. The load in the third stage increased continuously as the structure was compacted and a secondary peak load of 17 kN was observed at the end of the simulation; the total energy absorption in the pendulum test was 504 J. Figures 43 and 44 only illustrate the deformation of one layer of the energy dissipating structure; the hidden layers display an identical deformation mode.

The upper section of the structure was less resistant to deformation than the lower section since the wall thickness was reduced and the angle “alpha” increased the load applied in the direction of the upper wall. The emphasis of the parametric study was to observe the deformation modes and resultant load/displacement response when critical design parameters were adjusted.

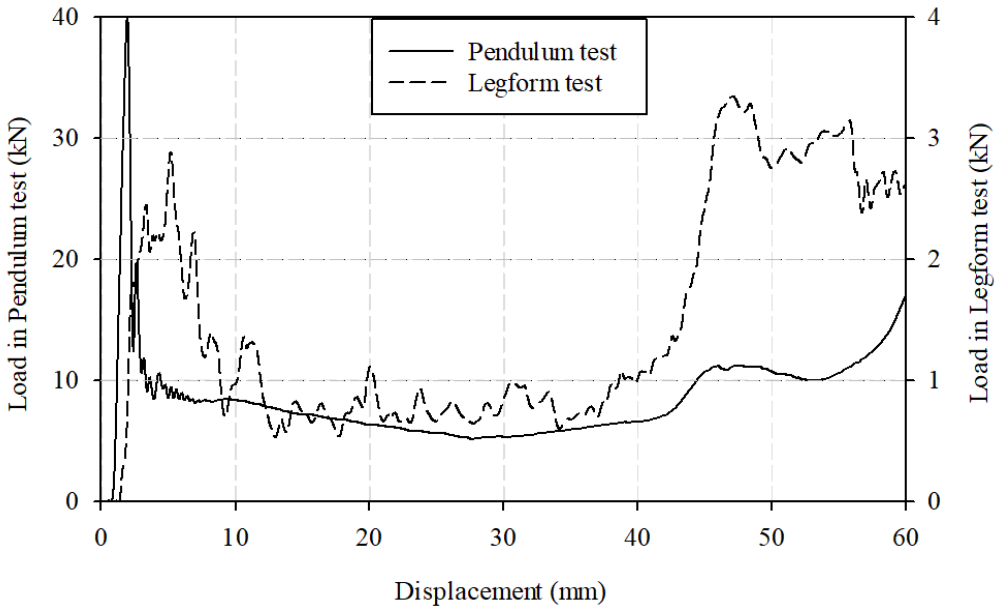

Figure 42. Load versus displacement of the energy dissipating structure with default dimensions.

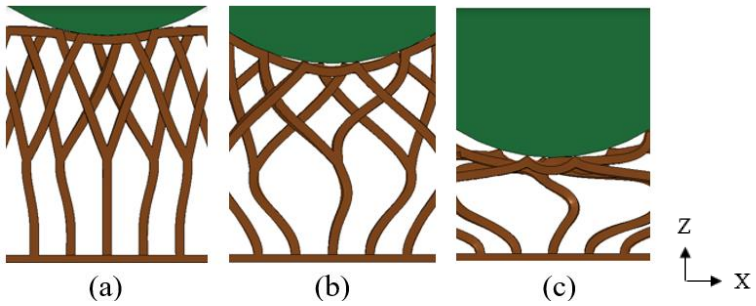

Figure 43. Legform test deformation: (a) observed during the first stage of deformation at 5 mm, (b) observed during the second stage at 15 mm, and (c) observed during the third stage at 45 mm.

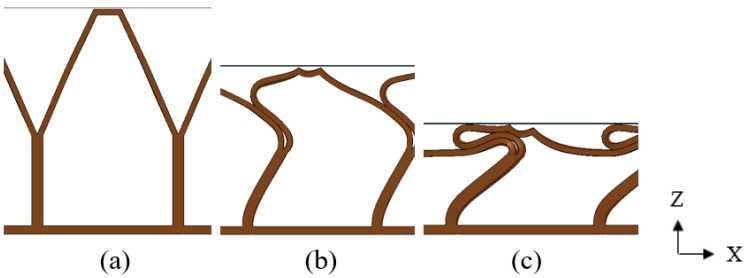

Figure 44. Pendulum test deformation: (a) observed during the first stage of deformation at 3 mm, (b) observed during the second stage at 16 mm and (c) observed during the third stage at 45 mm.

7.4. Influence of altering dimension “B”

Dimension “B” influenced both the upper and lower sections of the energy dissipater. When dimension “B” was increased from the default value, the upper section of the structure reduced in height which correspondingly reduced “alpha” and the length of the sidewall of the upper section. The lower section of the structure also increased in height since the overall height remained constant. The change in angle “alpha” was expected to have a proportionate effect on the force applied through the wall in the upper section, therefore, further tailoring the load/displacement response. The revised geometry in the lower section was expected to alter the transition from the second stage to the third stage in the legform simulation. The load/displacement responses of the tests with various values of dimension “B” are shown in the appendix, Figure A1 and A2 for the legform and pendulum tests, respectively.

The load/displacement responses for the legform simulations revealed that when “B” was increased from 35 mm to 50 mm, the initial peak load reduced from 2.9 kN to 1.8 kN. This reduction in load was attributed to the reduction of “alpha”, which decreased the force necessary in the z-direction to cause a similar force in the x-direction to deform the lower sections of the cells. The increased height of the lower section also reduced the resistance to buckling. The load response in the second stage remained unchanged until the transition to third stage. As expected, increasing “B” caused the third stage to initiate earlier in the deformation process, where the reduction in displacement was proportionate to the increase of “B”. Additionally, the load required to deform the lower section was increased in the final stage of the test. When “B” was reduced to 30 mm, in addition to the increased

load observed in the first stage, the load response in the third stage also increased significantly, which is an undesired effect.

When “B” was increased for the pendulum test, the results displayed a minor reduction in the load response during the first stage due to the adjustment of “alpha”. The second stage reduced in the displacement domain as “B” was increased; additionally, a secondary peak load initiated near the transition region between the second and third stages. Increasing “B” caused the upper section of the structure to reduce in overall size and rigidity. When the upper section was completely deformed, the following deformation in the lower section was insignificant. As the lower section deformed, the structure (Figure 45) maintained a high stiffness compared to the structure with default geometry (Figure 44(c)). Therefore, the resultant load response of the secondary peak load increased when “B” was increased. Since the duration of the second stage of deformation reduced as “B” was increased, the secondary peak load also occurred with less deformation. The secondary peak load was approximately 35 kN at 29 mm of displacement when “B” was set to 50 mm. The formation of this secondary peak load increased the load response over a large span of deformation, resulting in a significant increase in total energy absorption. When “B” was reduced to 30 mm, a secondary peak load with similar magnitude was also formed, at approximately 55 mm of displacement, which is not as beneficial compared to “B” equal to 50 mm.

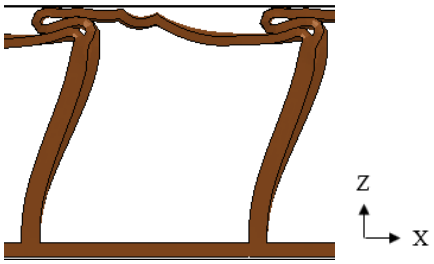

Figure 45. Pendulum test at 25 mm impactor displacement for “B=50mm”.

7.5. Influence of altering dimension “E”

The primary objective of studying dimension “E” was to understand the effect of indirectly adjusting “alpha” at the top section of the structure. Unlike an adjustment to dimension “B”, changing “E” will only influence the upper section of the structure and was expected to only affect the load response in the first and second stages. From Equations 3 and 4, it was expected that when “alpha” was reduced, the load required to initiate deformation would also decrease. The reduction in load was anticipated to affect both tests, with more pronounced effects in the first stage of the legform test. The load/displacement responses of the tests with various values of dimension “E” are shown in the appendix, Figure A3 and A4 for the legform and pendulum tests respectively.

The results of the parametric study of dimension “E” in the legform test were as expected in the first and second stages. When dimension “E” increased from 6.4 mm to 22 mm, the load response in the first stage of deformation increased from 2.4 kN to 3.7 kN. The load response in the second stage of the deformation also increased, however, the increase was only by an average of 0.1 kN. In the third stage of deformation, the load response increased with the decrease in dimension “E”. This change in load for the third stage was not expected since adjusting “E” did not affect the geometry in the lower section of the structure. A probable explanation could be that the deformation of the lower section

during the third stage was increased since less deformation occurred in previous stages due to the reduced load.

For the pendulum test, the results contradicted the previously discussed expectations. In the first stage of deformation. the load response was increased when “E” was decreased. By comparing the deformation modes between the models, larger deformation in the lower section was observed in the simulation with an increased “E” value (Figure 46). A reasonable explanation would be as “E” decreased, the complementary decrease in “alpha” induced greater lateral loads which increased the stability of the lower structure. Therefore, an increase in load was required to deform the structure compared to the default geometry.

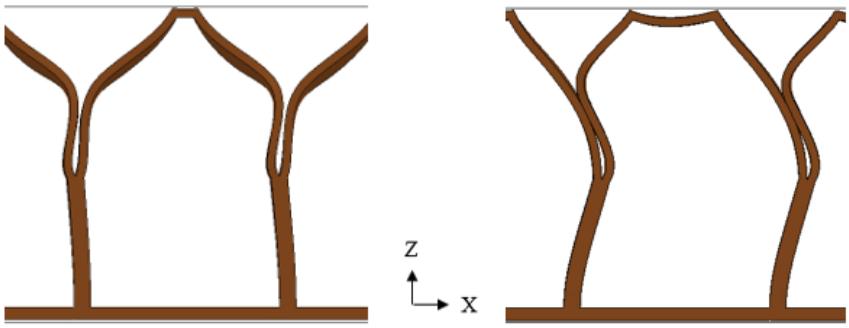

Figure 46. Pendulum test at 6 mm displacement with (a) E=6.4 mm and (b) E=22 mm.

7.6. Influence of altering dimension “F”

Dimension “F” represents the wall thickness of the upper section of the structure. With the default dimension, since the lower sections of each adjacent cell are connected, the lower section of the structure displayed increased strength compared to the upper section. The load response in the first and second stages for both tests were strongly correlated to the stiffness of the upper section of the structure. When the upper section was

stiffened by increasing dimension “F”, it was expected that the load responses during the first and second stages for both tests would increase. It was also expected that the load difference between the second and third stages for the legform test would decrease. The load/displacement responses of the tests with various values of dimension “F” are shown in the appendix, Figure A5 and A6 for the legform and pendulum tests respectively.

The results of the legform simulations demonstrated a significant increase in the reaction load during the first two stages when “F” was increased. With the increase in parameter “F”, the upper section responded in a stiffer fashion, causing the force required to initiate deformation to increase. The peak load in the first stage increased from 2.9 kN to 6.2 kN. The load response in the second stage also increased from an average of 0.8 kN to 2.9 kN. The increased stiffness in the upper section caused more load to be transferred to the lower section which caused significant deformation during the second stage. Therefore, the transition between the second stage and third stage became less significant as dimension “F” increased. With “F” increased to 4 mm, the average load in the second stage was similar to the third stage. Under this deformation mode, the load response was consistent regardless of where the impactor contacted the structure.

The results of the pendulum tests displayed a significant increase in energy absorption. When dimension “F” was increased to 4 mm, the peak load in the first stage increased from 40 kN to 79 kN, with the duration of the first stage increasing by a factor of 2. In the second stage, the average load increased by a factor of 3 compared to the results with the default dimension. In the final stage of the deformation, the increased stiffness and material in the upper section increased the load response when the structure was compacted. Note that if specific energy absorption is considered, the SEA dropped slightly

when “F” was increased from 3.5 mm to 4 mm (Table B5), which indicates that “F” induces the maximum specific energy absorption within this region. This specific dimension is also likely to cause the upper and lower sections of the structure to possess a similar structural stiffness.

7.7. Summary of parametric study

From the parametric study, the effects of controlling key dimensions in the structure were investigated. In the legform test, increasing dimension “B” caused a decreased load during the first stage, increased load in the third stage and increased the average load. Decreasing “E” reduced the load in the first stage and marginally increased the load in the third stage; the average load change was negligible. Increasing dimension “F” caused a significant load increase in the first and second stages as well as an increase in the average load. In the pendulum test, increasing “B” and “F” caused a large increase in energy absorption; decreasing “E” also caused an increase in energy absorption. However, the reduction was minor and occurred in the late stages of deformation. With consideration for the objectives of this study, the most crucial factor to consider when evaluating the legform test is the peak load throughout the test, with the average load as a secondary consideration. For the pendulum test, the most important factor was energy absorption, with the goal of obtaining high energy absorption in the early stages of deformation. A summary of these data is provided below, in Table 2, and Table B4 contains further details in Appendix B. Also, plots of the load/displacement response for the tests specified in table two are shown in Figure 47 and 48.

Table 2. Key parameters for evaluating result of test result.

Dimension (mm)	Load in legform test		Energy absorption in pendulum test		
	Peak load (kN)	Average load (kN)	At 10 mm (J)	At 30 mm (J)	At 60 mm (J)
Default (B=35, E=10, F=2.0)	3.3	1.5	105	234	504
B=50, E=10, F=2.0	4.9	1.85	121	447	963
B=35, ***E=6.4***, F=2.0	4.2	1.65	119	261	698
B=35, E=10, ***F=4.0***	6.2	2.8	368	749	1420

The altered dimension is highlighted with bold font.

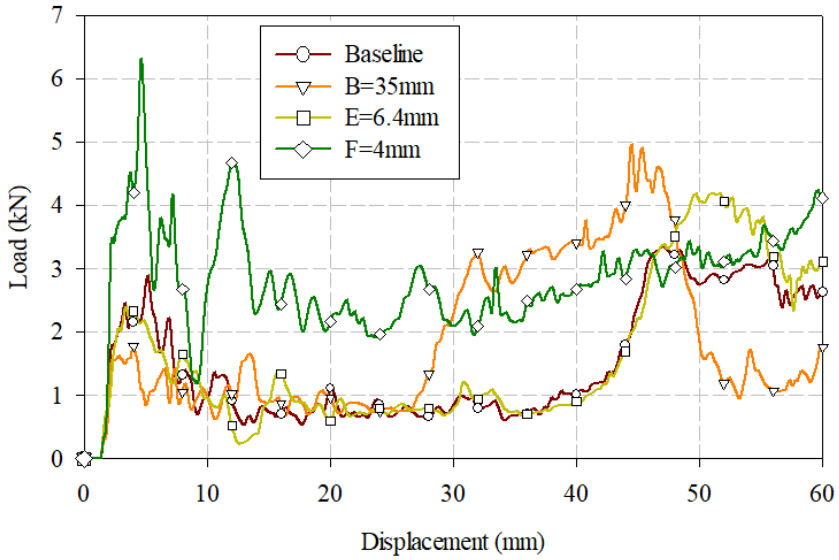

Figure 47. Legform test load/displacement response for tests in Table 2.

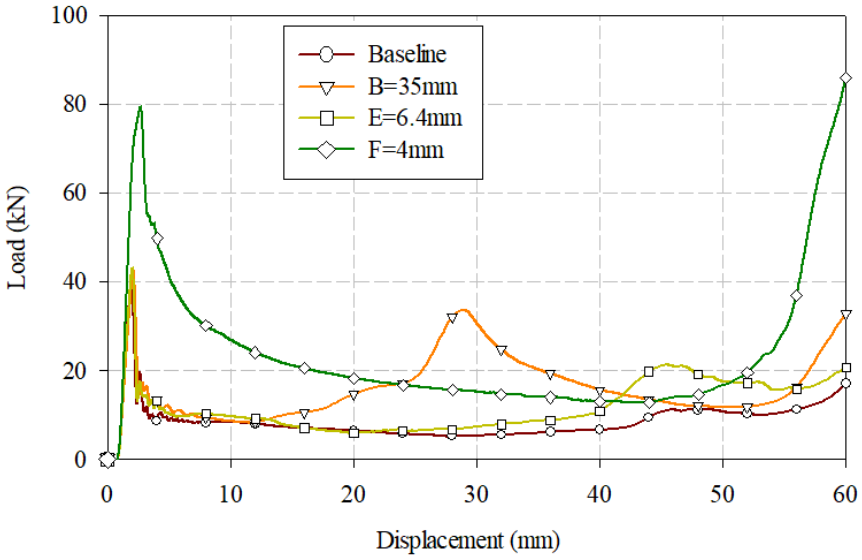

Figure 48. Pendulum test load/displacement response for tests in Table 2.

Adjusting dimensions “B” and “F” yielded a significant increase in energy absorption for the pendulum test. When “B” was increased to 50 mm, the increase in energy absorption caused by the secondary peak load occurred at approximately 30 mm of displacement, while the increase in energy absorption caused by the larger initial peak load when “F” was increased occurred within the first 10 mm of the pendulum test. When evaluating simulations which implemented changes to “B” and “F”, it was revealed that the increase in energy absorption caused by the changes of “B” and “F” for the pendulum test could not coexist. The increased energy absorption observed when increasing “B” occurred since the upper section was significantly weaker than the lower section; however, the purpose of increasing “F” was to increase the stiffness of the upper section. Comparing the results between adjusting “B” to 55 mm and “F” to 4 mm, the load in the legform test favors adjusting “B” in the simulation with 21% less peak load and 34% less average load (Table 2). The pendulum test results presented an advantage when adjusting “F” by displaying 47% more energy absorption, especially since a significant quantity of the increased energy absorption due to the dimension change occurred in the first 10 mm of deformation. Considering the test results presented above, adjusting “F” yielded more benefit within the scope of this research. Additionally, reducing dimension “E” reduced the peak load in the first stage for the legform tests; this was instrumental in reducing the peak load caused by increasing “F”.

Using the information obtained in the parametric study, the geometry of the structure was revised prior to the next objective of this investigation. With consideration of manufacturing the dissipater from a polymeric material, a suggested maximum material thickness of 3 mm was stipulated by the industrial partners. The structure was adjusted to

a 3 mm wall thickness in both the upper and lower sections. Dimension “E” was reduced to 7 mm to reduce the peak load in the legform test. Dimension “B” was unaltered, 35 mm was optimal for the structure to possess a similar stiffness in the upper and lower sections. Dimension “D” was also reduced to increase the number of cells to compensate for the reduced wall thickness. The results of the simulation with the revised structure included a peak load of 4.5 kN, an average load of 2.3 kN in the legform test and 1.26 kJ of energy absorption in the pendulum test.

8. GEOMETRIC MODIFICATIONS

8.1. Concept and methodology

The revised design employed a simplified geometry. Adding or removing material at critical locations allowed for the implementation of customized reinforcements and stress concentrators in the structure to tailor the deformation mode depending on the application. These adjustments included: weakening the bottom section by adding grooves to initiate bending at specific locations (Figure 49(a)), adding supports between adjacent cells in the upper section (Figure 49(b)), adding material to increase the initial contact area (Figure 49(c)) and support the bottom section of the structure (Figure 49(d)). The shaded area in the figures represents the added structure. Other structural modifications were investigated with no benefit to the performance, which will be discussed in later sections.

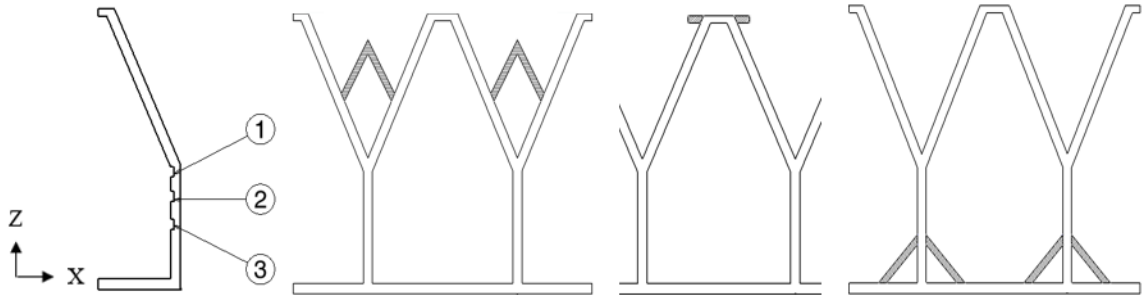

Figure 49. Structure Modification of: (a) Groove location, (b) Added structure in upper section, (c) Extended initial contact surface and (d) Added support in lower section.

8.2. Influence of groove design

Removing material from the structure allowed for control over the initiation point of the deformation. There were two objectives associated with the implementation of grooves. The first objective was to reduce the load response in the legform test by introducing a groove at the location of bending initiation and the second objective was to

modify the deformation mode by causing additional bending to occur in the pendulum test. To accomplish these objectives, grooves were added to the lower section of the dissipater (Figure 49(a)). A single groove was added to the dissipater with the location varying over multiple simulations. Groove location 1 coincided with the location where bending initiated in the unmodified legform simulation; the location was 35 mm from the lower surface of the dissipater. Groove locations 2 and 3 were 28 mm and 20 mm from the bottom of the structure, respectively. The load/displacement responses of the tests with grooves at specified locations are shown in the appendix, Figure A7 and A8 for the legform and pendulum tests respectively.

In the legform test, the load response was reduced for groove location 1 compared to the unmodified results. The peak load in the first stage of deformation and average load throughout the test were reduced by approximately 10%. The reduced material at the groove location acted as a stress concentrator and initiated deformation prematurely compared to the default geometry. For the simulations with a groove at locations 2 and 3, no significant improvements were observed.

In the pendulum test, the total energy absorption with a groove at location 1 increased by 15.5%. In contrast, groove locations 2 and 3 provided no benefit. The load response for the simulation with groove location 1 was similar to the unmodified simulation prior to 30 mm of deformation as the lower section of the structure was deformed. During the second half of the test, between 30 mm and 55 mm, the upper section of the structure in the tests with grooves added to the dissipater was in a stiffer orientation which increased the load response (Figure 50). The total energy absorption increased by 100 J by introducing a groove at location 1.

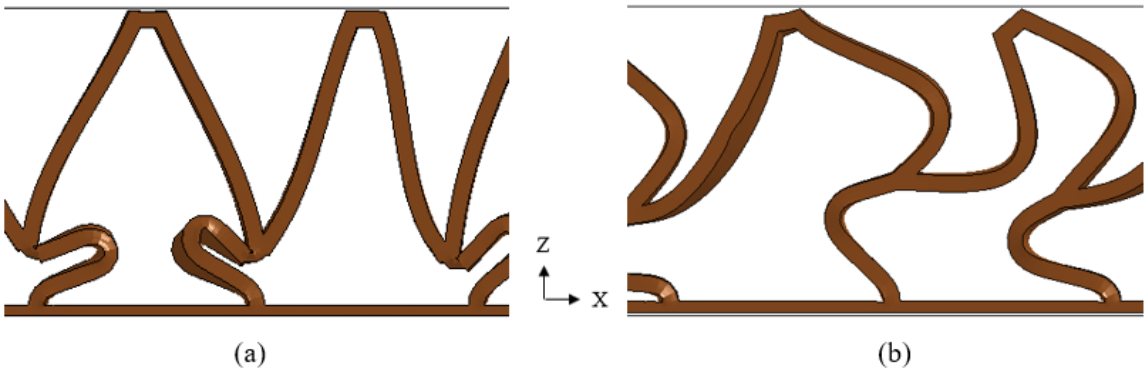

Figure 50. Structure at 25 mm of impactor displacement (a) with groove and (b) without groove.

8.3. Influence of added structure between upper trapezoidal section

From the observations of previous tests, the "V" shape formed by the upper section of adjacent cells experienced minor deformation during the first stage of both tests. Therefore, structure was added between the upper trapezoidal sections of adjacent cells as shown in Figure 49(b). This was expected to influence the load response in the early stages of deformation. The intention was to increase the reaction load in later stages of both tests without affecting the load response during the first stage of deformation. The added structure is shown as the shaded area in Figure 51. The geometry of the added material was determined by the thickness of the wall, the height where the added structure connected with the main body and the angle of the added structure. These dimensions are referred to as dimensions "H", "I", and "Beta", respectively, as shown in Figure 51. In general, increasing "H" caused the load to increase throughout both tests; decreasing angle "Beta" caused the load to increase in the later stage of both tests with more influence in the pendulum test results and altering dimension "H" influenced the rate of load increase in the second stage of the legform test. The results discussed below are based upon the structure with dimensions as specified in Figure 51. The load/displacement responses of

the test with the added support in upper section are shown in the appendix, Figure A9 and A10 for the legform and pendulum tests, respectively.

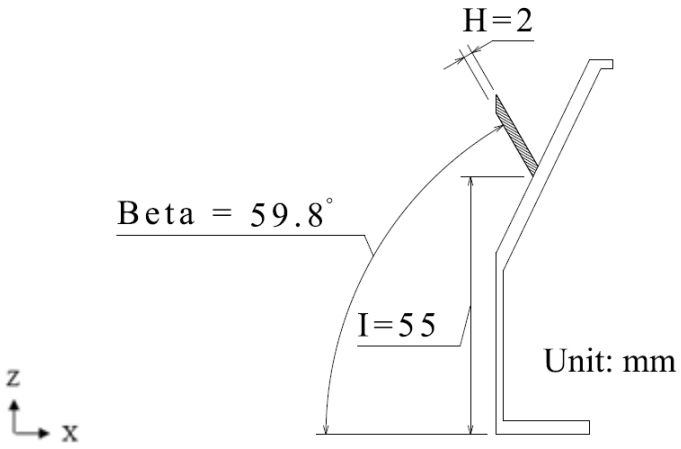

Figure 51. Dimension callout for added material in the upper section.

In the legform simulation results, the average load response in the second and third stages of deformation increased significantly while the initial peak load experienced a minor increase from 4.5 kN to 5 kN. After the peak load in the first stage decreased similar to the unmodified simulation, the load gradually experienced a secondary increase. The rate of increase in load response was controllable by modifying the geometry of the added material. The peak load was maintained under 5 kN up to 55 mm of displacement and reached 5.8 kN at the end of the test. The average load for the legform test was increased by approximately 50%.

With reinforcement from the added material, the upper section experienced an increase in stiffness. During the test, due to the increase of stiffness in the upper section, the deformation of the lower section transitioned to the second stage between 10 mm to 27 mm of displacement. Throughout the deformation of the upper section, which transitioned to the third stage of deformation, the load response significantly increased. No

change in the load response was observed during the first stage of deformation for the pendulum test. The load response for the test with added material was approximately 5 kN higher from 10 mm to 27 mm and 20 kN higher beyond 27 mm for the remainder of the simulation. Most improvements to the energy absorption capabilities of the dissipater occurred in the second half of the test (above 25 mm of displacement). The total energy absorption increased by 20% prior to 30 mm of displacement; the total energy of the entire pendulum test was increased by 75%.

8.4. Influence of extended upper surface

By observing the pendulum test simulations from the modification of dimension "E" in the parametric study, it was noted that when parameter "E" was decreased, the reduced contact area between the upper surface of the dissipater and pendulum impactor allowed the upper section to rotate freely. It was hypothesized that this uncontrolled rotation in the upper section could potentially reduce the bending of the structure throughout the test. Material was added to extend the upper surface, as shown in Figure 49(c), to prevent the upper section from rotating without increasing dimension "E". The motivation for this geometric revision was to produce a change in deformation modes which did not include the undesired rotation in the pendulum test without influencing the legform test, if possible. The upper surface length was increased from 7 mm to 15 mm with the added material for the test; the results in Figure A11 and A12 were generated.

In the legform test, the overall influence of the change in geometry was not beneficial. During the initial stage of deformation, the peak load increased from 4.5 kN to 5.0 kN. During the second and third stages, the amplitude of the load fluctuation was reduced, with the average load remaining unchanged.

The deformation mode of the pendulum test was altered since the rotation of the upper section was reduced, as shown in Figure 52. The lower section and wall structure near the upper contact area experienced additional deformation. However, the reflection of load response to the change in deformation mode was insignificant. Comparing the results of the extended upper surface to the previous test; the load response during first stage was not affected. Between 5 mm to 30 mm, the average load increased by approximately 1 kN; between 30 to 50 mm, the average load was decreased by 2 kN; and the average load was increased by 9 kN after between 50 mm and the end of deformation. The total energy absorption increased by approximately 5%.

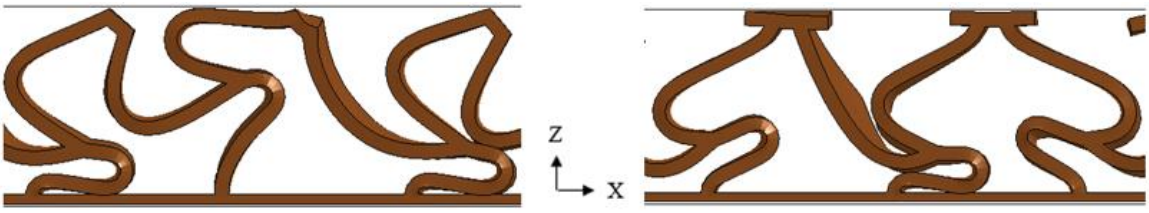

Figure 52. Pendulum test deformation mode (a) without extended top, and (b) with extended top.

8.5. Influence of support structure for lower section

During the first stage of the tests, the geometry near the lower surface had a minor influence on the load/displacement response. Therefore, adding material to the lower section as shown in Figure 49(d) was expected to increase the load response in the second and third stages without influencing the performance during the first stage of deformation. This modification was included in an effort to maximize total energy absorption under large-scale deformations. Various geometries of the support structure were tested, and the most preferable result was obtained by adding simple diagonal supports, as shown in

Figure 49(d). The increase in height where the structure was supported caused load response to increase for both tests, with greater effects observed for the pendulum test. However, if the height was raised above 20 mm, significant load increase would initiate towards the end of legform test as the impactor made direct contact with the supported section. Increasing the thickness of the supporting structure caused the load to increase in the later stages of both tests up to a certain limit. After the limit thickness was reached, further increase in the thickness did not increase the load response. The maximum thickness for a load increase effect varies with the length of the oblique support structure. The test results shown in Figure A13 and A14 were obtained for a main structure which was supported with a 45-degree oblique wall, at 15 mm from the bottom surface, while the thickness of the support was 2 mm.

The load response in the first stage of the legform test showed a 0.3 kN increase in the peak load compared to the unmodified structure. In the second and third stages, as the lower structure deformed, the load response increased by approximately 50%. The support section remained stiff and deformation was minimal, while the deformation was compensated for by the unsupported structure.

A comparison of the pendulum test results revealed an elevated load response. The load response during the deformation prior to 50 mm of deformation increased by an average of 5.5 kN with the implementation of the support. In the final stages of the simulation, the load required to deform the supported structure increased rapidly with a maximum load of 160 kN at 60 mm. For the dissipater which included the lower support, the energy absorption was increased by 27% throughout the deformation prior to 30 mm of displacement, and the total energy absorption of the test increased by 53%.

8.6. Other geometric modifications investigated

Structures depicted in Figure 53 were also tested, with support material added at the inner corners of the upper and middle sections of the cells.

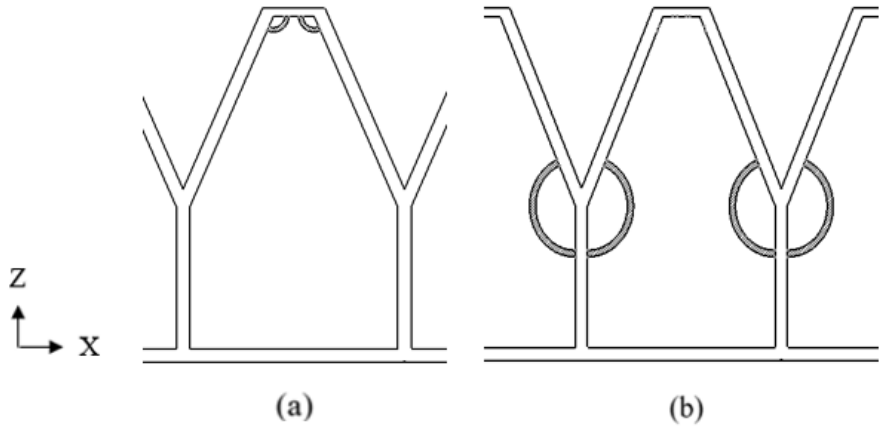

Figure 53. Reinforced structure at (a) upper and (b) middle corner.

Both designs resulted in an increase of load greater than 25% in the first stage of the legform impact test. The reinforcement structure affected the region where deformation initiated which resisted the deformation and increased the load bearing capacity. The change in energy absorption in the pendulum test was not significant to the extent where the sacrifice of performance in the legform test could be justified.

For the reinforced upper corner, Figure 53(a), although the result was not beneficial, the deformation result was informative. The added structure was effective in controlling the deformation mode, where the change of angle for the upper corner was resisted. It could be beneficial if the resistance only appeared when the angle of the corner was attempting to decrease, and not resisting the corner expansion. In the legform test, if the added structure does not resist corner expansion, the load in first the stage will not be affected. In the pendulum test, if the decrease in corner angle was resisted, it is likely that both upper

angles would expand and form a secondary, high stiffness structure as shown in Figure 20(a) in Section 5.3.3 to incur a complementary secondary peak load. This concept may be achieved by disconnecting one end of the reinforced structure while not removing material from it, in which the reinforced structure will only resist the collapsing of the corner. The wall thickness of the upper section may also need to be reduced slightly to initiate the deformation in the upper section for the pendulum test. This modification could be implemented by disconnecting the element in FEA, however, such a case is impractical from a manufacturing perspective. This mechanism will be discussed in the recommendations for future work that may be suitable for this concept.

8.7. Summary of designs with modified geometry

The modifications described in the previous sections allow for more control over the mechanical response of the system during an impact. More specifically, adding grooves to the lower section of the cells was shown to reduce the peak loads experienced in the legform tests without compromising the energy dissipation capabilities in the pendulum tests. Adding material between adjacent cells in the upper section increased energy absorption in the pendulum test with a minor increase of peak load for the legform test. Supporting the structure at the lower section also increased energy absorption for the pendulum test with a marginal increase in the maximum load for the legform test with a different behavior in the second stage of deformation compared to the original dissipater. The extended upper surface did not provide sufficient improvements to the mechanical response in the pendulum test to justify the reduced performance in the legform test. These results have been quantified and summarized below in Table 3 in addition to the details provided in previous sections.

In this study, the required performance of the structure was to absorb 1 kJ of energy, equivalent to the energy of a small car travelling at 4 km/h with as little permanent deformation as possible. Additionally, the peak load response for the legform could not exceed 6 kN, with the majority of the deformation process kept below 5 kN. The average load observed in the legform test and energy dissipation for the pendulum test were also considered to evaluate the outcome. These key parameters are included in Table 3 below. Table B5 is available in Appendix B with extended details. Figure 54 and 55 below shows the load/displacement responds for tests in Table 3, the result of extended top surface is not shown in the figure since it has very similar result to the unmodified structure.

Table 3. Key parameters for evaluating result of test result.

Geometric feature	Load in legform test (kN)		Energy absorption in pendulum test (J)		Displacement required for 1 kJ of energy absorption (mm)
	Maximum	Average	At 30 mm	At 55 mm	
Unmodified	4.5	2.3	507	1100	53
Groove	4.1	2.0	532	1270	50
Added structure in upper section	5.8	3.3	613	1920	42
Extended top surface	5.1	2.3	543	1120	53
Support structure in lower section	4.7	2.7	644	1510	47

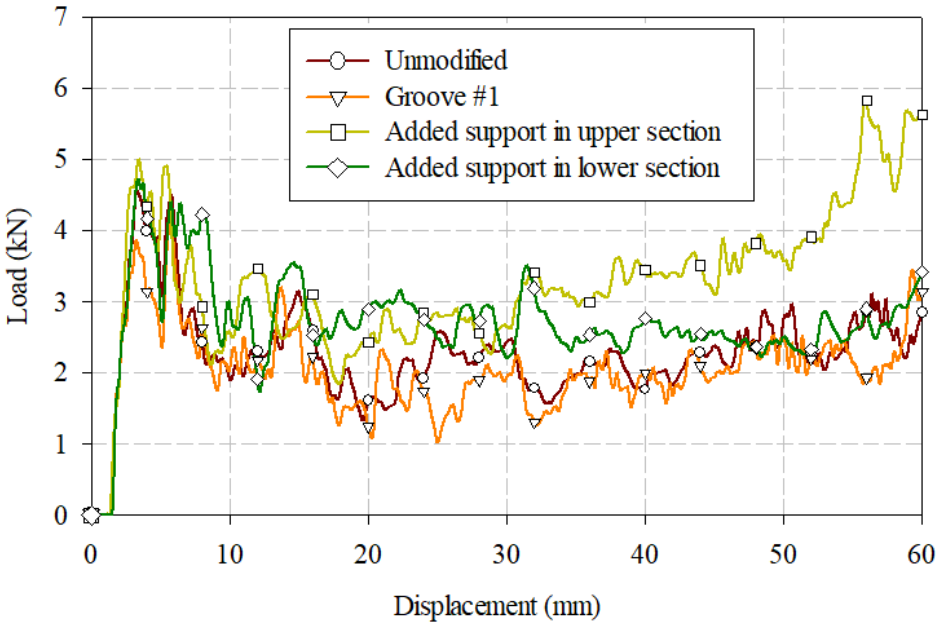

Figure 54. Legform test load/displacement response for tests in Table 3.

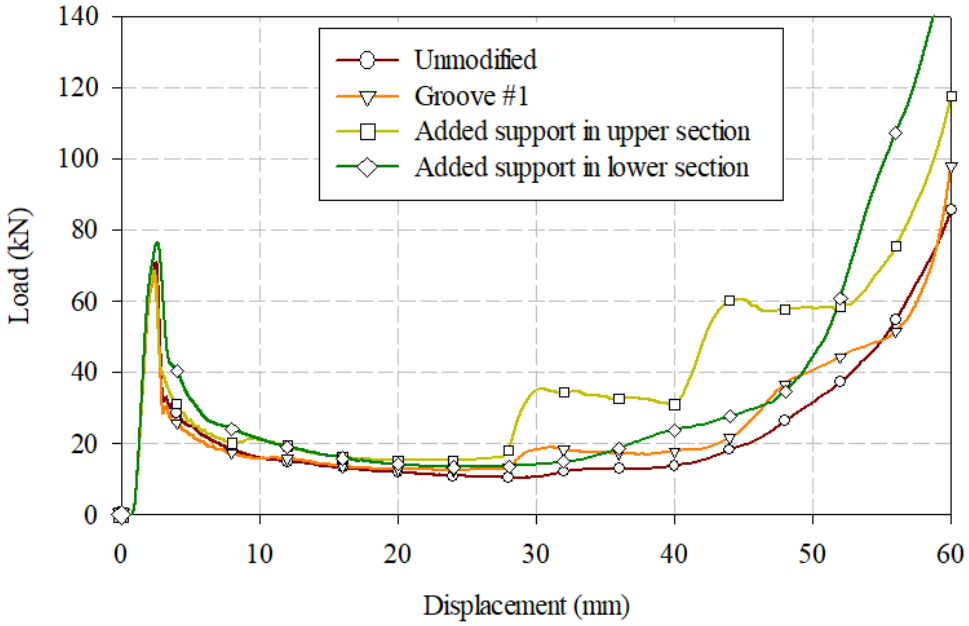

Figure 55. Pendulum test load/displacement response for tests in Table 3.

Material added to the upper and lower sections increased the energy absorption significantly in the pendulum test. Furthermore, the dissipater with added material in the upper section displayed the most ideal results which satisfied the energy absorption

requirements within 42 mm of deformation for the pendulum test. However, the dissipater with the support structure in the lower section displayed preferable legform test results. In addition to the reduced peak and average load response, the load response beyond the first stage of deformation was consistent with the results for the support in the lower section. While the dissipater with added material in the upper section satisfied the requirements for the legform test, a consistent load is preferable compared to the occurrence of a secondary peak load. The simulation with an added groove at location 1 demonstrated improvements by reducing the overall load response in the legform test and increasing total energy absorption in the pendulum test. The groove design provided a universal improvement that should be implemented in combination with other designs.

With the knowledge obtained from the parametric study and geometric modifications, the most preferred structure would include the following features:

1. The upper trapezoidal and lower rectangular sections of the structure should be designed to have similar load bearing capacity in the pendulum test, both sections should deform simultaneously to increase energy absorption in the early stage of the test. This could be accomplished by altering the wall thickness, where a uniform wall thickness would be preferred.
2. The dimension “B” indicated in geometric study should be low to reduce the initial peak load in the legform test. However, the upper section should not be designed with a triangle shape to prevent highly concentrated load.
3. A stress concentrator, such as a designed groove, located at the transition between the upper and lower sections could reduce the initial load in the legform test without reducing the performance in the pendulum test.

4. Triangular supports at the bottom of the structure should be utilized to increase the energy absorption in the pendulum test.

9. CONCLUSIONS

The previously outlined objectives of this investigation were satisfied by assessing, through numerical studies, a series of pilot designs; the most favorable design included a rectangular array of trapezoidal cells which artificially increased the stiffness of the structure with increasing loaded contact area. The simulation efforts of this study were validated with physical testing of a scaled-down reproduction of the geometry from a steel alloy. This was done to ensure that the generated models produced high quality predictions, assuming a reasonably accurate material model is implemented. All finite element models were also verified by assessing the energy balance and average energy ratio. Further parametric and geometric studies were also conducted to assess the influence of geometric modifiers including stress concentrators and the significance and influence of each critical dimension, respectively. The key findings of this study were as follows:

1. A preferable passive energy dissipater was determined to consist of adjacent, constrained cells with individual contact surfaces to allow for buckling in single-cell impacts and an artificially stiffened structure which maximized initial energy absorption under multiple-cell impacts. These characteristics were identified within the preliminary study where round top cellular structure exhibited a peak load of 32.0 kN at 17.0 mm of displacement compared to 23.0 kN at 32.0 mm and 10.8 kN at 26.4 mm for hemispherical structure and lateral ring structure, respectively in the pendulum tests.
2. A modified version of design 3 was developed which maintained the trapezoidal cells with modified flat impact surfaces. The following parametric study revealed that the ratio between dimensions “F” and “G” was the most critical parameter to

control. A 2:1 ratio between “F” and “G” is ideal to maximize total energy absorption for the pendulum test while maintaining a consistent load/displacement response for the legform. Additionally, such design implementations demonstrated the ability to control the initiation of failure by modifying the wall thicknesses in the upper and lower sections.

3. The pendulum and legform tests possess unique deformation modes; plastic hinge formation initiated at different locations for each respective test. Reducing the wall thickness at the hinge initiation location, groove location 1, reduced the initial peak load by 10% for the legform test and 5% for the pendulum test compared to the unmodified geometry.
4. Material was added to the junctions in the form of thin-walled crossbars between adjacent cells since this region experienced minor deformation during the initial stage of testing. The upper and lower supports increased the average load beyond the first stage of deformation by 39.1% and 17.4%, respectively, without significantly altering the peak loads observed in the first stage of the legform test. In the pendulum test, the upper and lower supports increased the total energy absorption by 74.5% and 37.3%, respectively. Based on these data and the analysis provided in previous sections, it was determined that implementing the lower support was preferable compared to the upper support.

10. RECOMMENDATIONS FOR FUTURE WORK

By observing the deformation and load/displacement response behavior of the FE models performed throughout this research study, knowledge of repeated, cellular self-adaptive energy absorbing structures was obtained. Based upon the knowledge and findings, the following recommendations are provided for future investigations into this topic with the potential to improve performance of the proposed design.

1. The structure remains untested, both experimentally and numerically, with a plethora of material models. Strain rate insensitive materials should be the priority of future investigations. Since strain rate sensitive material has a higher stiffness under higher strain rate, the difference between the impact speed of the pendulum test and the legform test did not favor the research objective. In this research, the impact condition with higher strain rate leading to a higher deformation resistant structure, which is the legform test, required a softer response. Materials with low strain rate sensitivity could potentially increase the difference of load response between the legform test and pendulum test to better satisfy the scope of research.
2. The structure could be divided into multiple sections and connected with revolute joints. Installing revolute joints at the location of groove 1 may reduce the load response during the legform test while having a negligible impact on the energy absorption in the pendulum test. Installing rotation direction restricted revolute joints at the location of the upper corner, which only allows the corner angle to increase, could greatly influence the deformation mode during the pendulum test which may increase the total energy absorption.

3. A sub-structure could be added inside the cell which is not connected to the existing structure, except at the bottom surface. The deformation of the sub-structure in the later stages of the impact event could enhance energy absorption while not increasing the initial peak load observed in the legform test.
4. Occupying the empty space in the cells with air bladders in which the bladders in a single layer of dissipating structure are connected. In a localized impact, air in a compressed bladder will flow into other bladders in which the air pressure will not increase on a large scale. In the large area impact where all bladders are compressed, the air pressure will be increased to resist the deformation, thus increasing the overall stiffness of the system.
5. An examination on parameter ‘G’, that being the thickness of the lower portion of the cell structure, could also be worthy of further investigation as it may play a significant role in the deformation mode of the cell structures.

REFERENCES

[1] National Highway Traffic Safety Administration. “Traffic Safety Facts 2015 Data–Pedestrians.” Washington, DC: US Department of Transportation, National Highway Traffic Safety Administration; Publication no. DOT-HS-812-375. 2017.

[2] World Health Organization. Global status report on road safety 2015. World Health Organization, 2015.

[3] United Nations Economic Commission for Europe (UNECE). Uniform provisions concerning the approval of motor vehicles with regard to their pedestrian safety performance. Regulation No. ECE 127:2015.

[4] U.S. Department of Transportation National Highway Traffic Safety Administration (NHTSA). Standard regulation on bumper standard. Regulation Part 581:1990.

[5] Yuen, S. C., and Nurick, G. N. "The energy-absorbing characteristics of tubular structures with geometric and material modifications: an overview." Applied Mechanics Reviews 61.2 (2008): 020802.

[6] Guillow, S. R., Lu, G., and Grzebieta, R. H. "Quasi-static axial compression of thin-walled circular aluminium tubes." International Journal of Mechanical Sciences 43.9 (2001): 2103-2123.

[7] Tang, Z. L., Liu, S. T., and Zhang, Z. H. "Analysis of energy absorption characteristics of cylindrical multi-cell columns." Thin-Walled Structures 62 (2013): 75-84.

[8] Hosseinipour, S. J., and Daneshi, G. H. "Energy absorption and mean crushing load of thin-walled grooved tubes under axial compression." Thin-walled structures 41.1 (2003): 31-46.

[9] Al-Hassani, S. T. S., Johnson, W., and Lowe, W. T. "Characteristics of inversion tubes under axial loading." Journal of Mechanical Engineering Science 14.6 (1972): 370-381.

[10] Huang, X., Lu, G. X., and Yu, T. X. "On the axial splitting and curling of circular metal tubes." International journal of mechanical sciences 44.11 (2002): 2369-2391.

[11] Jin, S. Novel cutting deformation modes on axially loaded circular AA6061-T6 extrusions for superior crashworthiness performance [Dissertation]. Windsor (ON, Canada): University of Windsor; 2012.

[12] Alghamdi, A. A. A., Aljawi, A. A. N., and Abu-Mansour, TM-N. "Modes of axial collapse of unconstrained capped frusta." International Journal of Mechanical Sciences 44.6 (2002): 1145-1161.

[13] Alghamdi, A. A. A. "Folding-crumpling of thin-walled aluminium frusta." International Journal of Crashworthiness 7.1 (2002): 67-78.

[14] Gupta, N. K., Prasad, G. E., and Gupta, S. K. "Axial compression of metallic spherical shells between rigid plates." Thin-walled structures 34.1 (1999): 21-41.

[15] Dehghanpour, S., and Yousefi, Y. "Lateral Crushing of Square and Rectangular Metallic Tubes under Different Quasi-Static Conditions." World Academy of Science, Engineering and Technology, International Journal of Mechanical,

Aerospace, Industrial, Mechatronic and Manufacturing Engineering 6.1 (2012): 204-208.

[16] Wang, H., Liu, R., Yang, J., Liu, H., and Sun, Y. "Theoretical model for elliptical tube laterally impacted by two parallel rigid plates." Applied Mathematics and Mechanics 37.2 (2016): 227-236.

[17] Morris, E., Olabi, A. G., and Hashmi, M. S. J. "Lateral crushing of circular and non-circular tube systems under quasi-static conditions." Journal of Materials Processing Technology 191.1-3 (2007): 132-135.

[18] Niknejad, A., Elahi, S. M., Elahi, S. A., and Elahi, S. A. "Theoretical and experimental study on the flattening deformation of the rectangular brazen and aluminum columns." Archives of Civil and Mechanical Engineering 13.4 (2013): 449-464.

[19] Baroutaji, A., Morris, E., and Olabi, A. G. "Quasi-static response and multi-objective crashworthiness optimization of oblong tube under lateral loading." Thin-Walled Structures 82 (2014): 262-277.

[20] Baroutaji, A., Gilchrist, M. D., Smyth, D., and Olabi, A. G. "Crush analysis and multi-objective optimization design for circular tube under quasi-static lateral loading." Thin-Walled Structures 86 (2015): 121-131.

[21] Khanchehzar, P., Niknejad, A., and Amirhosseini, S. G. "Influences of different internal stiffeners on energy absorption behavior of square sections during the flattening process." Thin-Walled Structures 107 (2016): 462-472.

[22] Niknejad, A., and Orojloo, P. H. "A novel nested system of tubes with special cross-section as the energy absorber." Thin-Walled Structures 100 (2016): 113-123.

[23] Baroutaji, A., and Olabi, A. G. "Lateral collapse of short-length sandwich tubes compressed by different indenters and exposed to external constraints: Laterales Versagen von kurzen Verbundrohren unter Druckbelastung mittels verschiedener Eindringkörper und äußerer Auflagerbedingungen." Materialwissenschaft und Werkstofftechnik 45.5 (2014).

[24] Lu, G., and Yu, T. X. *Energy absorption of structures and materials*. Elsevier, 2003.

[25] Smith, R. Experimental Testing of Aluminum Foam Filled Stainless Steel Braided Tubes Subjected to Transverse Impact [master's thesis]. Windsor (ON, Canada): University of Windsor; 2015.

[26] Deshpande, V. S., and Fleck, N. A. "Energy absorption of an egg-box material." Journal of the Mechanics and Physics of Solids 51.1 (2003): 187-208.

[27] Zupan, M., Chen, C., and Fleck, N. A. "The plastic collapse and energy absorption capacity of egg-box panels." International Journal of Mechanical Sciences 45.5 (2003): 851-871.

[28] Nowpada, S., Chirwa, E. C., Myler, P., and Matsika, E. "Aluminum "Egg-Box" Panel as an Energy Absorber for Pedestrian Protection." Advanced Engineering Materials 12.7 (2010): 591-595.

[29] Sashikumar, S., Chirwa, E. C., Myler, P., Qian, P., and Matsika, E. "Numerical investigation into the collapse behaviour of an aluminium egg-box under quasi-static loading." International Journal of Crashworthiness 17.6 (2012): 582-590.

[30] Yoo, S. H., Chang, S. H., and Sutcliffe, M. P. F. "Compressive characteristics of foam-filled composite egg-box sandwich panels as energy absorbing structures." Composites Part A: Applied Science and Manufacturing 41.3 (2010): 427-434.

[31] LSTC. LS-DYNA keyword manual. Vol. I. Livermore (CA): Livermore Software Technology Corporation (LSTC); 2015.

[32] ASTM, I. Standard test methods and definitions for mechanical testing of steel products. ASTM A370; 2012.

[33] Oberkampf, W. L., and Trucano, T. G. "Verification and validation in computational fluid dynamics." Progress in Aerospace Sciences 38.3 (2002): 209-272.

APPENDIX A: LOAD/DISPLACEMENT RESPONSES FROM PARAMETRIC AND GEOMETRIC STUDIES

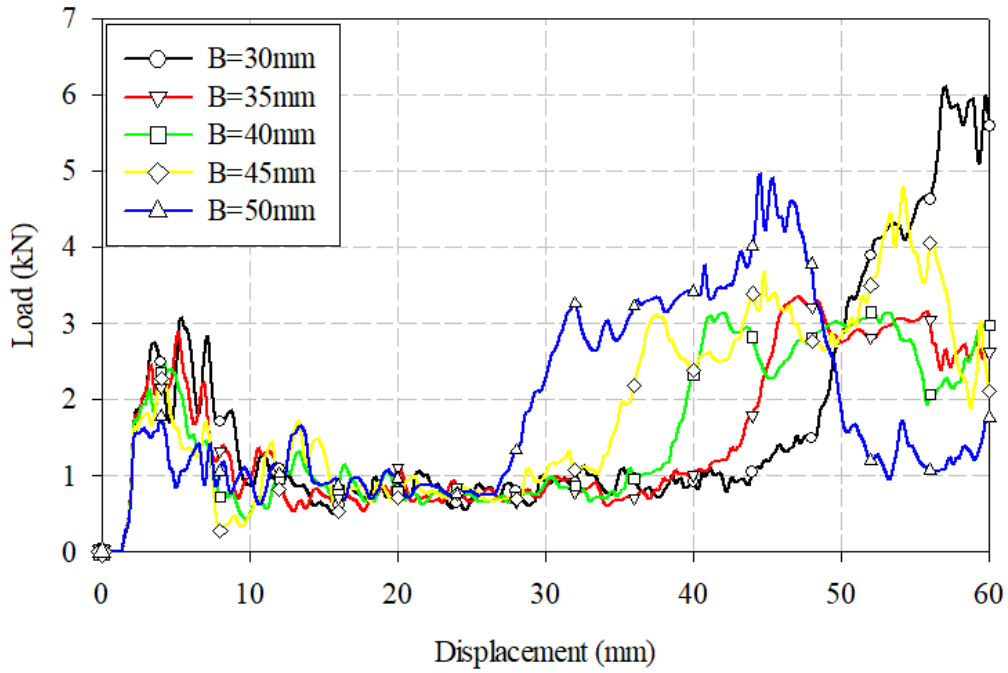

Figure A1. Legform test results from the parametric study of dimension "B".

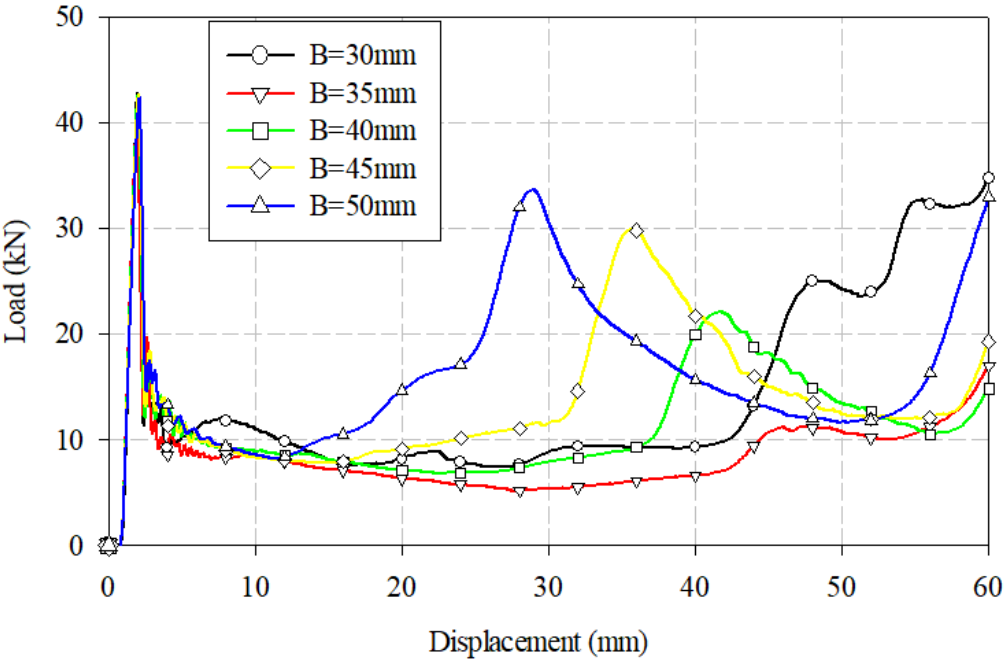

Figure A2. Pendulum test results from the parametric study of dimension "B".

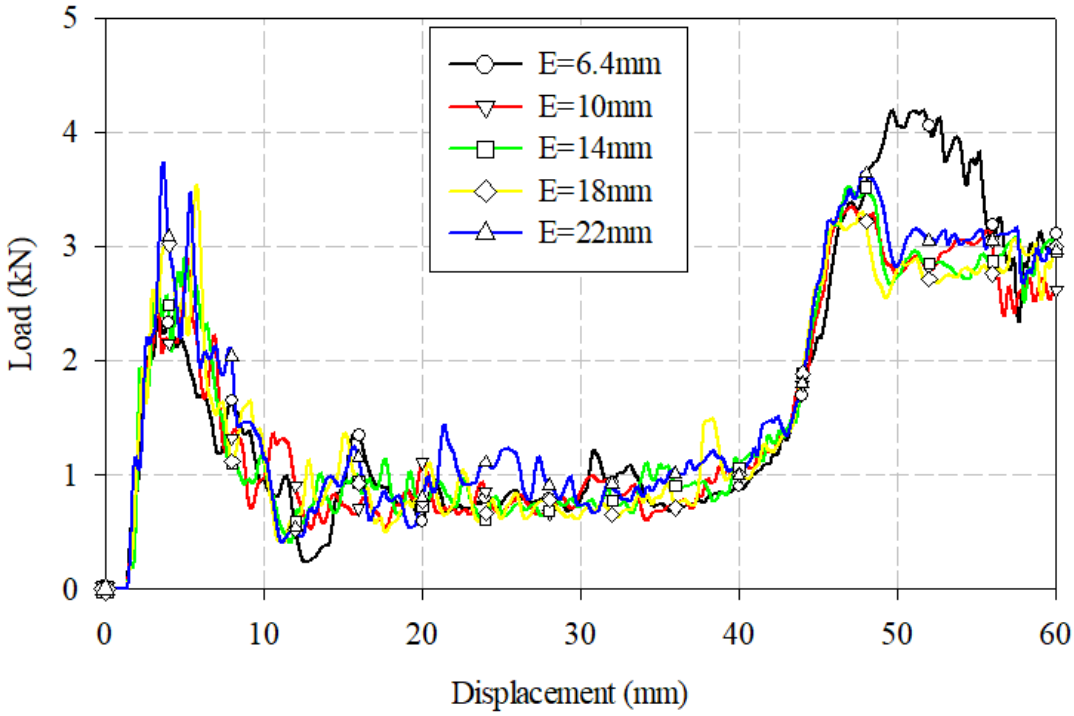

Figure A3. Legform test results from the parametric study of dimension "E"

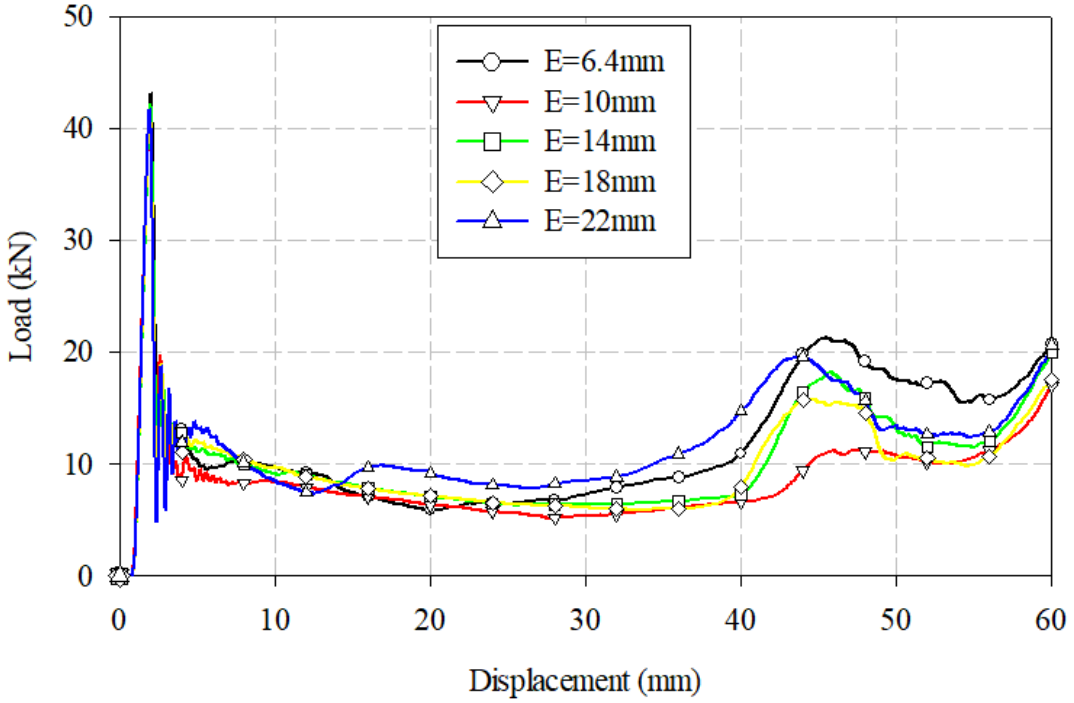

Figure A4. Pendulum test results from the parametric study of dimension "E"

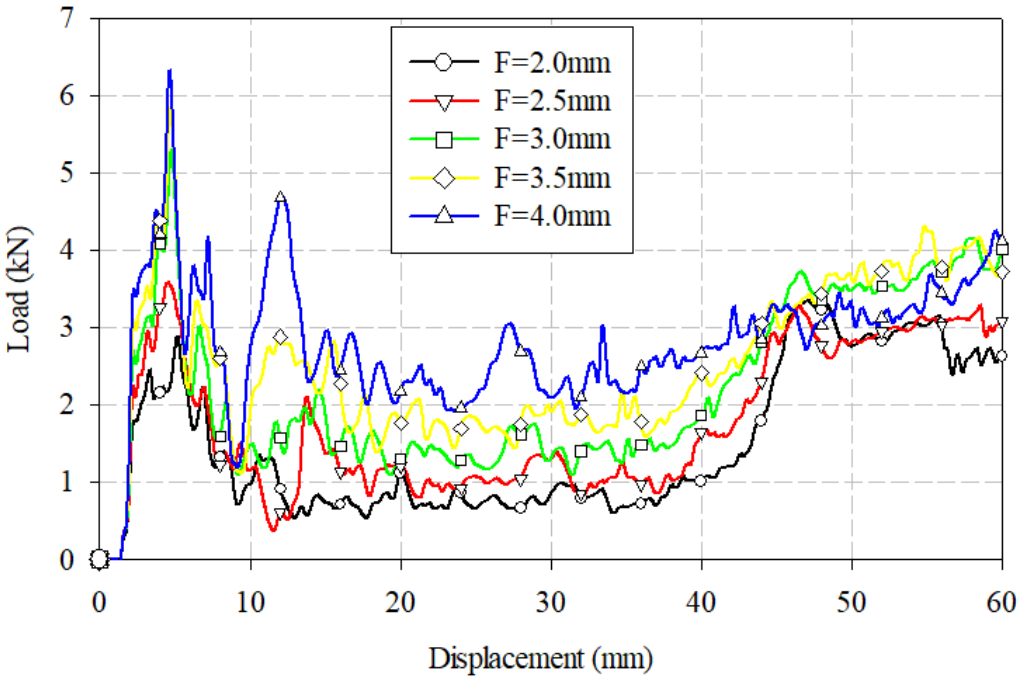

Figure A5. Legform test results from the parametric study of dimension "F".

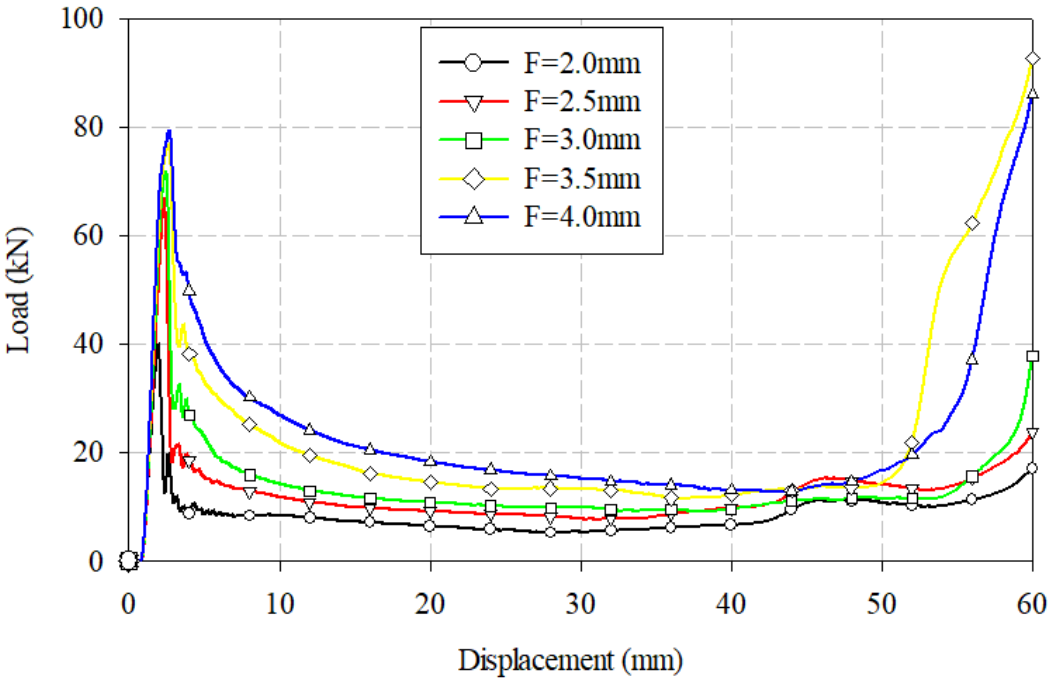

Figure A6. Pendulum test results from the parametric study of dimension "F".

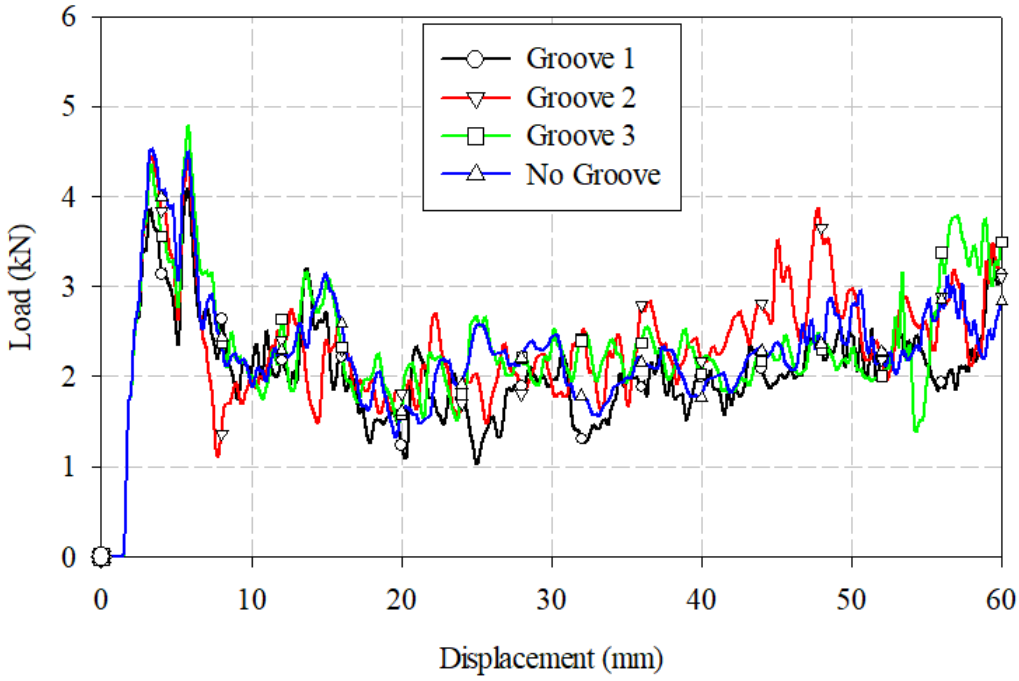

Figure A7. Legform test results with various Groove designs.

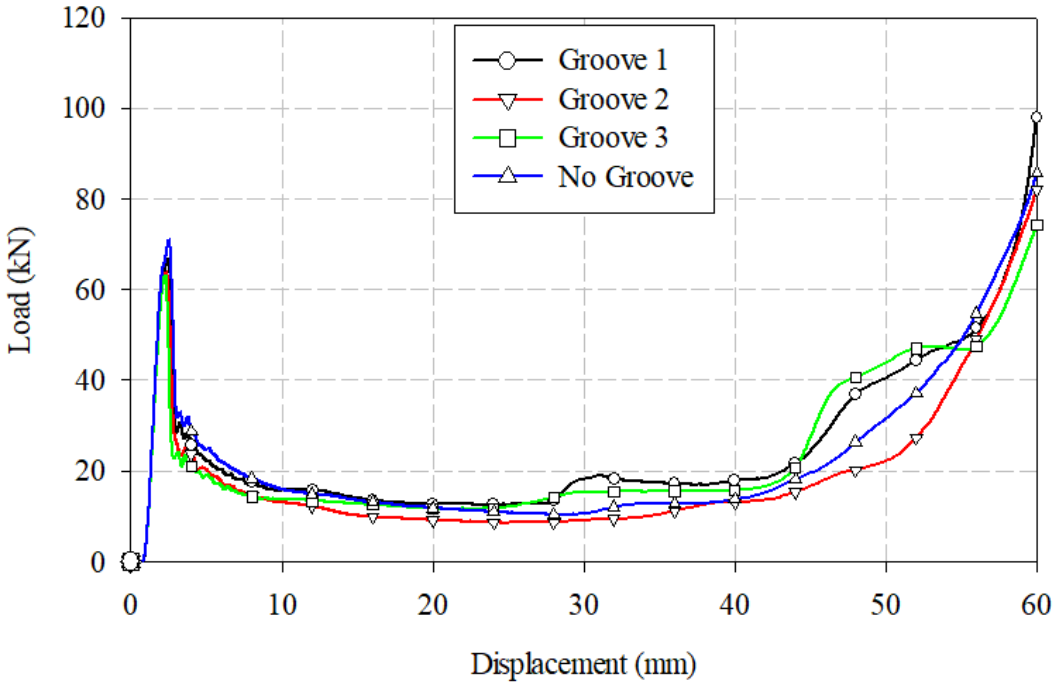

Figure A8. Pendulum test results with various Groove designs.

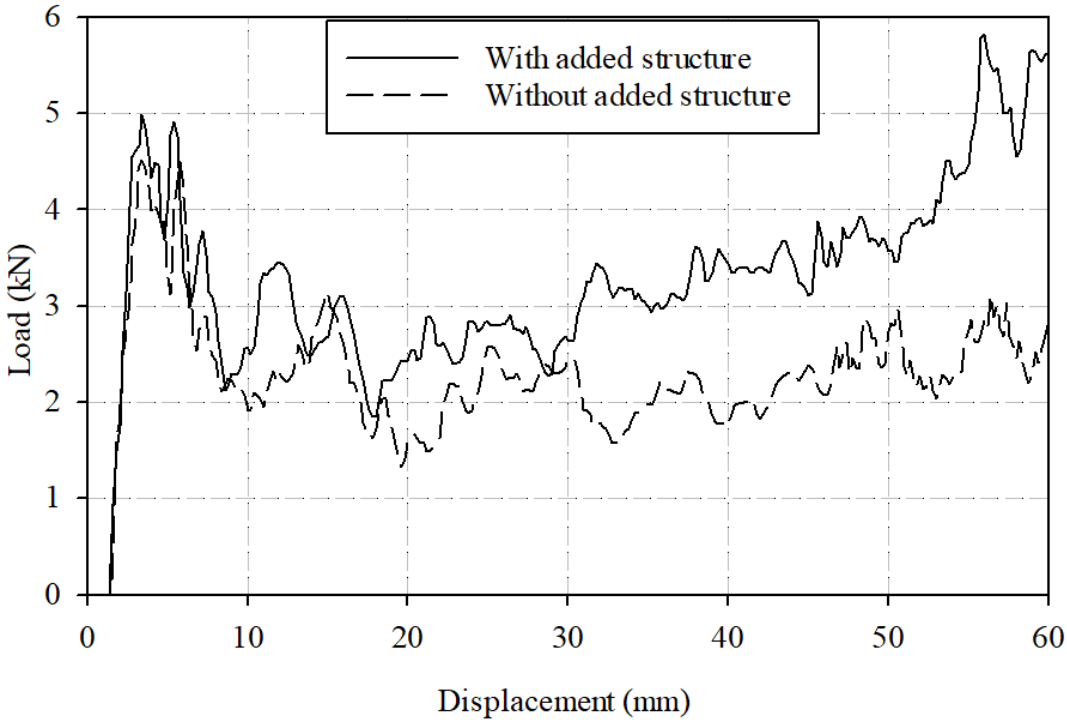

Figure A9. Legform test results with an added structure in the top section.

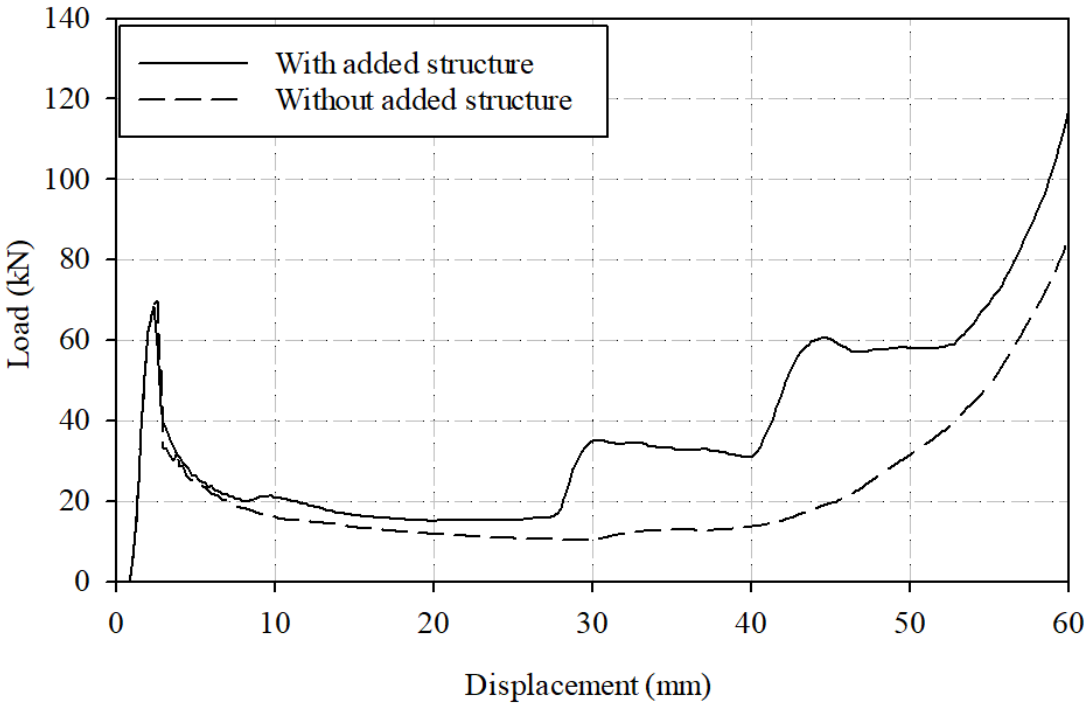

Figure A10. Pendulum test results with an added structure in the top section.

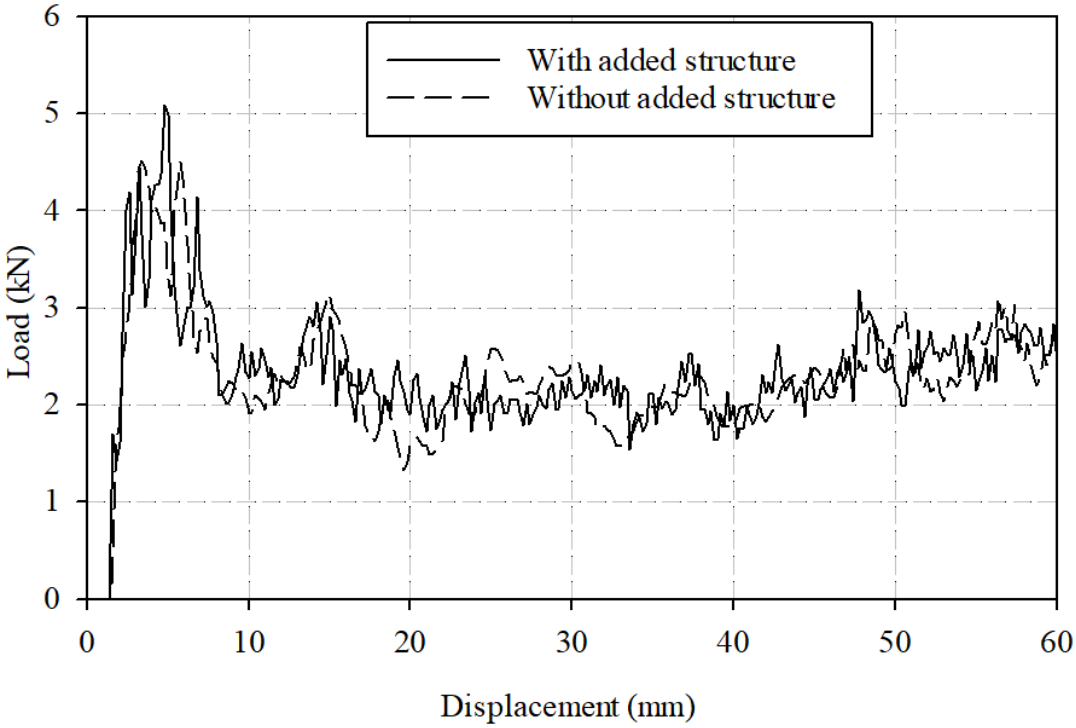

Figure A11. Legform test results with an extended top surface.

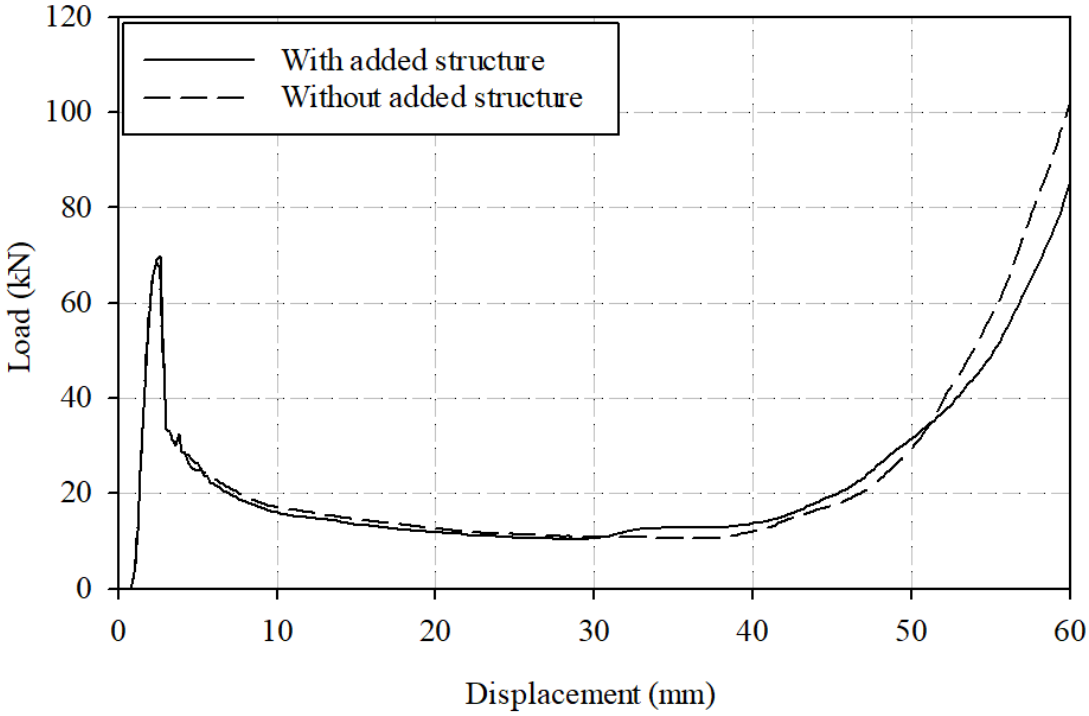

Figure A12. Pendulum test results with an extended top surface.

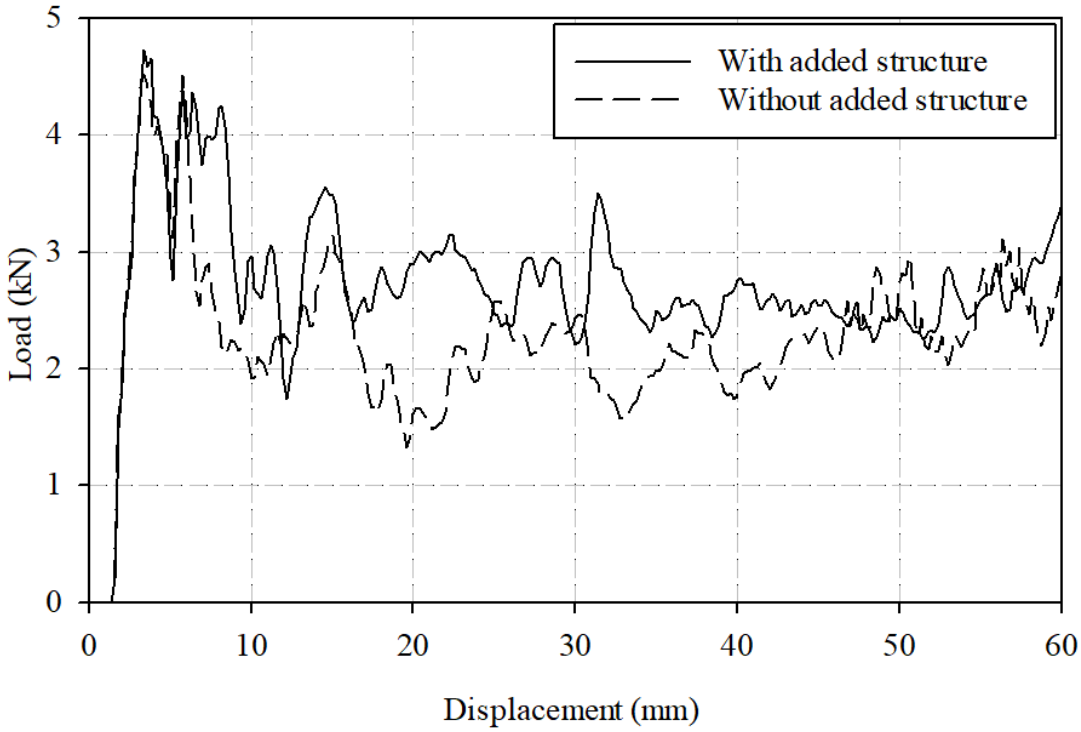

Figure A13. Legform test results with added support structure in the lower section.

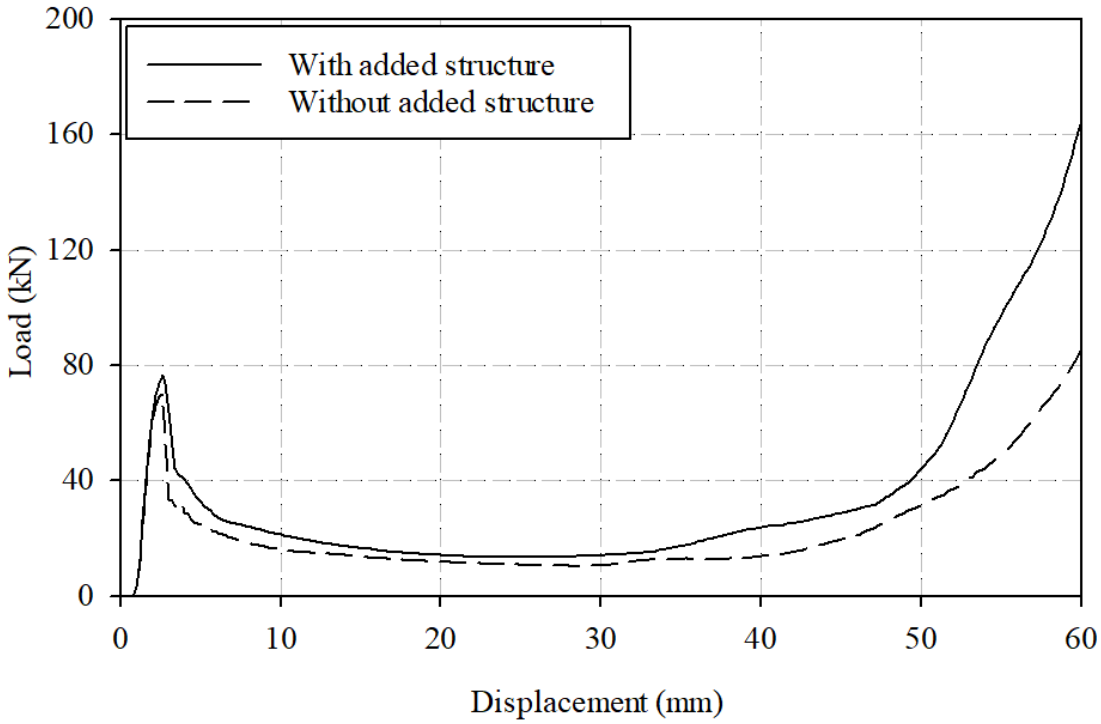

Figure A14. Pendulum test results with added support structure in the lower section.

APPENDIX B: DETAILED NUMERICAL COMPARISON OF PARAMETRIC AND GEOMETRIC STUDY

Table B4. Parametric test detailed result.

Parametric Study results									
Dimension (mm)	Load in **LEGFORM test** (kN)			Pendulum test Maximum load (kN)	Energy absorption in PENDULUM test (J)			SEA at 60mm (J/kg)	Change of Energy at 60mm
	Maximum load	Change of maximum load	Average load		At 10mm	At 30mm	At 60mm		
Baseline (B=35, E=10, F=2.0)	3.3	-	1.48	39.5	104	233	504	993	-
(**B=30**, E=10, F=2.0)	6.1	+84.8%	1.70	42.8	116	268	672	1329	+33.3%
(**B=40**, E=10, F=2.0)	3.2	-3.0%	1.55	42.5	116	268	672	1319	+33.3%
(**B=45**, E=10, F=2.0)	4.8	+45.5%	1.82	42.0	117	303	816	1593	+61.9%
(**B=50**, E=10, F=2.0)	4.9	+48.5%	1.85	40.5	120	447	963	1866	+90.9%
(B=35, **E=6.4**, F=2.0)	4.2	+27.3%	1.65	43.0	118	261	698	1387	+38.5%
(B=35, **E=14**, F=2.0)	3.4	+3.0%	1.54	38.0	114	257	543	1060	+7.8%
(B=35, **E=18**, F=2.0)	3.4	+3.0%	1.54	38.0	114	257	543	1049	+7.8%
(B=35, **E=22**, F=2.0)	3.6	+9.1%	1.55	38.5	112	252	542	1035	+7.4%
(B=35, E=10, **F=2.5**)	3.6	+9.1%	1.75	66.0	173	359	730	1308	+44.8%
(B=35, E=10, **F=3.0**)	5.3	+60.6%	2.20	71.4	222	444	811	1337	+60.9%
(B=35, E=10, **F=3.5**)	5.7	+72.7%	2.53	92.6	309	618	1405	2149	+178.7%
(B=35, E=10, **F=4.0**)	6.2	+87.9%	2.80	86.0	364	745	1424	2035	+182.5%

Table B5. Parametric test detailed result.

Geometric Study results								
Geometric feature	Load in **LEGFORM test** (kN)			Pendulum test Maximum load up to 55mm (kN)	Energy absorption in **PENDULUM test** (J)		SEA at 55mm (J/kg)	Displacement required for 1 kJ of energy absorption (mm)
	Maximum load	Change of maximum load	Average load		At 30mm	At 55mm		
Unmodified (baseline)	4.5	-	2.3	70	507	1100	2050	53
Groove	4.1	-9%	2	66	532	1270	2367	50
Extended top surface	5.1	13%	2.3	70	543	1120	2032	53
Added structure in upper section	5.8	29%	3.26	68.5	613	1920	3159	42
Support structure in lower section	4.7	4%	2.7	97.5	644	1510	2481	47

VITA AUCTORIS

NAME:	James Wu
PLACE OF BIRTH:	Xiongyue, Province of Liaoning, China
YEAR OF BIRTH:	1986
EDUCATION:	B.A.Sc., University of Windsor, Windsor, ON. 2014
CANDIDATE:	M.A.Sc., University of Windsor, Windsor, ON. 2014